Advances in Experimental Methods and Apparatus Design Applied to Investigate the Creep and Dehydration Behavior of Antigorite Serpentinite

by
Eric Burdette
B. S., University of Minnesota - Twin Cities, 2013

A dissertation submitted in partial fulfillment of the requirements for the Degree of Doctor of Philosophy in the Department of Earth, Environmental, and Planetary Sciences at Brown University

Providence, Rhode Island
Fall 2021

This dissertation by Eric Burdette is accepted in its present form by the Department of Earth, Environmental, and Planetary Sciences as satisfying the dissertation requirement for the degree of Doctor of Philosophy.

Date ______________ ______________________________

(Greg Hirth), Director

Recommended to the Graduate Council

Date ______________ ______________________________

(Reid Cooper), Reader

Date ______________ ______________________________

(Chris Huber), Reader

Date ______________ ______________________________

(Yan Liang), Reader

Date ______________ ______________________________

(Nick Beeler), Reader

Approved by the Graduate Council

Date ______________ ______________________________

(Andrew G. Campbell)
Dean of the Graduate School

Curriculum Vita

Eric Burdette

324 Brook Street
Providence, RI 02912
Email: eric_burdette@brown.edu
ORCID: 0000-0002-7940-2031

Education

Brown University — Providence, RI
Ph.D. in Geophysics, Advisor: Greg Hirth — 2016–2021

University of Minnesota - Twin Cities — Minneapolis, MN
B.S. in Materials Science and Engineering — 2009–2013

Experience

Corning Incorporated — Corning, NY
Firing Process Engineer — 2013–2016

- Focused on diesel filter firing cycle mechanical stress prediction (modeling) and 'big data' processing

Corning Incorporated — Corning, NY
Engineering Intern — summer 2012

- Study of wet cordierite die swell (rheology) and side feeder extruder performance

Publications

[1] A. Moarefvand, J. Gasc, J. Fauconnier, M. Baïsset, **E. Burdette**, L. Labrousse, and A. Schubnel, "A new generation griggs apparatus with active acoustic monitoring", *Tectonophysics*, p. 229 032, 2021, ISSN: 0040-1951.

[2] K. Okazaki, **E. Burdette**, and G. Hirth, "Rheology of the fluid oversaturated fault zones at the brittle-plastic transition", *Journal of Geophysical Research: Solid Earth*, vol. 126, no. 2, e2020JB020804, 2021.

[3] **E. Burdette** and G. Hirth, "Enhanced dehydration weakening of antigorite driven by slow shear heating: Insights from high-pressure experiments with a modified apparatus stiffness", *Journal of Geophysical Research: Solid Earth*, vol. 125, no. 11, e2020JB020064, 2020.

Acknowledgements

I am grateful for the mentorship, teaching, and patience of my advisor Greg Hirth. A marriage of materials science and geology has not always been easy, but his thoughtfulness and talent has carried us through. Thank you for believing in my ability execute unusual projects, like building a laser interferometer.

I would like to thank my committee members for sage guidance over my career. Reid Cooper, Chris Huber, Yan Liang, and Marc Parmentier have all supported me at times at times when I was struggling with lab or numerical problems. Nicolas Brantut and Matej Pec have been invaluable in their guidance through laboratory challenges, particularly during creep testing. David Kohlstedt invited me into the world of rock deformation and I will be forever grateful for that.

I would also like to thank my colleagues in the rock deformation lab. Keishi Okazaki's patience teaching me to do Griggs experiments was invaluable. My lab mates made coming to work every day an exciting experience. Thank you also for your patience as I have rewritten control software and upgraded the electronics on the Griggs rigs.

I would like to thank all of the faculty, staff, undergraduates, and graduate students. I have really enjoyed my time here at Brown University being a part of this community. The friendly and collegial atmosphere has made me a better scientist.

Finally, I'd like to thank my family Barb, Steve, and Lisa Burdette for supporting me along my journey to this point. Yaruska Ordinola-Perez in particular has helped me stay grounded, motivated, and inspired me to be a better person. Thank you all again for your support.

Contents

List of Tables

List of Figures

Introduction

Hydrous minerals play a critical role in determining the tectonics of the Earth's surface. Nowhere is this more obvious than the oceanic lithosphere and subduction zones. Over time the oceanic lithosphere experiences hydrothermal alteration, forming serpentinites as it moves towards subduction zones. Even small fractions of these hydrous minerals cause dramatic weakening.

Despite their ubiquitous nature, viscous deformation of serpentinite minerals has received relatively little attention because their unusual sheet structure and low dehydration temperature prevent experiments from accessing mechanisms that are likely active at very low strain rates in the earth. Some studies do exist, and show clearly that:

1. Serpentinite strength decreases significantly during and after dehydration due to pore fluid production and development of very fine grained reaction products.
2. Serpentinite deforms by shearing along grain boundaries and the basal planes of its sheets.
3. Slip on fault surfaces can lead to rapid shear heating.

At low pressure, the lizardite polymorph of serpentinite is dominant. Its sheets are not cross-linked and are nominally flat, causing it to be weaker than the high pressure polymorph, antigorite. Lizardite is prevalent in shallow sections of subduction zones, and altered transform faults like the San Andreas fault. Its behavior is not examined here, but the geometry of sheet deformation and methods for closely replicating the earth deformation of antigorite can be applied to better understand the influence of texture/strength evolution in the Earth and constrain hazards associated with post-seismic creep.

At high pressure the antigorite polymorph is prevalent, and has been called on to explain anomalous earthquakes at high pressure and tectonic viscosity limits in subduction zones. Both of these phenomena have been difficult to replicate in the lab, partly due to deformation apparatus limitations, and partly due to the complex evolution of deforming sheets that do not recrystallize in the lab.

Rock deformation machines are typically constructed with the strongest materials that could be deformed in mind. This leads to the use of large diameter pistons and stiff materials like alumina or tungsten carbide to construct most of the elements that load samples. This is a significant difference from the earth, where typically large (1m+) bodies of the same material surround the deforming zone of interest, which is also typically larger than laboratory samples. The size and stiffness differences lead to a large difference in elastic energy available to materials deformed in the Earth and the lab. This difference is significant for rupture and dynamic weakening processes: weakening that occurs in stiff machines quickly 'runs out' of available elastic energy which stops the dynamic feedback processes. The first chapter of this thesis describes an investigation of the relevance of stored energy (machine compliance) to antigorite weakening during dehydration. The third chapter outlines methods for calculating stiffness in a typical lab deformation geometry, and the effects typical experimental choices, like the amount of viscous resistance, may have on experimental fault compliance.

Rock deformation experiments are also constrained by their operators. Long duration experiments are impossible in many cases, in stark contrast to deformation in the Earth, which can last for millions of years. This difference leads to forcing materials in the lab to deform at much faster strain rates than those observed in nature to accumulate appreciable deformation. Some materials like olivine and quartz can be heated to higher temperatures, which increases the rate of deformation, and their rheological behavior can then be extrapolated to lower temperatures with understanding of active deformation mechanisms. This practice is not possible with serpentinites due to their limited thermal stability (approximately 300°C and 600°C for lizardite and antigorite, respectively), so prior work examined their brittle behavior (opening and sliding of cracks) extrapolated to low strain rates, or ignored the effect of very low strain rate entirely. The Griggs-type assembly was redesigned and recalibrated here to precisely measure low stress and strain rates. The second chapter of this thesis describes an investigation of the microstructure resulting from deforming antigorite slowly to low strains under constant stress creep conditions at pressures which suppress crack growth. The resulting plastic deformation highlights the importance of kinks, a previously overlooked deformation mechanism, and illuminates a microstructural mechanism and flow law that can be confidently extrapolated to natural conditions. Chapter 4 documents design of a laser displacement/load sensor that can be used to significantly increase accuracy of future creep and rupture experiments, further improving our ability match earth conditions.

Chapter 1

Enhanced Dehydration Weakening of Antigorite Driven by Slow Shear Heating: Insights from High-Pressure Experiments with a Modified Apparatus Stiffness

Eric Burdette and Greg Hirth

[1]Department of Earth, Environmental and Planetary Sciences, Brown University, Providence, RI, USA

*

Key Points:

- Apparatus stiffness was reduced by an order of magnitude with a soft spring added to the loading column.
- Increased weakening rates during dehydration correlate with both apparatus compliance and imposed load-point displacement rate (V_0).
- High reaction extent and fluid-filled porosity in the center of recovered specimens indicates shear enhanced reaction and resulting weakening.

*Published in Journal of Geophysical Research: Solid Earth, 125, 11, (2019)

Abstract

Deformation experiments were conducted to investigate the influence of apparatus stiffness on frictional stability during dehydration of antigorite. These experiments also provided a novel way to constrain relationships between fault slip rate and reaction weakening. Experiments were conducted at a confining pressure of 1 GPa using a Griggs apparatus with a modified loading column. During experiments, the temperature was ramped from 400 to 700°C over 600 seconds, while deformation was imposed with varying load-point displacement rates. No stick-slip behavior was observed during the experiments, despite an order of magnitude lower apparatus stiffness, suggesting there are inherent differences in the frictional stability between low pressure (where stick-slip is observed during dehydration) and high pressure experiments. Fault slip at high pressure may be stabilized by higher dehydration temperatures and higher shear stresses prior to the onset of dehydration reactions. In comparison to reference experiments conducted with an unmodified stiffness, the weakening rate during dehydration increases by a factor of two. In addition, the time (and therefore imposed temperature) at which the maximum weakening rate is observed decreases linearly with increasing maximum weakening rate. Microstructures in the deformed samples illustrate much greater reaction extents (locally $> 50\%$) relative to the reference experiments ($< 1\%$), with decreasing reaction extent away from the primary slip surfaces. These observations indicate that the dehydration reaction is enhanced by additional shear dissipation resulting from a tenfold increase in displacement per increment of weakening. The shear-enhanced reaction mechanism could potentially generate runaway slip in subduction zone settings, leading to intermediate-depth earthquakes.

Plain Language Summary: The mechanisms that promote intermediate depth earthquakes (50-200km) observed in subduction zones remain poorly understood because brittle materials are generally too strong at low temperature and high pressure to fracture and slide. Reactions in water-bearing minerals are thought to counteract the influence of high pressure, allowing brittle failure. However, previous studies conducted at mantle pressures only show evidence for stable fault slip that would not produce earthquakes. The experiments presented here show that when we make

our high-pressure deformation machine less stiff (resulting in a larger stored energy to drive slip), samples react, and weaken. With the lower apparatus stiffness, pronounced shear heating leads to more rapid (though still stable) stress drops. The shear heating mechanism can be scaled to natural conditions to investigate processes that lead to earthquakes in subduction zones.

1.1 Introduction

Magnitude 8+ earthquakes occur in subduction zones at depths of 50-100 km where estimated pressures are greater than 1 GPa. At these conditions, below the normal seismogenic zone, most subduction zone materials are extremely strong or deform in a stable rate-strengthening manner, which inhibits earthquake nucleation (Scholz, 1998). Thus, these intermediate-depth earthquakes have long been hypothesized to result from dehydration embrittlement of serpentinite (Raleigh and Paterson, 1965), or other hydrous phase, as well as other processes associated with dehydration reactions (c.f. Hacker et al., 2003; Rutter et al., 2009; Ferrand et al., 2017)). However, some experimental studies conducted at mantle pressures indicate stable sliding during dehydration of serpentinite (Chernak and Hirth, 2011; Proctor and Hirth, 2015; Okazaki and Hirth, 2016; Ferrand et al., 2017; Gasc et al., 2017). Here we investigate the possibility that differences in frictional stability during dehydration of antigorite arise from differences in apparatus stiffness. Our new experiments show stable sliding during dehydration, however, we also find evidence for weakening rates enhanced by shear heating. When scaled to natural conditions, such shear heating mechanisms could account for some seismicity.

Previous experiments on serpentinite show a range of slip behaviors at different confining pressures. For example, nominally drained experiments on antigorite conducted in a gas apparatus at confining pressures below 200 MPa show transitions from distributed shear, to slow slip, and finally to stick-slip behavior as temperature is increased above the dehydration temperature (Okazaki and Katayama, 2015). In contrast, experiments conducted in Griggs-type solid-medium apparatuses at 1-1.5 GPa confining pressure show only slow (stable) slip during dehydration, with no rapid load drops (Proctor and Hirth, 2015; Okazaki and Hirth, 2016) under both drained and un-drained conditions. Similarly, experiments conducted at pressures up to 4 GPa in the D-DIA apparatus do not show evidence for stick-slip during dehydration of pure antigorite based on acoustic emission records (Ferrand et al., 2017; Gasc et al., 2017); the acquisition rate of stress measurements in the D-DIA make it difficult to identify stick-slip from mechanical data. These differences make it difficult to extrapolate relationships to conditions appropriate for intermediate earthquakes. Here we investigate the possibility that this apparent discrepancy between low- and high-pressure experiments can be explained by differences in the apparatus stiffness.

For materials that develop frictional fault surfaces, such as antigorite at our deformation conditions (e.g. Proctor and Hirth, 2016), mechanical behavior is often modeled using rate-and-state friction that describes weakening or strengthening with time and slip velocity. The model has three parameters to describe the evolution of friction: a is the direct logarithmic velocity dependence of the friction coefficient, b and Dc combine to describe displacement and time dependent evolution of friction. (a-b) is positive if steady-state friction is an increasing function of velocity. Frictional stability criteria (i.e., defining conditions where stable rather than unstable fault slip occur) for materials that obey rate and state friction can be defined using the relationship (e.g. Ruina, 1983):

$$\frac{K}{\sigma_n} \geq \frac{-(a-b)}{D_c}, \tag{1.1}$$

where K is shear stiffness (the elastic relationship between shear stress and shear displacement on the fault surface), and σ_n is normal stress. Three responses to velocity perturbations are possible, depending on the velocity-dependence of friction. For velocity strengthening (a-b) > 0, the system is stable. For velocity weakening, the system is conditionally stable if equation (1.1) is satisfied, but the system is intrinsically unstable if $\frac{K}{\sigma_n} < \frac{-(a-b)}{D_c}$. The transitions in slip behavior observed by Okazaki and Katayama (2015) were hypothesized to result from changes in the frictional properties with increasing temperature. Equation (1.1) shows that increasing K (or, K/σ_n) promotes stable sliding. Thus, assuming that the frictional properties remain the same at high pressure, one explanation for the lack of stick-slip in the Griggs and D-DIA experiments is that the ratio $\frac{K}{\sigma_n}$ is much larger for the higher confining pressure experiments (Figure 1.1). Alternatively, the frictional behavior might change as a function of confining pressure at a given temperature and strain rate. Okazaki and Katayama (2015) report an apparatus stiffness of 58 MPa/mm, while the higher pressure apparatus have a stiffness of 2 GPa/mm (Griggs-type apparatus) and 200 GPa/mm (D-DIA; see calculation in the appendix), respectively. As described in the next sections, we tested these hypotheses by modifying the stiffness of the Griggs apparatus to match the ratio $\frac{K}{\sigma_n}$ (and thus stability) of Okazaki and Katayama (2015), while running experiments using the same procedures as Proctor and Hirth (2015).

The modification of the apparatus also allowed us to explore the role of shear dissipation in reaction weakening. As frictional slip proceeds during dehydration of antigorite at 1 GPa confining pressure, pore fluid pressure increases due to a reaction producing forsterite, enstatite/talc, and water causing samples to weaken in response to decreasing effective normal stress. Temperature ramping results in a bell-shaped reaction rate versus time curve, with a peak at a characteristic reaction extent (Vyazovkin et al. (2011); Trittschack et al. (2014); Trittschack et al., 2014 illustrate this behavior for brucite and serpentine). Chernak and Hirth (2011) illustrate that the weakening rate during dehydration increases with increasing temperature ramp rate (indicting a relationship between reaction rate and weakening rate). Proctor and Hirth (2015) illustrate that the weakening arises from an increase in pore-fluid pressure by comparing drained (reaction with no pore fluid pressure) and the undrained dehydration experiments, consistent with the related work of and Murrell and Ismail (1976). The reduction in strength during pore-fluid weakening is accompanied by an elastic response of the machine. The system can be described by a simple slider-block model with equations:

$$\tau = \mu\left(V\right) * \left(\sigma_n - P_f(\omega)\right), \tag{1.2}$$

$$V = \frac{1}{K}\left(-\frac{d\tau}{dt}\right) + V_0, \tag{1.3}$$

Where τ is shear stress, V is slip velocity, μ is the velocity-dependent friction coefficient, P_f is pore fluid pressure as a function of reaction, ω is reaction extent, and K is shear stiffness.

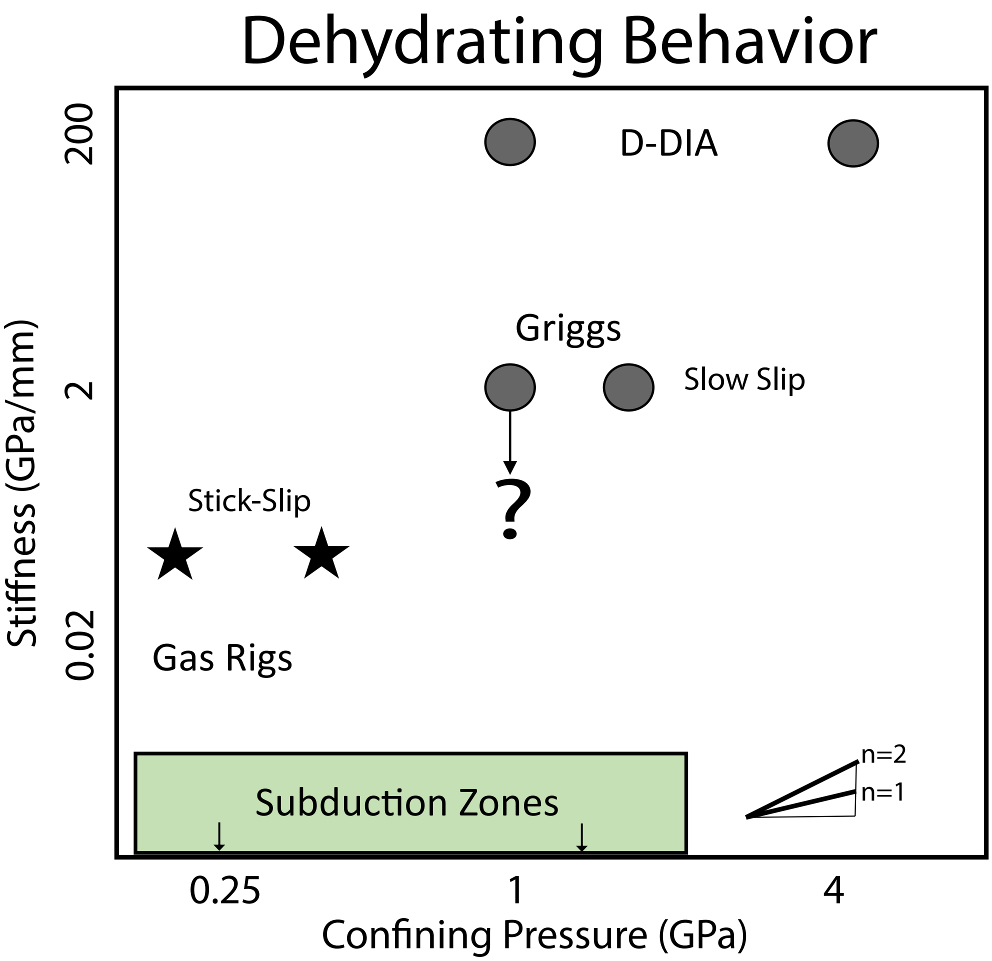

Figure 1.1: Confining pressure and corresponding apparatus stiffness plotted for conditions of previous experimental studies of mechanical behavior during dehydration of antigorite. D-DIA studies referenced are those of Hilairet et al. (2007); Ferrand et al. (2017); Gasc et al. (2011). Griggs studies referenced are those of Chernak et al. (2011), Proctor et al. (2015), and Okazaki et al (2016). Gas apparatus experiments referenced are those of Okazaki et al. (2015), and Murrell et al. (1976). Plotted on a log scale to illustrate stiffness ($< 5 * 10^{-5}$ MPa/mm, methods of Fletcher and McGarr 2006) and pressure in subduction zones.

As shown by equations (1.2) and (1.3), the friction coefficient is connected to an elastic response through its dependence on velocity. Pore fluid pressure can be affected by the elastic response through shear dissipation (a function of velocity V) that drives increased reaction rates. Similar to the rate-state friction criteria in equation (1.1), the inclusion of shear heating results in more complex conditional stability criteria that depend on a minimum stiffness, starting shear stress, thermal diffusivity, and permeability (examined by Brantut and Sulem (2012)). In the experiments described here, we reduced K by a factor of ten, which leads to a tenfold increase in shear dissipation that can enhance reaction and be assessed through the time evolution of strength.

1.2 Materials and Methods

1.2.1 Materials and Sample Preparation

Antigorite samples were synthesized from a serpentinite collected from the Nagasaki metamorphic belt in Japan; this sample is predominantly antigorite (98%) with minor diopside, spinel and magnetite. The serpentinite was crushed and sieved to prepare gouge samples with a grain size of 20 um to 45 um. Powder was washed and magnetically separated following sieving. The weight of gouge sample used for each run was 150.0 mg, resulting in a sample thickness of 1.1 mm without any optically visible porosity ($< 1\%$) after hot-pressing for 12 hours at 400°C and 1 GPa confining pressure.

1.2.2 Deformation Procedure and Sample Assembly

Experiments were conducted in a Griggs-type triaxial press (Tullis and Tullis, 1986) using NaCl as a confining medium, at a confining pressure of 1 GPa and a temperature range from 400 to 700°C. Samples were deformed at imposed displacement rates (V_0) of 0.18, 0.36, or 1.8 μm/s using an AC motor. We refer to V_0 as the load-point displacement rate; specifically, V_0 is the displacement rate measured between the top of the load cell and the upper platen (Figure 1.2).

Powder was placed between alumina shear pistons cut at angles of 30, 45, or 60 degrees to

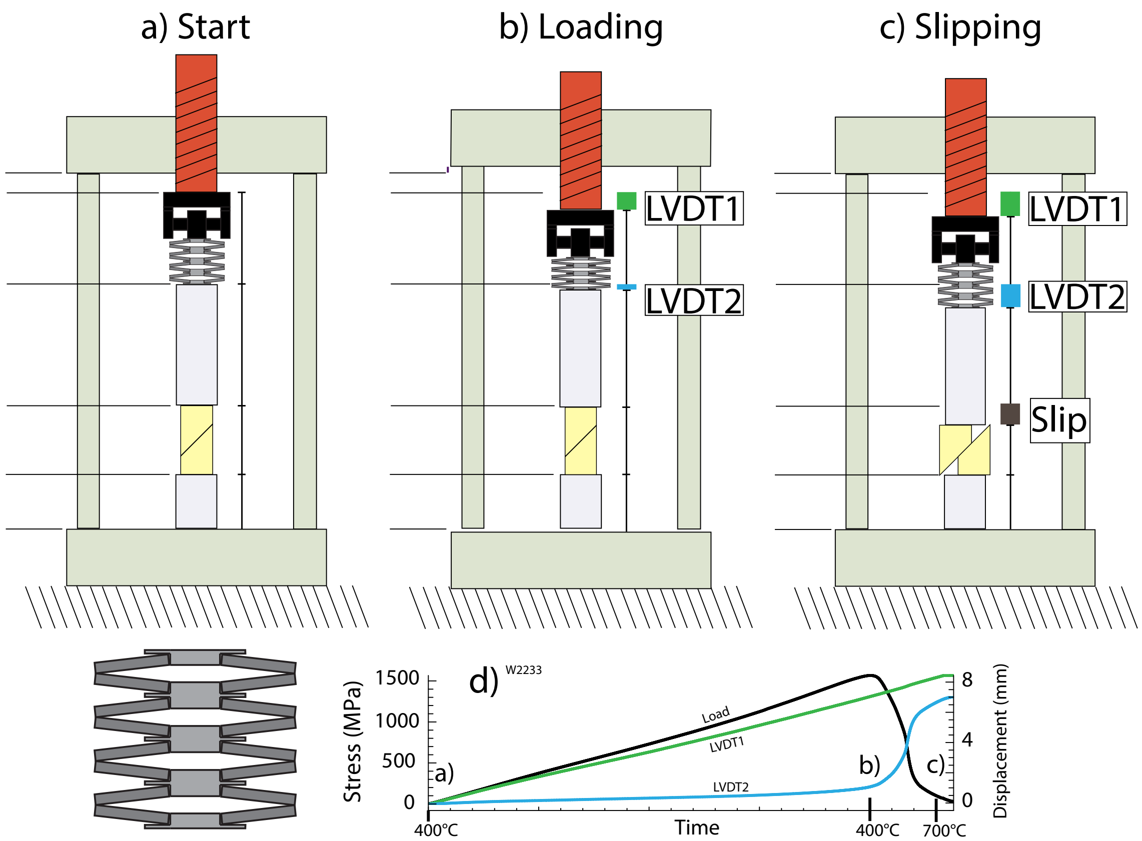

Figure 1.2: Schematic figure illustrating relative movement of modified triaxial apparatus elements during antigorite deformation/dehydration runs (W2333 is depicted). (a) Initial apparatus position with no differential stress applied to the gouge sample. (b) Sample loaded to peak stress. Axial loading is applied by a ball screw represented by the cross-hatched element at the top of the column. Elastic displacement is stored primarily in the disk springs with a small portion stored in the column below the disk spring. (c) Apparatus position during and after weakening. Note that the majority of displacement is generated by the spring elements. (d) Time history of the load and displacement for both transducers (LVDT1&2). Black bars indicate start of the temperature ramp at 400°C, and the end of temperature ramp at 700°C.

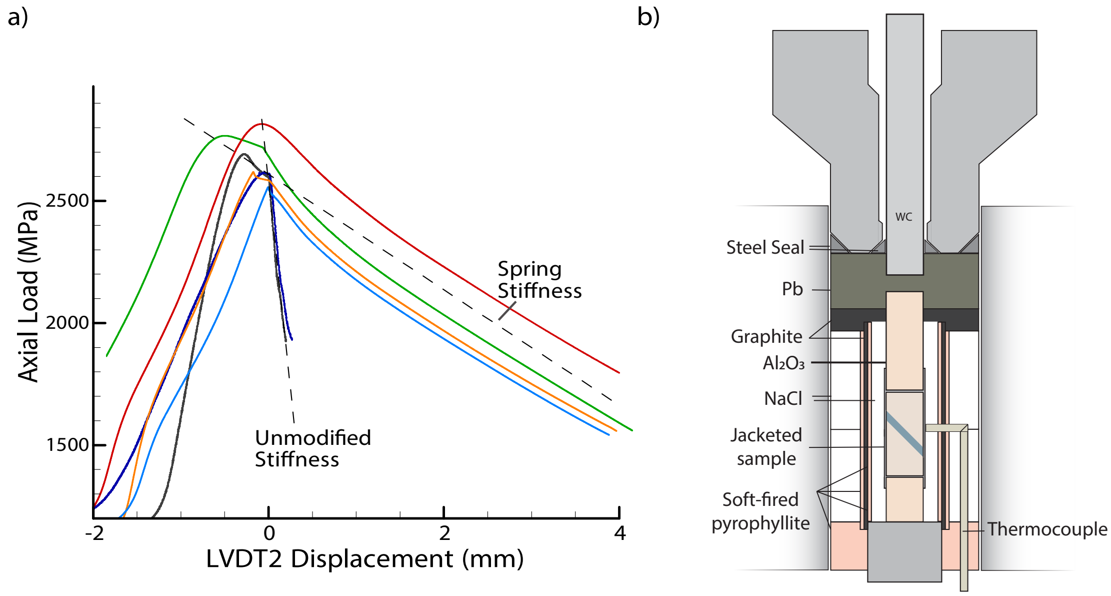

Figure 1.3: Figures summarizing recorded axial load vs LVDT2 displacement and a depiction of the sample assembly. (a) Load plotted against displacement for dehydration runs, with displacement referenced to the recorded value at initiation of the temperature ramp. Dashed reference lines are plotted for the static stiffness of the standard and modified apparatus. (b) Schematic illustration of the experimental apparatus inside the pressure vessel. Sample powder is contained between two sawcut alumina shear pistons inside the silver jacket.

the axial stress and placed inside a cylindrical Ag jacket with wall thickness of 0.25 mm. Ag disks were placed at the end of each shear piston and mechanically sealed during a short cold pressing step. Sample temperature was measured using a Pt–Pt10%Rh thermocouple placed next to the jacket at the sample center (Figure 1.3b). Samples were brought to 1 GPa and 400°C, allowed to equilibrate for 12 hours, and then loaded at a constant load-point displacement rate. After reaching peak stress and the initial onset of weakening (Figure 1.3), the temperature setpoint was ramped from 400-700°C at 0.5°C/s while V_0 was maintained (calculations indicate <1°C sample temperature lag, see supporting information). After reaching 700°C, all samples were first quenched under load to 300°C in 1 min and then returned to ambient conditions over 1–2 h. Samples were then impregnated with epoxy, cut and polished into thin-sections for microstructural analysis.

1.2.3 Deformation Apparatus

The loading frame of the press was modified to change stiffness between experiments by inserting a modular column comprised of paired Belleville disk springs. The original load cell was replaced with a smaller load cell to accommodate this change. The unmodified apparatus axial stiffness ($K_{Apparatus}$) is 1.97 GPa/mm. The modified apparatus is an order of magnitude less stiff (0.194 GPa/mm) with the addition of 4 pairs of Belleville disk springs. This modification of stiffness leads to an order of magnitude more sample displacement for a given decrease in stress. These stiffness values include the tie-bar elements of the load frame and the ball screw used to drive the loading column (see supporting information). For comparison, the gas confining media apparatus used by Okazaki and Katayama (2015) is less stiff than our modified apparatus. Thus, we can conduct experiments at similar values of $\frac{K}{\sigma_n}$ (i.e. equation 1.1) as those conducted by Okazaki and Katayama (2015) ; (i.e., (155 MPa/mm)/(200 MPa) = 0.78/mm for the gas apparatus used (Okazaki and Katayama, 2015), and (194 MPa/mm)/(1000 MPa) = 0.19 GPa/mm for our modified apparatus).

In the triaxial apparatus shear and normal stress evolve together (see supporting information). At constant pressure, they both evolve as a function of axial stress σ_1. For simplicity, we report measured quantities axial stress, LVDT2 displacement, and axial stiffness $K_{Apparatus}$ instead of the derived shear quantities. An additional LVDT (referred to as LVDT2 in Figure 1.2) was added below the springs to provide a better measurement of sample displacement (V_{sample}). To present the data in the most straightforward way, in the figures we plot measured values of displacement from LVDT2. In detail, the slopes on these curves show are somewhat greater stiffness because they reflect $K_{Upper\ Column}$ and not $K_{Apparatus}$ (Figure 1.9). Plotting the raw data in this way has no effect on our conclusions.

1.2.4 Data Recording and Treatment

Mechanical data were recorded at 1kHz, then anti-alias filtered and reduced for storage. Precision in load and pressure is 0.1 MPa, while precision in displacement is 0.1 μm. Recorded load and displacement data were converted to shear stress and shear displacement using methods outlined in the data reduction program RIG 1.3 by Matej Pec.

1.3 Results

1.3.1 Mechanical Results

Load versus displacement curves for temperature-ramping experiments (all with a temperature ramp rate of 0.5°C/s) are illustrated in Figure 1.3a. Here we report axial load in MPa by dividing the axial force by the area of the 1/4 inch diameter loading piston. The slopes of the load versus displacement curves for experiments conducted using the unmodified loading column approach, but remain less than, the apparatus stiffness. Similarly, the slope of the load versus displacement curves during weakening for experiments conducted with the modified loading column plot near the modified apparatus stiffness (Figure 1.3a and Figure S2). Calibration experiments (shown in the supporting information) indicate that the higher initial slopes during weakening arise from frictional hysteresis between surfaces of the Belleville springs, and thus the load versus displacement curves in Figure 1.3 also reflect weakening with a slope similar to the machine stiffness.

Even with the significant decrease in apparatus stiffness, the samples unload stably in all experiments. We do not observe stick-slip. We can compare details of the weakening using characteristics outlined in Proctor and Hirth (2015). Plots of displacement rate and weakening rate ($d\sigma_1/dt$) versus time exhibit two peaks during the temperature ramps in both modified-stiffness (Figure 1.4a) and unmodified-stiffness experiments. The first peak initiates just after the onset of the imposed temperature increase (Figure 1.4a, the first peak overlaps with second peak for W2233); previous studies show that this weakening occurs in a similar way under both drained and undrained pore fluid pressure conditions (Proctor and Hirth, 2015), and is interpreted to reflect the effect of temperature on the strength of antigorite. The second peak follows 100-500 seconds later with a higher $d\sigma_1/dt$, and proceeds until the sample weakens to the final strength. The second event is driven by pore fluid produced by the dehydration reaction (e.g. Proctor and Hirth, 2015, as outlined in introduction). The time after the ramp initiation (the x axis in Figure 1.4a) where the

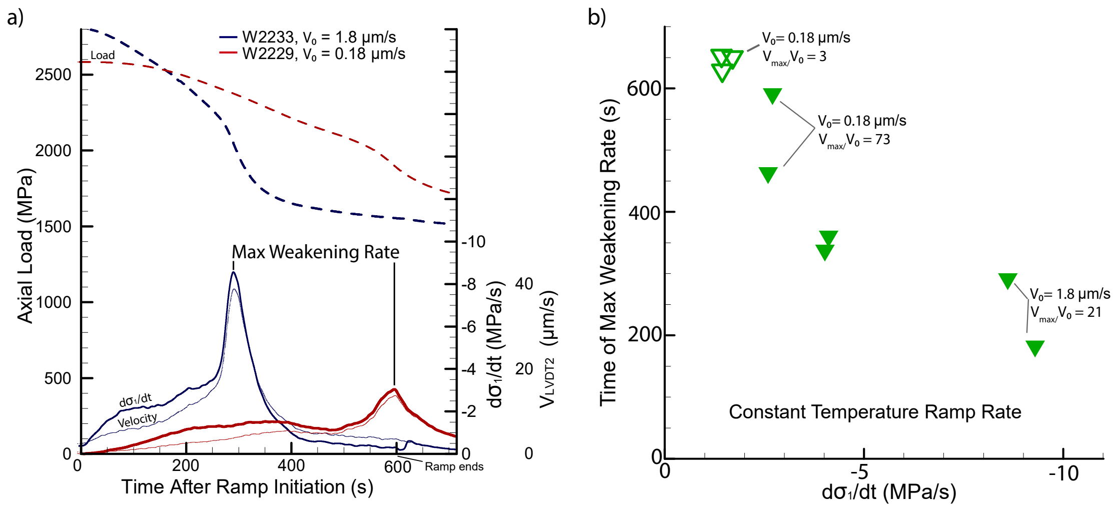

Figure 1.4: (a) Time history of recorded load, velocity, and weakening rate during dehydration. Run conditions are noted in the plot. b) Observed time (after temperature ramp start) of the maximum weakening rate plotted against the magnitude of the maximum weakening rate; the load-point displacement rate (V_0) and V_{max}/V_0 are noted near data points. Open triangles are experiments with the unmodified stiffness, solid triangles are modified-stiffness experiments.

2nd peak in dσ_1/dt is observed is a proxy for the time required to achieve a characteristic reaction extent. The magnitude of the maximum weakening rate (dσ_1/dt) is a proxy for reaction rate. In the discussion section, we distinguish these concepts from complications arising from rate-dependent friction.

While unstable slip is not observed, experiments conducted with the modified stiffness exhibit higher maximum fault displacement rates and a decrease in the time at which the maximum weakening rate occurs. Peak sample displacement rates are 20 to 100 times greater than the imposed displacement rate (V_0) for intervals of 10s of seconds (Figure 1.4a). The time of the maximum dσ_1/dt is plotted against the magnitude of the maximum dσ_1/dt in Figure 1.4b. The experiments with modified stiffness exhibit slightly larger weakening rates and much higher sample displacement rates. In addition, experiments conducted with higher V_0 achieve maximum sample displacement rates 50 and 450 seconds earlier than observed in experiments with unmodified stiffness deformed at the same conditions (Figure 1.4b). Because all of the temperature ramps start at 400°C with the same temperature ramp rate, the shorter time required to achieve the peak slip rate correlates with imposed temperatures that are 25 to 225°C lower.

The maximum weakening rate in our modified-stiffness experiments also increases with an increase in V_0 (Figure 1.5). The weakening rate ($d\sigma_1/dt$) increases by a factor of 3 for a factor of 10 change in V_0. Figure 1.5 illustrates that the maximum weakening rate also correlates with the magnitude of differential stress at the onset of the temperature ramp.

1.3.2 Microstructural Observations

Microstructural analyses of our samples illustrate evidence of dehydration reactions occurring in the deformed samples. SEM micrographs of the sample with the largest observed weakening velocity (W2233, $V_0 = 1.8\mu$m/s) and a hydrostatically annealed sample that experienced the same imposed temperature-pressure protocol are illustrated in Figure 1.6. The deformed sample exhibits spatial variations in forsterite content, indicating variations in reaction extent. The highest reaction extent is observed in the center of the sample adjacent to the high-displacement faults. A high reaction extent inside the fault zone is illustrated by a large fraction of forsterite (33% by area) and porosity (12% by area) in the quenched sample (Figure 1.6). 200 μm outside of the fault zone, the reaction extent is significantly lower (83% unreacted antigorite, 15% forsterite, and 2% porosity, all by area). The forsterite grains are rounded and <2 μm in diameter, often in bands oriented parallel to the fault zone. Outside of the primary fault zone forsterite grains with similar diameter form but are concentrated in pores between grains. Similar microstructures, but with smaller reaction extents, are shown for samples deformed with lower V_0 (W2230, V_0 = 0.54 m/s; W2229, V_0 = 0.18 μm/s (Figure 1.7). All of these samples illustrate significantly greater reaction extent than that observed in samples of antigorite deformed with the unmodified stiffness using the same temperature ramp protocol (e.g., sample W1892 from Proctor and Hirth (2015)).

To investigate microstructures associated with the onset of reaction weakening, some experiments (all with 45° pistons at V_0 =1.8 m/s) were quenched before the imposed temperature

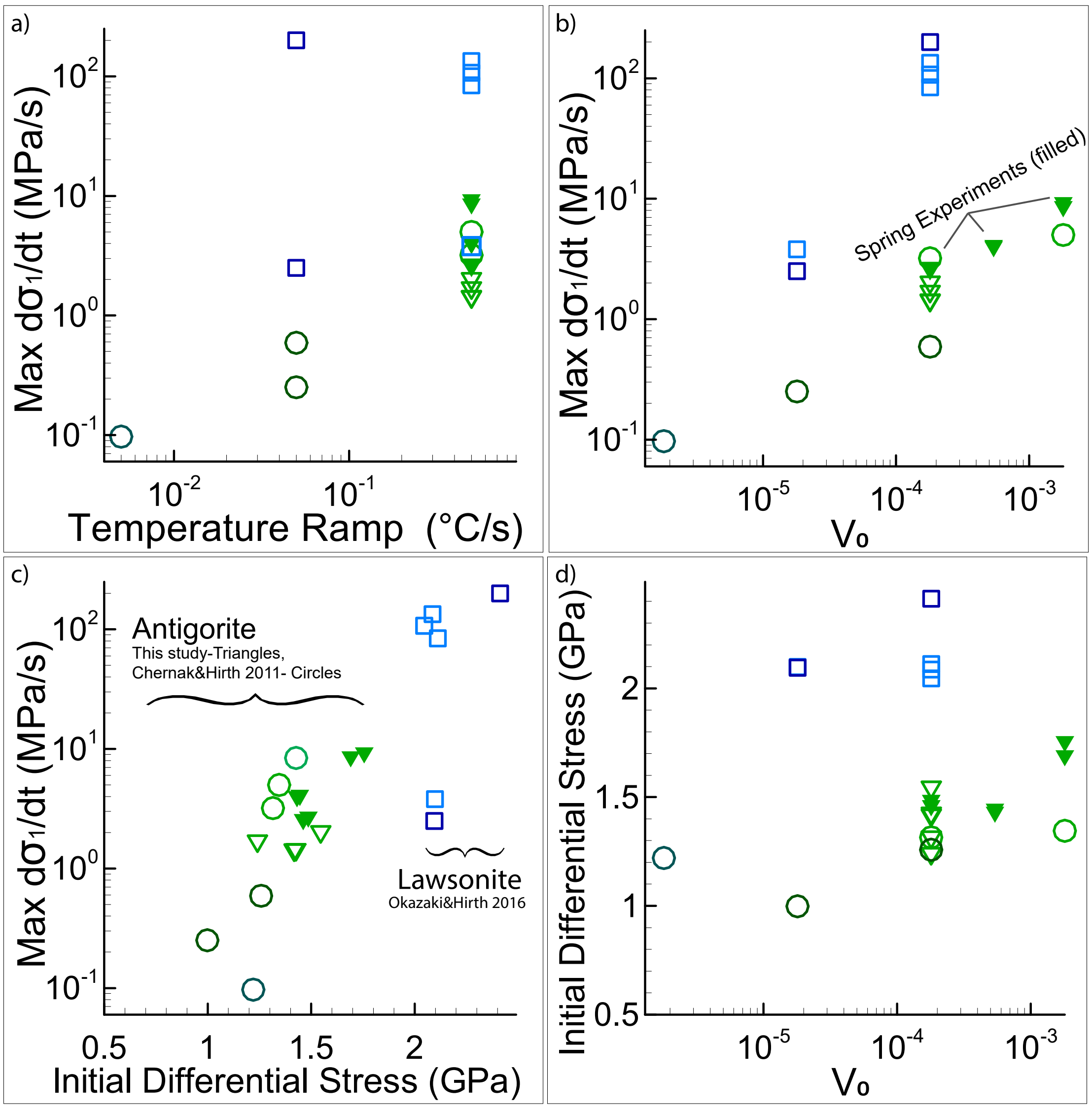

Figure 1.5: Open symbols are runs with unmodified stiffness. Circles are Antigorite data from Cernak and Hirth 2011, squares are Lawsonite data from Okazaki and Hirth 2016 for comparison, and triangles are this study. Darker shades of color for each materials denote a lower ramp rate. (a) Plot of maximum weakening rate vs. temperature ramp rate. (b) Plot of maximum weakening rate vs. imposed load-point displacement. (c) Plot of weakening vs. differential stress at the initiation of temperature ramping. (d) Plot of initial differential stress vs. imposed load-point displacement rate.

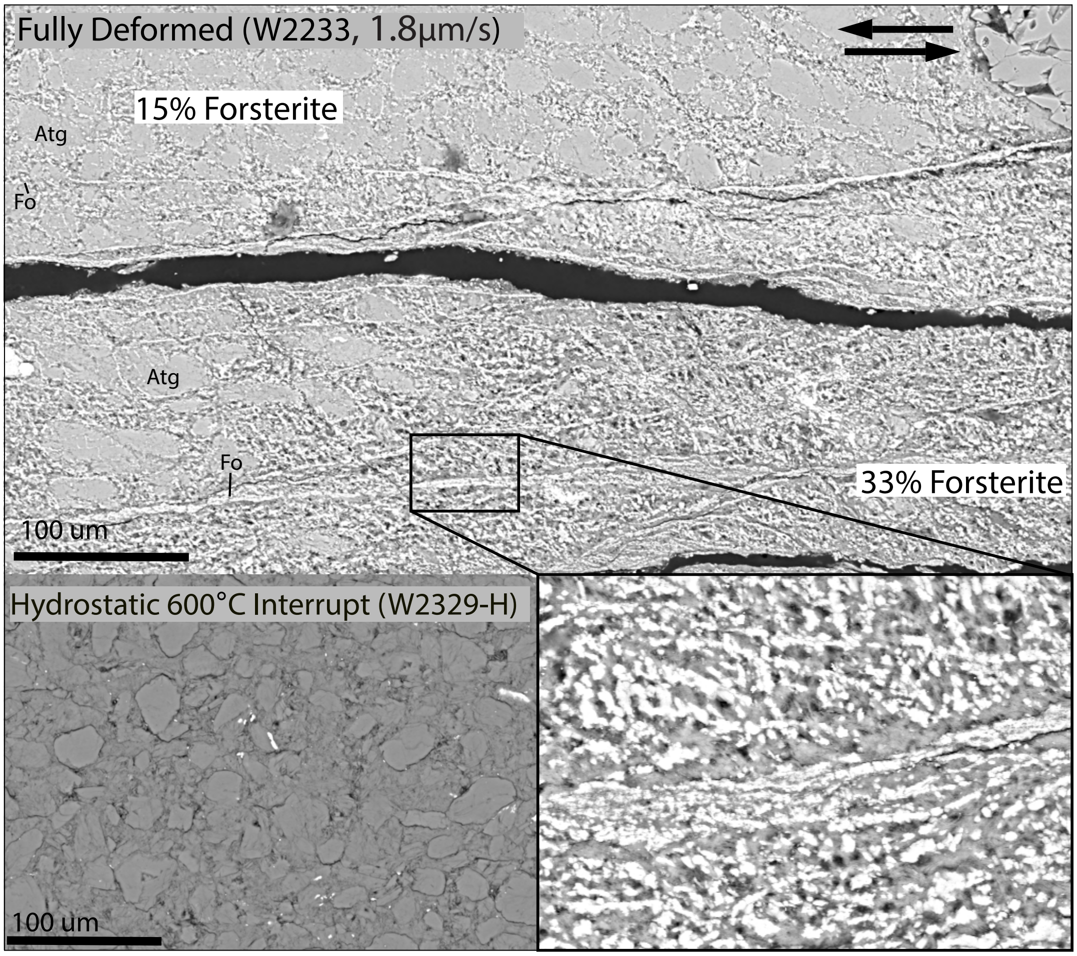

Figure 1.6: Images of a deformed sample containing high forsterite (Fo) content (a proxy for reaction extent visible in electron imaging) and porosity that decreases away from fault surfaces, as well as a reference hydrostatic sample conducted with the same temperature protocol with no visible reaction products. Noted fractions are area percent.

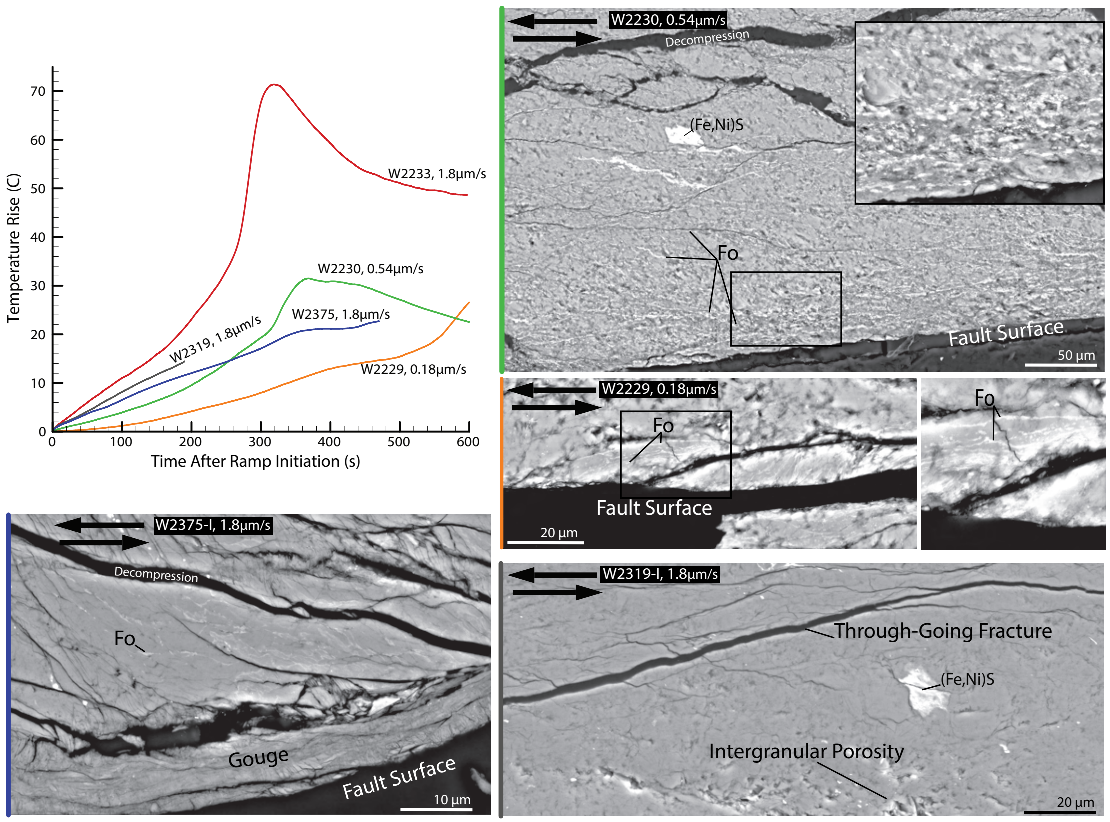

Figure 1.7: Plotted: Predicted temperature rise above imposed (ramping) temperature as a function of time calculated from supporting information equation 1.4. The highest temperature and reaction extent occur in experiment W2233-0.2-4 which is featured in Figure 1.4a. Images: Recovered fault surface microstructure of several samples where reacted forsterite content (Fo) is highlighted: W2230, W2229, W2319-I, and W2375-I (clockwise).

reached 700°C. These samples show the development of localized shear zones along fractures oriented in the R1/Reidel shear orientation. The sample quenched after the smallest amount of displacement shows localized deformation and no evidence for reaction (Figure 1.7 W2319-I, quenched at 500°C). While more difficult to resolve relative to the higher displacement samples, small amounts of reaction products are observed in the gouge zone of the fault that formed in the sample quenched at the onset of weakening (Figure 1.7 W2375-I, quenched at 600°C). In contrast, a hydrostatically annealed sample (W-2329-H) that was quenched at 600°C after the same imposed temperature-pressure protocol as W2375-I shows no reaction products (Figure 1.6). In addition, there is minimal evidence for crushing or alignment of the antigorite grains in the hydrostatic sample.

The samples deformed with the modified stiffness experience large fault displacement – a direct result of the difference in stiffness. The highest reaction extents are observed within the center of the samples along the fault zones. The outer edges of the samples exhibit much lower reaction extents, indicating that the reaction extent is not a reflection of translation of the sample closer to the graphite furnace.

1.4 Discussion

Even with the reduced apparatus stiffness, we do not observe stick-slip events which would be expected if the dehydrating antigorite gouge obeyed rate-and-state friction and was velocity-weakening (given the observations from Okazaki and Katayama (2015)). Based on comparison with these lower pressure experiments, our observations indicate that the frictional behavior of antigorite changes at high confining pressure for a given temperature and strain rate. Such a transition may arise owing to the activation of rate-strengthening deformation processes, in response to both the higher stresses required for deformation and higher temperatures due to a positive Clapeyron slope of the dehydration reaction up to 1 GPa confining pressure. Consistent with these interpretations, at the conditions of our experiments, rate-strengthening deformation has been reported for antigorite gouge, both within its stability field (Proctor and Hirth, 2016) and during dehydration (Chernak and Hirth, 2011).

While we do not observe stick-slip, our results highlight positive feedbacks between slip velocity and reaction weakening rate that are enhanced in the experiments conducted with the modified stiffness. In the following sections we discuss how these observations that indicate these feedbacks arise from shear heating.

1.4.1 Effects of Temperature Ramp Rate, Imposed Velocity on Weakening of Antigorite and Lawsonite

In contrast to our observations for antigorite, Okazaki and Hirth (2016) found that dehydration reactions in lawsonite generate stick-slip events. As outlined below, comparing observations for these materials suggests that the contrasting behaviors during dehydration arise from the differences in the rate-dependence of friction of the reacting materials.

First, the maximum weakening rate in antigorite correlates strongly with temperature ramp rate (Figure 1.5a). This observation indicates that weakening rate in antigorite is controlled by reaction rate that leads to continual pore fluid pressure generation during temperature ramping (Proctor and Hirth, 2015). We repeated unmodified-stiffness experiments on antigorite (open triangles) and reproduce trends from previous work. In contrast, no clear trend in shown for lawsonite in Figure 1.5a, indicating an apparent decoupling between weakening rate and reaction rate.

Second, for a given temperature ramp rate, the weakening rate increases with V_0 for both antigorite and lawsonite, with the effect more prominent for lawsonite (Figure 1.5b). The initial differential stress (i.e., before temperature ramping) increases with V_0 for antigorite (Figure 1.5d). In contrast, V_0 appears to have little influence on the differential stresses before temperature ramping for lawsonite, although the stresses are approximately two times greater than those for antigorite (Figure 1.5c). From these observations, we conclude that the weakening process for lawsonite (which leads to unstable stress drops) must involve rate-insensitive or weakening friction, in conjunction with critical stability conditions (i.e., equation 1.1) that are close to our starting conditions (as concluded by Okazaki and Hirth, 2016). In contrast, the velocity strengthening nature of the antigorite friction appears to inhibit instability.

Third, the relationships shown in Figures 7b and 7c for antigorite indicate dissipative processes lead to faster reaction rates – and faster, but apparently stable weakening. In the next section we discuss the roles of rate-dependent friction and pore-fluid weakening on the rate sensitivity of slip during dehydration.

1.4.2 Rate Sensitivity of friction during Pore-fluid Driven Weakening

Closer inspection of our data reveals evidence for a rate-weakening effect associated with reaction (likely shear heating). To illustrate this behavior, we outline the expected effects of reaction weakening and stiffness on sample strength and slip velocity using a frictional slider-block model. Equation (1.2) can be applied to our tri-axial experiments (for which axial load and axial displacement are measured) using standard linear relationships that account for the angle of the fault zone. At the same conditions as our experiments, Proctor and Hirth (2015) establish that equation (1.2) describes the evolution of strength during dehydration by comparing drained ($P_f = 0$), partially drained, and undrained (i.e., sealed) experiments.

The influence of slip velocity on weakening rate during dehydration can be evaluated by comparing experimental data to the result expected for a reference scenario where (a) frictional resistance is assumed to be rate-independent and (b) dτ/dt is fixed by the change in pore fluid pressure resulting from the dehydration reaction driven by the imposed temperature ramp. With this scenario, dτ/dt (and thus dσ_1/dt) would not be affected by the change in apparatus stiffness (K), and K would govern the relationship between changes in force and changes in displacement (eq. 3). If V_0 is much less than the sample slip velocity (as observed in our experiments), a ten-fold reduction in stiffness K results in a proportional ten-fold increase in sample slip velocity; this scenario is illustrated schematically in Figure 1.8a. In our experiments we observe that dσ_1/dt is not constant, and in fact increases (i.e. weakening occurs more rapidly, Figure 1.8c) with modified stiffness and, further, that dσ_1/dt increases with larger V_0 (Figure 1.5b). These observations indicate a positive feedback between sample slip velocity and weakening rate (i.e., shear heating,

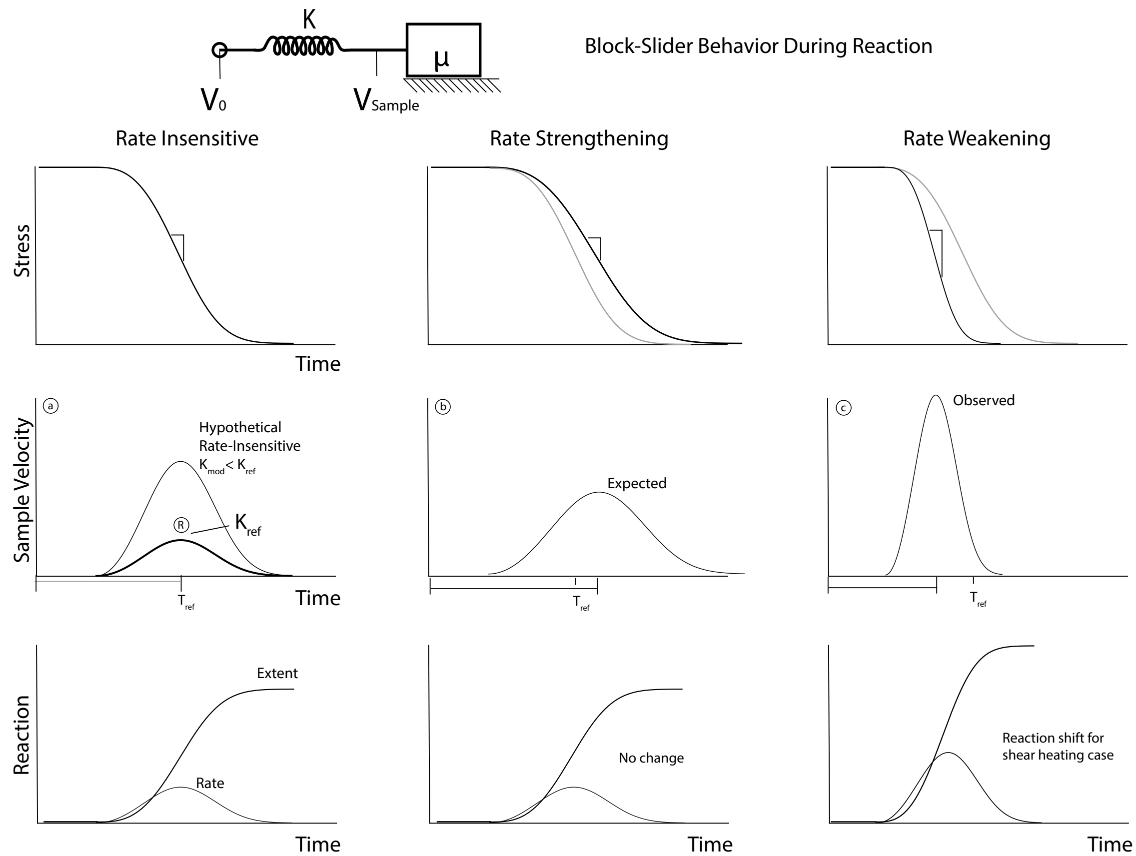

Figure 1.8: Schematic plots of stress and slip velocity for a block slider with strength evolution controlled by the change in pore fluid pressure during dehydration (equation 1.2). (a) Velocity response of an unmodified reference case R, and the predicted response of a rate insensitive system where K is changed. Velocity response is directly proportional to the ratio between standard and modified compliance (1/K) by equation (1.2) (b) Expected response of a velocity strengthening material to pore-fluid driven weakening. Rate strengthening is enhanced by extra displacement released during weakening serving to “hold-back” (delay) the weakening velocity and magnitude. This behavior is not observed in our experiments. (c) Expected response of a velocity weakening material to pore fluid driven weakening. Increased velocity enhances weakening, causing peak weakening rate to happen earlier. Reaction rate is also modified to match weakening mechanism of microstructural observations.

possibly in combination with other dissipative weakening processes as outlined further below; Figure 1.8c). The rate-weakening scenario in Figure 1.8c also indicates that the maximum weakening rate will occur earlier in the temperature ramp (relative to the reference case), consistent with our results shown in Figure 1.4a. As noted above, previous work indicates that the antigorite gouge is rate-strengthening in constant temperature testing at the conditions of our experiments. The observation that the peak differential stress achieved prior to the initiation of the temperature ramp increases with increasing V_0 is also consistent with velocity-strengthening behavior (Figure 1.5c). The expected scenario with rate-strengthening is illustrated in Figure 1.8b. Here, the peak weakening rate would be delayed relative to the reference case, while the relationships for the reaction rate and reaction extent remain unchanged. Clearly, our results are inconsistent with the expected scenario for rate-strengthening friction with constant reaction rate. This observation indicates that weakening during experiments with the modified-stiffness must be promoted by an enhanced reaction rate (to overcome the intrinsic frictional behavior of the antigorite), which is schematically illustrated at the bottom of Figure 1.8c; this leads to an earlier onset of the maximum weakening rate (as shown in Figure 1.4a) and a greater reaction extent (as illustrated in Figure 1.7).

1.4.3 Weakening by Shear Heating

Based on the observations outlined in Figures 1.5 and 1.8, and our microstructural observations, we hypothesize that weakening rate is enhanced by shear heating in our modified stiffness experiments. While the temperature surrounding the sample is fixed, our observations indicate the action of local heating and deformation driven reaction. The local temperature rise increases the reaction rate, and therefore the onset time when evidence for the reaction is observed. The local temperature rise above the imposed-ramp temperature were estimated using a thermal model for deforming gouge presented in Proctor et al. (2014), described in the supporting information. As shown in Figure 1.7, the peak temperature increase predicted for the experiments that show the greatest reaction extent is more than twice that predicted for the experiments that show lower reaction extent. In addition, experiments that were quenched prior to the rapid slip event show no reaction products, and the experiment quenched at the onset of rapid slip shows small amounts of forsterite near and along fault surfaces. The estimates of the temperature rise are generally consistent with our hypothesis that reaction weakening is enhanced by shear heating. For example, the calculated temperature rise of 70°C at 300s shown in Figure 1.7 indicates that the fault zone temperature reached 620°C (i.e., 400°C+0.5°C/s*300s+70°C), while the short-term thermal stability of antigorite at our conditions is above 600°C. At face-value, the magnitude of the calculated temperature rise is too small to promote the amount of reaction that we observe based on the predicted thermal stability of antigorite at our experimental conditions. Although some hydrostatic experimental studies show evidence for full antigorite dehydration at around 620°C (e.g. Wunder and Schreyer, 1997), these hydrostatic tests are conducted over several days and are often seeded with product crystals (talc or forsterite) that enhance reaction rates. Deformation experiments such as ours typically report broadly observable reaction at higher temperatures (700°C) and do not report evidence of talc in reaction products (Chernak and Hirth, 2011, Gasc et al., 2017). The thermal model may underpredict the temperature rise because it does not incorporate the possible effects of a decrease in thermal conductivity resulting from a fluid-filled porosity. It is also possible that the reaction rate is enhanced during deformation by an increase in reactive surface area (resulting from gouge formation and microcracking), the role of crystal defects and specific surface energy on changing the reaction boundary, and local decreases in fluid pressure associated with microcracking (e.g. Milsch et al., 2003; Takahashi et al., 2011; Ferrand et al., 2017; French et al., 2019). Nonetheless, the overall agreement between the observed mechanical behavior with the inclusion of the modified stiffness set-up, the thermal model, and the observed reaction extent all support shear dissipation increasing reaction rate (c.f., Brantut and Sulem, 2012). The high extent of reaction we observe also highlights the role of deformation in promoting the reaction. To estimate the kinetic time/temperature to attain 33% forsterite reacted microstructure (i.e., the area fraction amount observed along the fault surface illustrated in Figures 1.6 & 1.7) we compare our results to reaction extents observed in hydrostatic experiments (e.g. Sawai et al., 2013; Proctor and Hirth, 2016; Rutter et al., 2009). All three of these studies report reaction extents similar to what we illustrate in Figure 1.6, but over a time of at least 24 hours above 650°C. In contrast, the same reaction extent is observed locally in our deformation experiments below 650°C with a duration of only 0.15 hour (emphasizing that no observable reaction products are observed in our control hydrostatic tests quenched after 0.15 hour while following the same temperature ramp protocol).

1.5 Conclusions and Geophysical Implications

Antigorite dehydration experiments were run with modified apparatus stiffness and show evidence for shear heating enhanced weakening at 1 GPa confining pressure. Compared to reference unmodified stiffness dehydration runs of the same thermal conditions, the rate at which the dehydrating samples with modified stiffness weaken ($d\sigma_1/dt$) increases by a factor of two. Time of peak weakening rate decreases with increasing peak weakening rate magnitude indicating shear enhancement of the dehydration reaction due to modified stiffness and increasing imposed load-point displacement rates. Recovered microstructure suggests strongly enhanced reaction rates, indicated by increased reaction extent relative to unmodified stiffness experiments and decreasing reaction extent away from primary slip surfaces. No stick-slip activity was recorded, but the shear heating mechanism identified scales inversely with stiffness and could generate fast slip in subduction zones. The lack of stick-slip instabilities suggests that dehydrating antigorite gouge at high pressure would not lead directly to rapid rupture, but rather favor accelerating slow slip that scales with stiffness and therefore rupture size (Dieterich, 1979).

Acknowledgments

We thank John Wheeler and an anonymous reviewer for their constructive comments. We thank Hannah Rabinowitz for initial feedback on the manuscript. We also thank Keishi Okazaki, Nicolas Brantut, and Yuval Boneh for helpful discussions of the work. This work was supported by NSF EAR-1315784 and EAR-1513714. Data associated with this paper are available through the Brown University Digital Repository (https://doi.org/10.26300/ks4j-dg34).

Experiment Name	Confining Pressure	Start Temperature	Ramp Rate	Quench Temperature	Column Stiffness	Imposed Displacement Rate	Sawcut Piston Angle	Displacement at Peak Weakening or Interrupt
	(GPa)	(°C)	(°C/s)	(°C)	(GPa/mm)	(μm/s)	(°)	(mm)
W1968	1	400	0.5	700	1.98	0.18	45	0.15
W2092	1	400	0.5	700	1.98	0.18	45	0.18
W2140	1	400	0.5	700	1.98	0.18	45	0.16
W2229	1	400	0.5	700	0.21	0.18	45	2.20
W2230	1	400	0.5	700	0.21	0.54	45	1.93
W2233	1	400	0.5	700	0.21	1.8	45	2.40
W2235	1	400	0.5	700	0.21	0.54	45	1.17
W2267	1	400	0.5	700	0.21	0.18	30	3.4
W2268	1	400	0.5	700	0.21	1.8	60	1.6
W2317-H	1	400	0.5	400	0.21	0	45	0
W2319-I	1	400	0.5	500	0.21	1.8	45	1.18
W2329-H	1	400	0.5	600	0.21	0	45	0
W2331-I	1	400	0.5	600	0.21	1.8	45	1.90
W2375-I	1	400	0.5	610	0.21	1.8	45	1.80

1.6 Supporting Information

1.6.1 Thermal Model

The temperature rise predicted for the center of deforming gouge layer was calculated using an analytical expression that considers distributed shear work and thermal conduction.

$$T\left(y,t\right) = T_0 + \int_0^t \frac{\tau\left(t'\right)V\left(t'\right)}{\rho c\sqrt{2\pi}} \frac{1}{\sqrt{W^2 + 2\alpha_{th}\left(t-t'\right)}} exp\left(-\frac{y^2}{2W^2 + 4\alpha_{th}\left(t-t'\right)}\right) dt' \tag{1.4}$$

The details are described in Proctor et. al (2014). The shear stress (τ) was calculated as half of the differential stress. We are interested in peak temperature so we report values for y = 0. Velocity (V) was calculated for the shear surface of the 45° saw-cut piston from the axial displacement rate of the sample (V_{sample}). In the calculations we use a deforming gouge layer half-width (W) of 100 μm, a thermal diffusivity (α_{th}) of 10^{-6} m2/s, and a volumetric heat capacity (ρ_c) of 2.7x10^6 Pa/°C (Proctor et. al 2014). The half width only becomes important when W^2 is much larger than $\alpha_{th}\left(t-t'\right)$, i.e., at very short times, or very large W. With large W, the heat is already widely distributed so thermal diffusivity is less important, and at short times heat cannot migrate quickly so temperature rise is strongly dependent on amount of material the heat is generated in. For reference, shear and normal (σ_n) stresses in triaxial geometry can be computed with relationships for Mohr's circle from Jaeger et. al. (2007), where axial force is σ_1 and confining pressure is σ_3.

$$\tau = \frac{\sigma_1 - \sigma_3}{2} sin(2\theta) \tag{1.5}$$

$$\sigma_n = \frac{\sigma_1 + \sigma_3}{2} - \frac{\sigma_1 - \sigma_3}{2} cos(2\theta) \tag{1.6}$$

Temperatures were calculated with area corrected shear stress. The area correction is calculated with a relation for the overlap of two ellipses presented in the RIG 1.3 by Matej Pec. The contact area change can be calculated as a function of piston shear.

$$contact\ length = \ c\ = \frac{shear\ displacement}{starting\ shear\ length}\ = \frac{\Delta x_{axial}}{Diameter} tan(\theta) \tag{1.7}$$

where θ is angle between the saw-cut and piston axis. The area is then calculated as:

$$\frac{A}{A_0} = 1 - 1.2082 \ \times c \ - \ 0.19134 \ \times c^2 \ + \ 0.39461 \times c^3 \tag{1.8}$$

$$\tau_{corrected}(t) = \tau_{measured}(t)\frac{A_0}{A} \tag{1.9}$$

Sample temperatures do not significantly lag the temperature ramp set point. This can be estimated based on solutions for diffusion in an infinite cylinder. For this calculation we use an alumina thermal conductivity of $10^{-5}m^2$/s because the shearing pistons make up most of jacketed cylinder's volume. The thermocouple is 3 mm away from the center of the sample. The center of the sample will reach 98% of an instantaneous temperature change in less than 1s (based on a normalized time of $0.8 = \alpha_{th\ Al2O3}t/0.003^2$; Figure 12, Carslaw and Jaeger, 1959). For example, if we could instantaneously increase surface temperature by 300°C, the center of the sample would reach 294 °C in 0.8 seconds. Thus, for a temperature ramp rate of 0.5°C /s the temperature will not lag behind the setpoint by more than 1°C over the duration of the temperature ramp (which is on order of the error in our temperature measurement).

1.6.2 Compliance with the general shear assembly

The area offset on the shear pistons used in the general shear geometry affects both stress state (as noted above) and the effective shear stiffness (i.e., the change in gouge stress with shear displacement). As the sample slips during weakening, the spring unloads, but area between the pistons is also getting smaller. This effectively decreases sample stiffness. While the overlapping area of the pistons is getting smaller between pistons, the force/displacement relationship of the spring stays the same, leading to an increase in the instantaneous stiffness of the column (this is a competing effect). As slip continues, the change in overlapping area with displacement decreases ($dA_{overlap}/ds$ decreases). In our experiments, rapid slip and the onset of reaction starts after relatively low displacement, so this effect does not affect our conclusions.

1.6.3 D-DIA Stiffness

The stiffness of the D-DIA apparatus was calculated from elastic stiffness of steel deformation anvils and hydraulic fluid compressibility. First, the frame is assumed to be infinitely stiff. The hydraulic ram radius is 44.5 mm, and total stroke is 20 cm^3 (Wang et al., 2003). Bulk modulus of the oil is assumed to be 1.5 GPa. Compressing this volume of oil to 50 MPa with the ram would lead to ram force of 311 kN and displacement of 0.333 mm. On a 1.2mm diameter sample used in Hilairet et al (2007) this is 275 GPa which results in a stiffness of 825 GPa/mm. The same calculation from specification given in Ferrand et al 2017, with a 2.1 mm diameter sample gives a stiffness of 270 GPa/mm. The internal steel ram stiffness can be estimated approximately as a cone with diameters 10 mm and 90 mm. Integrating displacement along the cone length with elastic modulus of 200 GPa gives elastic displacement of 0.99 mm at 311 kN for a stiffness of 278 GPa/mm and 91 GPa/mm respectively (1.2, 2.1 mm diameter). The composite stiffness (combining the hydraulic stiffness and the steel ram stiffness) for Hilairet et al. 2007 condition is 208 GPa/mm; this is the value quoted in the text of our paper. Substantial uncertainty exists due to friction in the sample assembly so effective stiffness on the sample could be much larger.

1.6.4 Measurement of apparatus, column, and spring stiffness

Disambiguation of measured stiffnesses is important for interpretation of data and comparison to other studies. It is simple to consider the stiffness of the whole rig as a loop of springs, with the frame expanding/returning and the loading column compressing/expanding as load changes in the loop due to advancing/retracting the ball screw or slipping the sample, respectively. Our LVDTs are positioned close to, but not directly on the sample (see Figure 1.2 and Figure 1.9). This divides the stiffness of the whole rig, $K_{apparatus}$, into two halves: $K_{upper\ column}$ and $K_{lower\ column}$.

We can introduce displacement in either section of the loop to measure elastic stiffness of the other half (e.g. ball screw to measure to lower pistons and anvil, or hydraulic jack in place of sample to measure springs, load cell, ball screw, and frame). In Figure 1.9, the ball screw displacement is noted as x_0 and the sample or hydraulic jack displacement is noted as x_{sample}. The

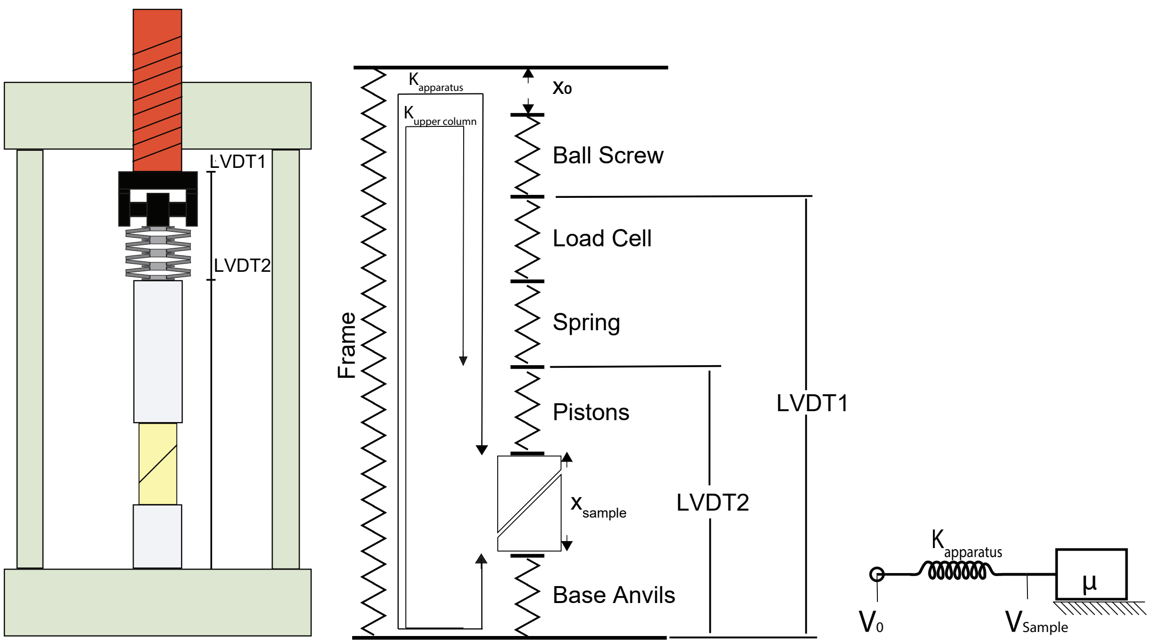

Figure 1.9: Schematic drawing of the components of the loading frame and column drawn in a realistic style and a typical 1D mechanics style alongside the typical schematic of a 1D rate-state friction slider block model. Change in displacement of all the loading elements (zigzag lines) for a change in sample load need to be accounted for to form the typical $K_{Apparatus}$ used in rate-state models.

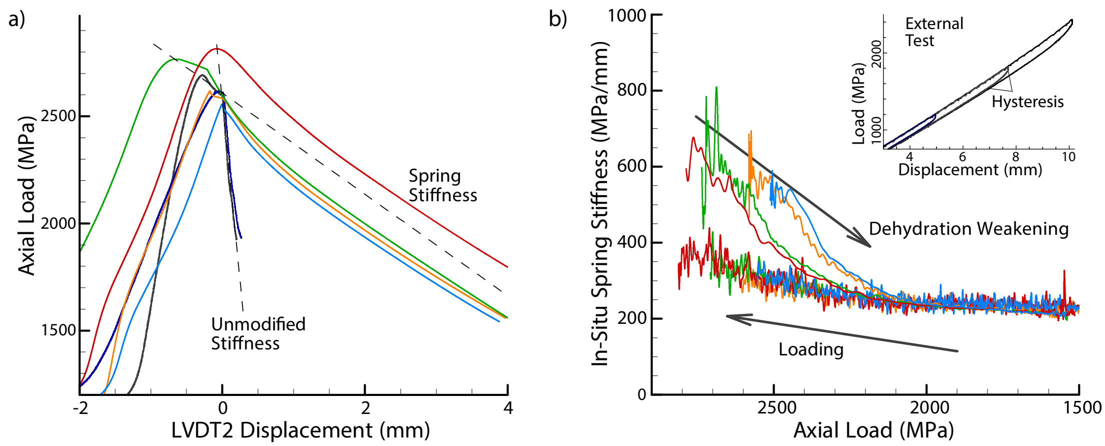

Figure 1.10: Figures summarizing recorded load, displacement, and their derivative relationship (stiffness). (a) Load plotted against displacement for dehydration runs, with displacement referenced to the recorded value at initiation of the temperature ramp. Dashed reference lines are plotted for the static stiffness of the standard and modified apparatus. (b) Absolute value of instantaneous absolute spring stiffness measured for the load-displacement curves in (a) (both loading and weakening). Inset shows separate results of calibration experiments on only the spring elements using a hydraulic press; the frictional hysteresis matches the observed unloading behavior during the dehydration experiments.

Table S1: Measured load-displacement for each element in the modified apparatus

	Stiffness (kN/mm)	Axial Stiffness (1/4" OD MPa/mm)	Compliance (mm/MPa)
Lower Column			
Base	3153.63	99578.64	1.00E-05
Base carbide	7480.55	236204.72	4.23E-06
σ_1 steel piston	363.74	11485.39	8.71E-05
σ_1 0.5" WC	1496.11	47240.94	2.12E-05
σ_1 0.25" WC	748.05	23620.47	4.23E-05
Sample	3647.36	115168.53	8.68E-06
Upper Column			
Ball Screw	311.36	9831.46	1.02E-04
Frame	489.28	15449.44	6.47E-05
Load cell	845.12	26685.39	3.75E-05
Spring	6.62	209.00	4.78E-03
Lower total	182.50	5762.69	
Upper total	6.35	200.46	
Apparatus total	6.14	193.72	
Unmodified Upper	94.88	2995.94	
Unmodified total	62.43	1971.16	

Figure 1.11: Apparatus compliance measurements.

resulting combination of the stiffness of the two halves is the value that the sample responds to ("feels") during slip (or propagation of instabilities) so the combination of the whole loop (Kapparatus) should be used for assessment of stability. Mathematically the stiffnesses can be expressed as:

$$K_{Measured} = \frac{dF}{dx_{LVDT2}} \tag{1.10}$$

$$\frac{1}{K_{Lower\ Column}} = \frac{1}{K_{Pistons}} + \frac{1}{K_{Base\ Anvils}} \tag{1.11}$$

$$\frac{1}{K_{Upper\ Column}} = \frac{1}{K_{Frame}} + \frac{1}{K_{BallScrew}} + \frac{1}{K_{Load\ Cell}} + \frac{1}{K_{Disk\ Springs}} \tag{1.12}$$

$$\frac{1}{K_{Apparatus}} = \frac{1}{K_{Lower\ Column}} + \frac{1}{K_{Upper\ Column}} \tag{1.13}$$

For simplicity, our rig schematic omits the hydraulic ram, which applies 1 GPa pressure to our 1 inch diameter pressure vessel. This omission is negligible if pressure remains constant or varies by only a small amount. We satisfy this condition by ramping temperature at 0.5°C/s, which produces only a small change in pressure. In contrast, if pressure changes by a large amount (100 MPa -> 100 µm expansion) over a short period (for example, in 1 minute for a temperature ramp rate of 5°C/s at $V_0$2µm/s), the hydraulic ram force adds to frame expansion and pushes the top platen up. The upward motion is applied in the opposite direction of ball screw displacement (V_0) which changes effective V_0 substantially and can even unload samples.

Okazaki et al. (2015) choose to report their stiffness as a shear quantity so it needs to be converted to an axial quantity for comparison. Their reported effective force-displacement from stress drops in the supplement is 80kN/mm on 20 mm diameter pistons which have an area of 314 mm^2 which results in an axial stiffness of 254 MPa/mm. The reported shear stiffness in the main text can be converted to axial stiffness by using constant pressure derivatives of equation 1.5 and conversion of shear to axial displacement ($cos(\theta)$). The conversion of their stated 58 MPa/mm shear stiffness to axial stiffness results in axial apparatus stiffness of 155 MPa/mm. They do not draw a stiffness diagram or note at which two points on their machine the displacement is measured, so it is unclear whether 155 MPa/mm is the entire machine ($K_{Apparatus}$) or another value. Nonetheless we use 155 MPa/mm for a relative comparison.

1.6.5 Nonlinear Elastic Spring Behavior

During dehydration experiments with the modified stiffness, the initial weakening occurs with a steeper slope in the recorded load-displacement curves (Figure 1.10a). We isolated the load displacement relationship for the Belleville disk spring stack during these experiments by taking the difference in displacement between LVDT1 and LVDT2. We found that the spring stack was the source of the nonlinear elasticity, with an initially large drop in force/load after either weakening or unloading started. This is a known effect in Belleville disk spring stacks due to frictional contact between the disks. We confirmed this hysteresis by compressing the stack (instrumented with a direct LVDT) in an external press (Figure 1.10b).

1.6.6 Notes on Relationships Among Unloading Slope, V_0, and Unloading Rate

To investigate the influence of dehydration reactions on weakening slope, we analyze stress relaxation of a frictional slider-block in the context of previous work that focused on relationships among measured $\frac{dF}{dx_{LVDT}}$, V_0, reaction rate, and $K_{upper\ column}$, (referred to for this section as just K) stiffness (e.g., Okazaki et al. 2016, Chernak et al. 2011; Figure 1.12). For quasi-static (no effect of inertia) conditions, the change in force during weakening of a slider block is directly proportional to the apparatus stiffness (K):

$$\frac{dF}{dt} = K_{upper\ column}\,(V_0 - V_{LVDT2}) \tag{1.14}$$

which can be rearranged to define a relationship for the sample displacement rate: $V_{LVDT} = V_0 - \frac{dF}{dt}\frac{1}{K}$. The unloading slope is determined from the observed change in force and displacement, which from substitution for V_{sample} can be written as:

$$\frac{dF}{dx} = \frac{\frac{dF}{dt}}{\frac{dx}{dt}} = \frac{\frac{dF}{dt}}{V_{LVDT}} = \frac{\frac{dF}{dt}}{V_0 - \frac{dF}{dt}\frac{1}{K}} = K\frac{\frac{dF}{dt}}{V_0 K - \frac{dF}{dt}} \tag{1.15}$$

Equation (1.15) has three regimes: (i) with $V_0 K \gg \frac{dF}{dt}$, the unloading slope approaches $\frac{\frac{dF}{dt}}{V_0}$ (with the limiting case of dF/dx = 0 for steady state sliding); (ii) an intermediate regime which follows equation (1.15); and (iii) with $V_0 K \ll \frac{dF}{dt}$, the unloading slope approaches K (a limiting case that includes scenarios related to stick-slip (i.e., large dF/dt) or stress relaxation with a fixed loadpoint (i.e. Vo 0). As illustrated in Figure 1.12, the experiments showing stable slip during dehydration of antigorite (Chernak et al. 2011, Okazaki et al. 2016) fall in either regime (i) or regime (ii); the unstable slip associated with dehydration of lawsonite (Okazaki et al. 2016) falls in regime (iii) for a limiting case in which stick-slip is observed; and the unloading slope observed in our new experiments with the modified stiffness falls in regime (iii) for the limiting case of an effectively fixed load point displacement. For comparison to earlier work, the data from these studies are summarized in Figure 1.12 on a plot of dF/dx versus temperature ramp rate over strain rate.

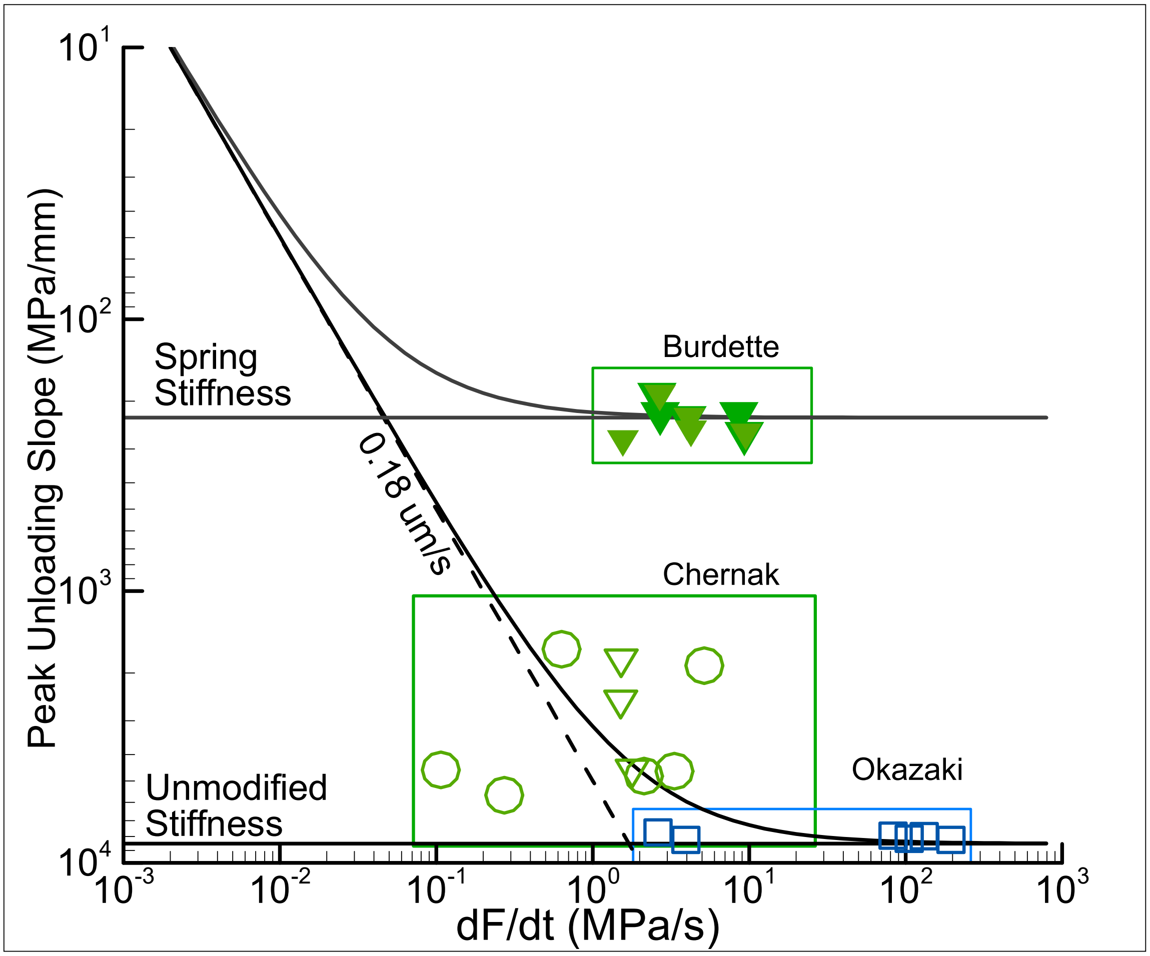

Figure 1.12: Mechanical description of apparatus unloading during sample weakening following equation 1.3. Peak weakening slope calculated from compliance is plotted against unloading rate to illustrate the transition between regimes and where previous experimental work trends relative to this work. Open symbols are unmodified apparatus runs. Circles are data from Chernak and Hirth (2011), squares are lawsonite runs from Okazaki and Hirth (2016), inverted triangles are this work. Note reference $K_{uppercompliance}$ is 3x larger than quoted in this study due to placement of LVDT1 used in these older studies.

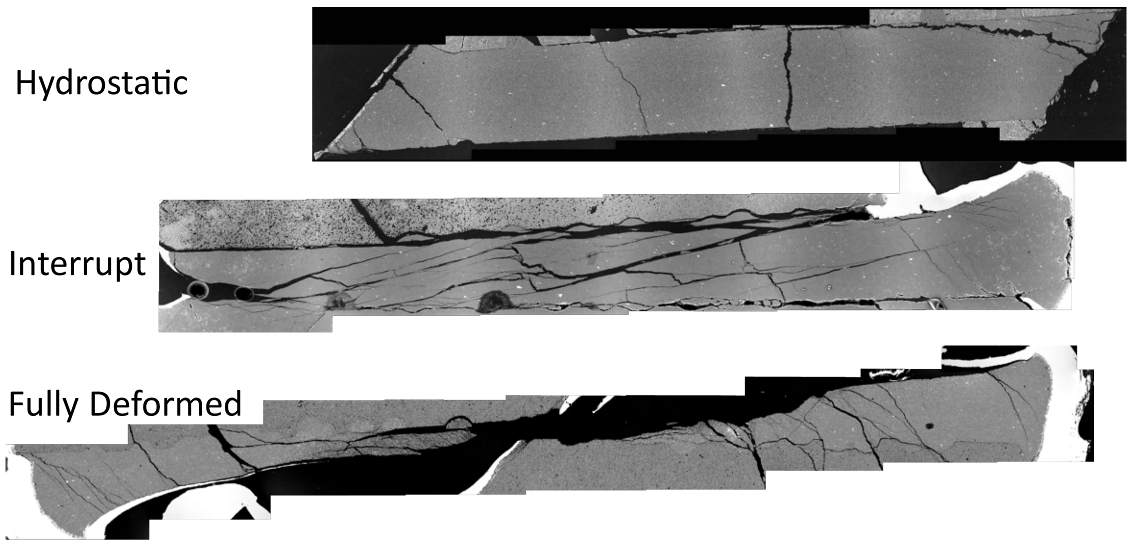

Figure 1.13: Modified compliance dehydration specimens showing deformation patterns and reacted zones. Upper two images show samples that were quenched after ramping from 400-600°C, while the bottom micrograph was quenched after the sample was fully relaxed after ramping to 700°C. The uppermost image was hydrostatically loaded and preserves initial grain shapes with no signs of reaction evident. The middle image (W2319) shows formation of localized fracture bands along the R1 shear direction which accommodate most of the sample slip (see Figure 1.7). The lower image shows a high displacement deformed sample (W2333), with darker areas near the center of the specimen showing high reaction extent.

Chapter 2

Antigorite Creep at Subduction Conditions: Long Duration, High Accuracy Rheological Tests On Intact Cores Using Re-Designed Griggs Assemblies

Eric Burdette and Greg Hirth

[1]Department of Earth, Environmental and Planetary Sciences, Brown University, Providence, RI, USA

Key Points:

- Antigorite was deformed at constant stress to low strain
- Slip along basal planes and kinks allow plastic deformation
- Low temperature plasticity creep laws describe deformation rheology well

Abstract

A redesigned Griggs-type assembly and apparatus was used to deform antigorite under constant stress creep conditions at low temperature, low strain rate, and high pressure (1 GPa). Antigorite was deformed at constant temperatures between 75°C and 550°C, acquiring 8-12 rheology results per temperature. The microstructure of samples recovered after deformation highlights the importance of kinks to antigorite plasticity. Rheology data is optimally fit with a barrier-controlled plasticity law whose mechanisms agree physically with a kink-limited glide/slip deformation mechanism. When applied to natural settings, the extrapolated viscosity agrees well with predictions from subduction models.

2.1 Introduction

Subduction zones are among the most seismically active areas on earth. The wide spectrum of brittle and ductile behavior in the nearby mantle and downgoing slab control seismic coupling, deep fluid transport, and mantle convection. The interplay between rheology and metamorphic reactions is key to understanding tectonic dynamics and evolution at depth. To explain a range of observations at subduction zones (e.g., heat flow, location of volcanic front, slab seismicity, seismic structure of the mantle wedge), thermal models require slab decoupling down to a depth of approximately 80 km (e.g. Wada et al., 2008; Syracuse et al., 2010). Owing to its relative weakness compared to other lithospheric minerals, the presence of serpentine along the interface has been called on to promote this decoupling (e.g. Wada and Wang, 2009). In altered oceanic lithosphere and mantle wedge, antigorite is the stable serpentine polytype at these high pressure/high temperature conditions (Wunder and Schreyer, 1997; Schwartz et al., 2013).

The rheology of antigorite at high pressure has been investigated in a wide range of experimental studies (e.g. Hilairet et al., 2007; Auzende et al., 2015; Proctor and Hirth, 2016; Hirauchi et al., 2020). Flow laws constrained by strain rate stepping experiments from these studies show evidence for both power-law creep behavior (stress to n, with $n = 3$) and/or greater stress-dependence consistent with low-temperature plasticity or semi-brittle flow ($n > 20$). Such large variation in estimated stress-dependence leads to large uncertainties when extrapolating flow laws to the relevant geologic conditions. The relative importance of these mechanisms can be distinguished by conducting low strain rate creep tests at high pressure over a range of temperatures. Creep tests are advantageous because nominal steady state behavior can be achieved at low strain, allowing quantification of flow laws over a wider range of strain rates (almost all previously published data were collected at strain rates greater than 10^{-6} $1/s$).

We conducted creep tests on solid cores of mesh-textured antigorite at constant differential stress. To improve the resolution of both stress and strain rate we redesigned the dynamic seals, sample assembly, and mechanical control of a Griggs-type deformation apparatus for the temperature conditions where antigorite is stable. The microstructure preserved after deformation illustrates the importance of kinking and basal slip, rather than a solely dislocation glide deformation mechanism in serpentinite bodies (c.f. Auzende et al., 2015; Amiguet et al., 2014).

2.2 Materials, Cell Designs, Methods, and Data Analysis

2.2.1 Materials and Sample Preparation

Antigorite samples were cored from a serpentinite collected from the Nagasaki metamorphic belt in Japan; this material (which was also used in the studies of Proctor and Hirth (2015) and Okazaki and Hirth (2016)) is predominantly antigorite (98%) with minor diopside, spinel and magnetite (figure 2.7).

2.2.2 Sample Assembly

Samples were jacketed in thin copper or silver sleeves and deformed at 1 GPa confining pressure in one of three types of modified Griggs-type deformation assemblies, depending on the experimental temperature (Figure 2.1). For experiments at T=75°C, a weak Bi-Sn-Pb eutectic alloy was cast into a tube filling the space between samples and the pressure vessel walls (Figure 2.1c). When the entire

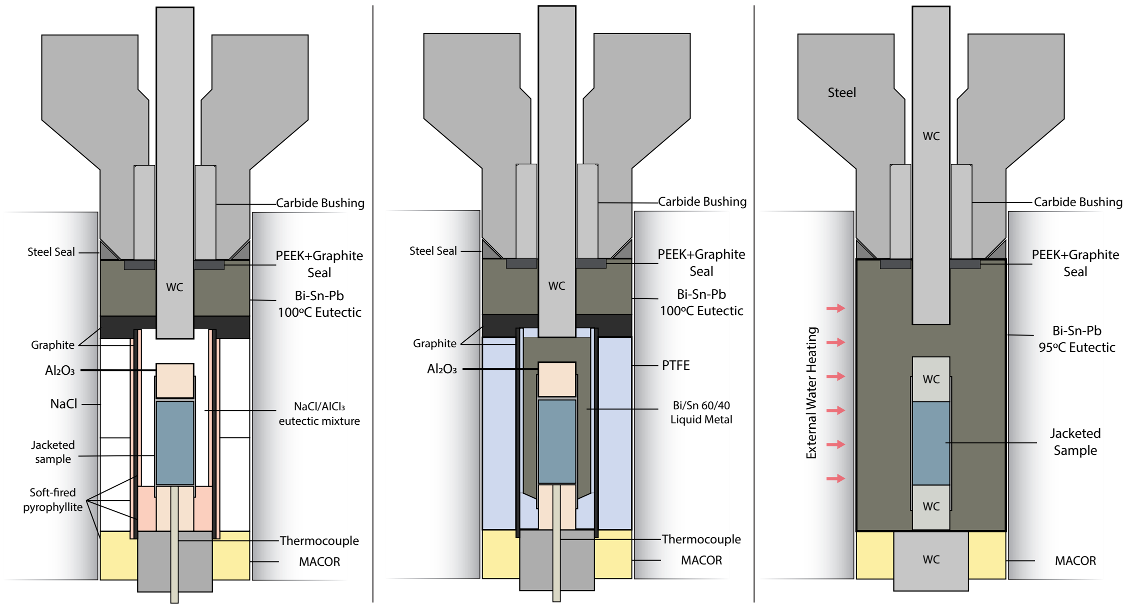

Figure 2.1: Sample assemblies used in this work. From left to right: High temperature partially molten salt assembly, teflon lined liquid metal assembly, low melt eutectic assembly (externally heated).

pressure vessel is heated above 70°C by flowing hot water through the standard cooling rings, the alloy becomes very weak and presents low resistance to sample expansion and piston advancement (further details are provided in the supplemental information). For T=200°C, a modified molten salt assembly was fabricated with molten Bi-Sn alloy replacing salt, and machined teflon replacing pyrophyllite (Figure 2.1b). For T>400°C, a eutectic partial melt salt (0.15AlCl3-0.85NaCl mol) was used in a molten salt assembly (Figure 2.1a).

The nearly fluid nature of these confining media necessitated the use of central axial thermocouples. Thermal modeling (see supplement) and previous studies (Kirby and Kronenberg, 1984) indicate that the axial thermocouple measures a slightly colder area of the sample column, representing a more reliable, but also lower bound on the sample temperature. In addition, moving the thermocouple out of the 100°C/mm gradient between the sample and furnace wall improved reliability of temperature determination.

Low apparatus friction is critical for characterizing samples with large stress sensitivity. To decrease friction, we replaced the typical beveled mitre-ring seal used in Griggs-type apparatuses with a tight-tolerance polished carbide bushing and Graphite-filled PEEK O-ring/washer (Figure 2.1). This design limits extrusion of seal material and promotes excellent piston alignment. We tested and calibrated the new design by conducting tests on brass using paraffin wax as a confining medium (Figure 2.16). With these improvements, both the magnitude and rate-dependence of cell friction was reduced by approximately a factor of five.

2.2.3 Stress Stepping Methods and Calibration

In all creep experiments on antigorite cores, the deformation piston was first advanced until it "hit" the sample and loaded to starting stress. The sample was then allowed to creep at constant load for 2-24 hours (whose data was not used). For each subsequent load step, strain rate was monitored and allowed to stabilize after reaching target load (see supplement text 2.6.2 for details). A list of experiments is included in table 2.1. To test the performance of the new assemblies, we also conducted stress stepping creep tests on Westerly granite at 200 MPa and 70°C in a low temperature assembly and compared the results to published data acquired in a gas-confining medium apparatus (Brantut et al., 2012). Our data compare favorably and show that we can accurately measure strain rate down to at least $5 * 10^{-8}$/s. For this calibration test, we recorded acoustic emissions, and observed that event frequency increased proportional to strain rate with 500 collected events (Figure 1.4). Post-processing of strain data reveals that Antigorite may continuously harden with increasing strain. The hardening is discussed briefly later in microstructural context, and more thoroughly in text 2.6.2.

2.2.4 Acoustic Data

While we did collect acoustic data during antigorite creep, emissions were only observed during pressurization. This result is consistent with the results of previous studies on deformation of antigorite (Escartin et al., 1997; Okazaki and Hirth, 2016; Gasc et al., 2017; Ferrand et al., 2017)

Table 2.1: Experiments

Experiment	Sample	Temperature (°C)	Pressure (MPa)	Confining Media	Strain
W2394-75	Westerly Granite	75	200	95C Alloy	0.04
W2424-550	Antigorite	550	1000	NaCl-AlCl3	0.02
W2439-400	Antigorite	400	1000	NaCl-AlCl3	0.04
W2441-75	Antigorite	75	1000	95C Alloy	0.05
W2447-200	Antigorite	200	1000	60:40 Bi:Sn	0.04
W2526-480	Antigorite	480	1000	NaCl-AlCl3	0.01
W2521-75	Antigorite	75	1000	Hydraulic Oil	0.03
W2520-520	Antigorite	520	1000	NaCl-AlCl3	0.02

2.3 Results

2.3.1 Mechanical Results

Mechanical data were collected at each temperature by varying applied stress and observing strain rate stabilize over time. When high strain rate points ($> 10-6$ 1/s)from a single temperature are plotted as the log of strain rate against the log of stress, they display a consistent slope (stress exponent "n"), which varies with temperature between 5 and 21. Data at the highest temperatures also show decrease in n at the lowest strain rate. Comprehensive fitting to a low temperature plasticity creep law is plotted in figure 2.2b and is discussed in section 2.4.1.

2.3.2 Microstructure

Antigorite is known to deform by nominally non-dilatant brittle deformation mechanisms at confining pressures above 50 MPa (Escartin et al., 1997; David et al., 2018). We collected acoustic emission data during the antigorite creep experiments, and as would be expected emissions were only observed during pressurization/depressurization (furnace/pyrophyllite cracking). This is in stark contrast to westerly granite experiments where we observe hundreds of emissions during creep due to crack opening and propagation. In addition, recent studies of antigorite's shear velocity evolution during deformation (David et al., 2018) confirm its non-dilatant nature and implies that opening of shear cracks and voids in solid samples happens after depressurization, so we consider recovered microstructure with that in mind.

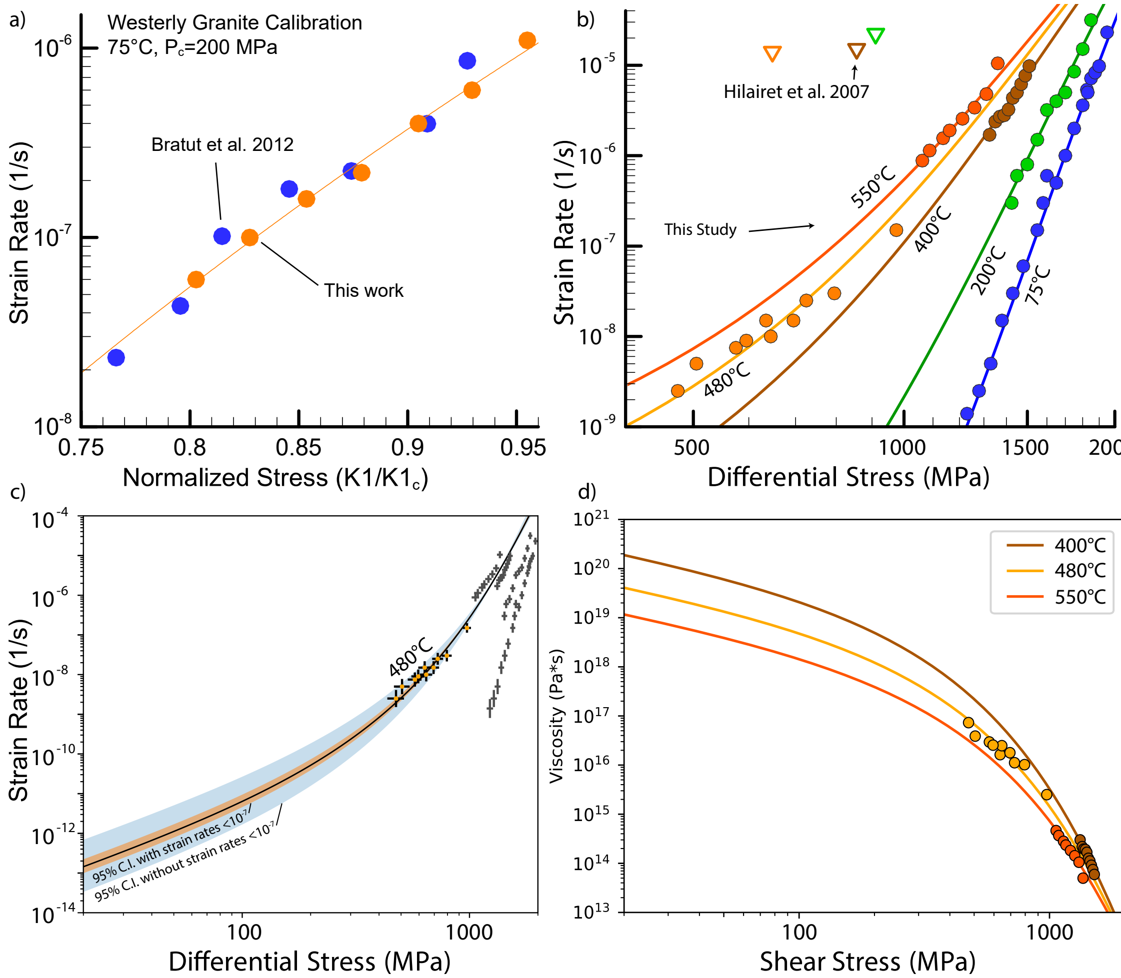

Figure 2.2: a) Comparison of normalized stress in this work to data of Brantut et al. (2012). b) Final strain rate plotted against applied differential stress (this study, circles). Curves are low temperature plasticity creep fits for each temperature. Data of Hilairet et al. (2007) are included as open inverted triangles for reference. c) Plot of best fits on all data, extrapolated with confidence intervals at 480 °C. Error bars on data points are plotted as lines. Data collected at 480 °C are highlighted arange, while all other points are plotted in grey. The best fit is a constant athermal flow stress (τ_0) of 2.42 ± 0.04 GPa, inner exponent p of 1, outer exponent q of 1.18 ± 0.04, an average activation enthalpy of 86 ± 1.4 kJ/mol, and a pre-exponential constant A of $\exp(-.62 \pm 0.1)$ 1/s. d) Plots of extrapolated viscosity vs. stress to subduction conditions.

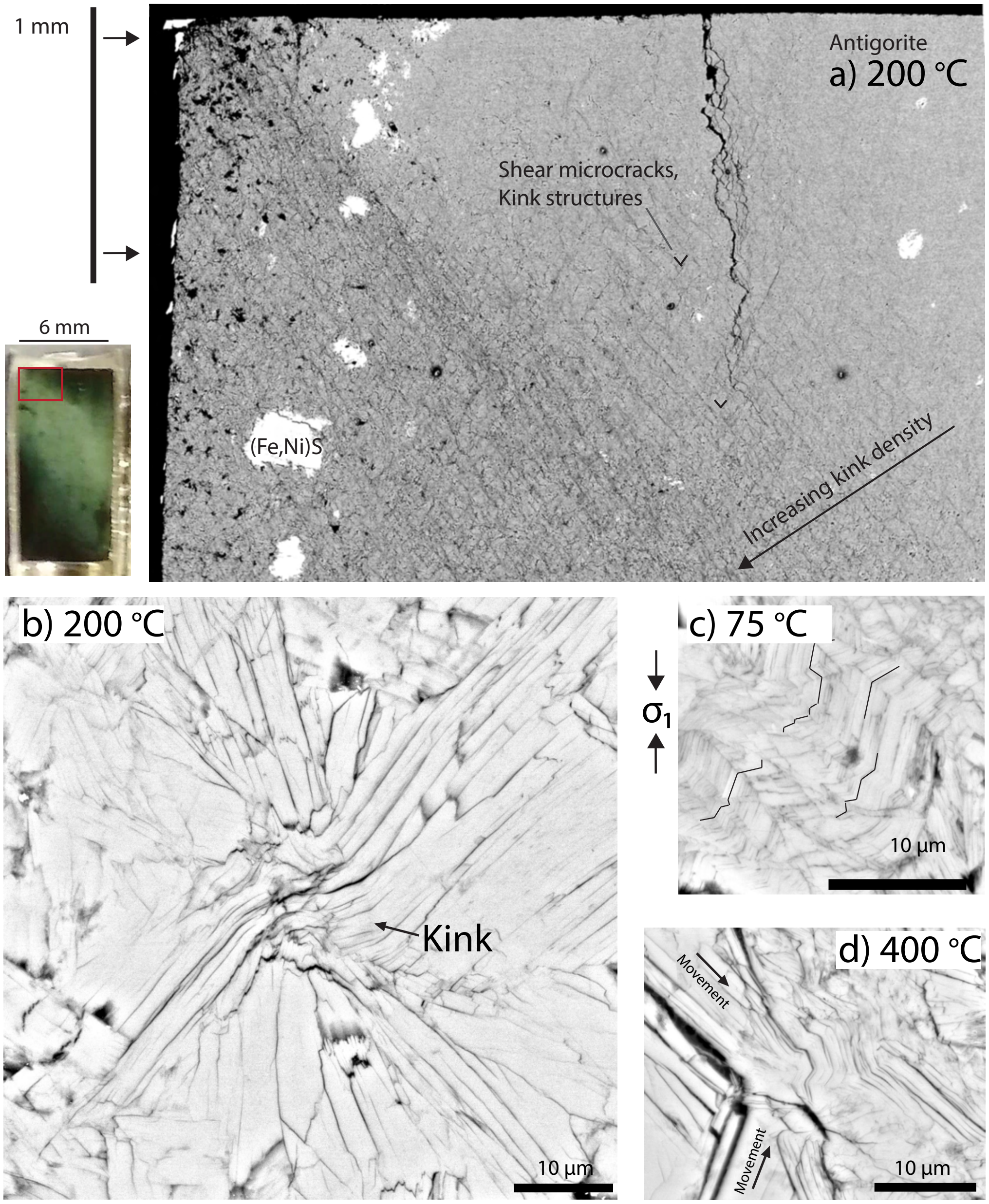

Figure 2.3: a) Image showing both macroscopic color image of damage (light color), and backscatter SEM image of the 200°C creep sample. The visible structures in SEM are X-shaped structures of opposing antigorite foliation. The poor orientation leads to kinking at the intersection of opposing grains and delamination opening upon decompression around the kinked structures. b) Backscatter SEM image of x-shaped structures in the 200 °C creep sample. Poor orientation of the pictured grains forces kinking at the intersection, and eventual tearing when easy kinking is exhausted. C-axis (along sheet) deformation is required for this structure to form. Delamination cracks open after decompression due to residual stress. c) SEM Image of low temperature antigorite deformation microstructures. Tight kinks, with angles 2-3x higher than elevated temperatures are highlighted by black lines following the sheet basal planes. d) SEM Image of structures in the sample deformed at 400°C. Arrows denote movement of poorly oriented grains along a cracked slip surface. Stress is concentrated at the intersection of the grains, resulting in four tight kinks. Note that kink angle and delamination decrease rapidly with distance from the intersection in contrast to lower temperature microstructure. Differential stress is vertical in all images.

The original microstructure of cored samples shows a generally isotropic mesh texture defined by antigorite grains oriented dominantly around 45 degrees to the axial compression direction (supplement Figure 2.6). There is no macroscopic foliation, and the grains appear to be ”cross-stitched”. The mesh texture is not visible in backscattered electron images of undeformed cores. However, it becomes visible after deformation as shear cracks open during decompression. Basal slip along the antigorite grains leads to contact interactions between grains in the opposing sheets of the mesh texture, whose recoverable microstructure varies with temperature. Sample scale photos of the deformed samples are presented in Figure 2.7.

Cores deformed at 75°C have deformation localized into a 0.11 mm wide, banded structure oriented 35 degrees from the axial compression direction. Within the localized zone , we observed $< 200\mu m$ long fractures and a high density of relatively tight kinks (Figure 2.3b); surprisingly, there is little other evidence for comminution/damage in the localized zone. We define kink angle as deviation from an unkinked plane (180 degrees less/minus the inner angle between visible cleavage planes) so that slight bending corresponds to a small kink angle. The average kink angle at 75°C is 54° (29 measurements, minimum 40°, maximum 68°). This is approximately the period doubling angle observed in polygonal serpentinite samples (spiral/tube sheet growth with kinks) (Grobéty, 2003).

The core deformed at 200°C also displays deformation localized at 35 degrees to axial compression, but the “fault zone” is wider (1-2 mm width, Figure 2.3a). No deformation-induced fractures longer than 100 µm are present. Instead, deformation is accommodated by basal shear and kinking. Kinks appear at the intersection of well- and poorly-oriented grains whose sheets have clearly slipped along basal cleavage during deformation, forming X-shaped features (Figure 2.3b). When the bend of kink plane is small (see Figure 2.3b), the sheets remain kinked and intact along their length. In cases where offset if larger, they tear at the kink apex. Average kink angle in these X-shaped structures is 23° (9 measurements, minimum 15°, maximum 33°), approximately half the angle observed at 75°C.

At 400°C the deformation becomes much more distributed. Kinks and microcracks are evenly distributed in the deformed part of the sample. A lack of strain localization in core samples deformed to low strain at 400°C is consistent with previous work (Chernak and Hirth, 2010). The same X-shaped structures are also present in the most deformed parts of the sample, but they are less densely spaced than observed at lower temperature – and accordingly there are fewer kinks in the sample deformed at 400°C. The kink angles are quite variable and also vary as a function of distance from the stress concentrating feature (Figure 2.3c). The average kink angle less than 10 µm from the feature is 45 degrees, while the kink angles 20 µm away are 10-20°. This observation suggests that the kink bands grow outward with increasing deformation at the stress-concentrating feature.

Samples deformed at 550°C also have the same X-shaped structures, and distributed deformation similar to the 400°C sample. However, we did not observe any kinks. Some slight bending of grains is observed, but only at very small scales ($< 1\mu m$). Where these small bends in the grains appear (supplement Figure 2.8), they do not have a clear apex that lower temperate samples possess. This observation suggests thermal activation of some reaction/recovery mechanism "healing" the kinks and basal slip that is occurring.

2.4 Discussion

2.4.1 Low Temperature Plasticity

The creep data in figure 2.2 define a continuous stress dependence at each temperature. The systematic variation among temperatures is well described by a constitutive model used for obstacle-controlled glide of dislocations that must "cut through" obstacles like precipitate particles in hardened metals. We suspect that antigorite deformation fits this deformation rate equation so well because interactions of grains with basal slip planes in optimal orientation (high resolved shear stress on basal planes) impinging on poorly oriented grains. Additionally, low temperature plastic deformation is often accompanied by hardening, or build up of an internal stress (e.g. Hansen et al., 2019). Post-processing of data in this study reveals that unlike our westerly granite tests, antigorite strain rate continues to decrease slowly with increasing strain. The hardening suggests interaction of kinks or exhaustion of easy kinking, but does not appear to be significant enough to affect our flow law determination (see supplement 2.6.3). More study is needed of slip on planar antigorite (if it can be grown or fabricated) at variable pressure to constrain the magnitude of individual contributions of basal slip and kinking/rotation to flow and hardening of serpentinite.

2.4.2 Flow Law

Reduction of the stress sensitivity/stress exponent with increasing temperature is consistent with exponential low temperature plasticity or "barrier controlled" creep laws where the "barrier height" is lowered by thermal activation. Microstructural observations suggest the barrier mechanism involves basal slip and kinking of the antigorite grains. That law has the form (Frost and Ashby, 1982):

$$\dot{\epsilon} = A \left(\frac{\sigma}{\mu}\right)^2 \exp\left(\frac{-\Delta G}{RT}\left(1 - \left(\frac{\sigma}{\tau_0}\right)^p\right)^q\right) \tag{2.1}$$

Fitting data to the law is very sensitive to changes in the exponents. Typically data do not extend to low enough strains rates to constrain p and q (e.g. Evans and Goetze, 1979) and these parameters are often assumed to both have values of 1 as suggested by theory (Frost and Ashby, 1982). Our data at strain rates of 10^{-8} and 10^{-9} 1/s do constrain the exponents (see supplement figure 2.15) so we were able to invert for parameters on all data from 75°C to 550°C. The best fit using all collected data gives a constant athermal flow stress (τ_0) of 2.42 ± 0.04 GPa, an inner exponent p of 1, an outer exponent q of 1.18 ± 0.04, an average activation enthalpy of 86 ± 1.4 kJ/mol, and a pre-exponential constant A of $\exp(-.62 \pm 0.1)$ 1/s. Additionally some pressure dependence of antigorite strength exists, but it is modest so it is not included here (Proctor and Hirth, 2016).

2.4.3 Deformation Mechanisms in Undamaged Antigorite

The most critical aspects of the current work are constant stress testing and using dense antigorite cores. Typical constant strain rate experiments capture strength of an evolving microstructure that is complicated by antigorite's anisotropic sheet structure. Powdered material is not effectively densified and sintered below dehydration temperatures (Burdette and Hirth, 2020) and deformation includes compaction events even at 1 GPa confining pressure. Constant stress testing of solid cores captures rheology at low strain and can be used to examine mechanical response at a microstructural "snapshot". As a result, we are testing the rheological behavior of the undamaged rock, rather than the response of a "cold pressed gouge" that experienced sheet tearing and comminution which occur after easy kinking is exhausted. Here we show in more detail how the kinking mechanism fits into broader study of antigorite deformation.

Some of the earliest serpentinite deformation work notes kinks in the experimental fault zone. Raleigh and Paterson (1965) write "Study of thin sections shows that in the ductile specimens serpentinite grains throughout the deformed zone have become bent or kinked. In the transitional specimens, the faults consist of narrow zones of strongly reoriented serpentinite grains; some grains lying outside the faults appear to have been plastically deformed, but the majority of these are adjacent to the fault zones. In brittle specimens, there is no evidence of plastic deformation outside of a very narrow band of highly oriented serpentinite present in places along the fault." Their transition microstructures were produced by increasing pressure at room temperature, instead of increasing temperature at constant pressure, but these microstructural changes are similar to the transitions we observe with increasing temperature at higher confining pressure.

More recent work highlights activity of a key mechanism for the formation of kinks: slip along the basal cleavage plane. Escartin et al. (1997) measured volumetric strain in foliated antigorite and found that deformation was nominally non-dilatant (cracks are not opening, but rather sliding during deformation). In addition, their microstructural characterization shows cracks form exclusively along the (001) plane of the antigorite sheets, further supporting the activity of basal sliding. Non-dilatant shear deformation is also consistent with the lack of acoustic emissions due to the microcracking and clear formation of shear cracks we observe in this study. David et al. (2018) confirm the non-dilatant behavior in a more recent study with seismic velocity, and further show some of the plastic deformation behavior of the cores is reversible, as would be expected for a material deforming by low temperature plasticity mechanisms with a strain-hardened back stress.

In an expanded study (David et al., 2020), which included experiments at confining pressures up to 1 GPa, they concluded a similar shear-crack mechanism can explain the reversible deformation and pressure dependence to 1 GPa.

The observation of non-dilatant shear deformation suggests the possibility of basal dislocations, but they have not been observed in indentation or push-pull TEM studies. Hansen et al. (2020) nanoindent antigorite, but only observe a “paucity” of crystal plastic deformation up to 6 GPa ”differential” stress. Similarly, in TEM experiments of antigorite grains (push-pull style tension), Idrissi et al. (2020) observe deforming antigorite grains in real time up to 800 MPa tension, but do not observe moving dislocations that other materials display (e.g. olivine of Idrissi et al., 2016), and instead observe grain boundary sliding.

If antigorite deforms dominantly by grain boundary/basal fracture slip, then it needs rotation mechanisms to satisfy the volume-preserving Von Mises criterion. This constraint can be satisfied by the kinks observed in Figure 2.3. Our nominally isotropic antigorite starting material does not have the continuous “bladed band” structure present in many other serpentinites (Escartin et al., 1997), and instead has many sets of nearly perpendicular antigorite grains, which we call “cross-stitched”. This cross-stitched microstructure is possibly the strongest texture because basal slip is regularly impeded by grains perpendicular to the slip direction. As Figure 2.3 shows, the grain interactions are accommodated by kinking and tearing of the perpendicular grains.

2.4.4 Comparison to Other Materials

Some other materials have sheet structures with similarly high creep strength and reversible grain boundary deformation. Studies of their deformation show a strong dependence of behavior on grain size and have clearly kinked structures after indentation and deformation. At very high temperatures (1150°C) TiSiC undergoes a transition in material behavior to a diffusion creep process with a power law exponent of 2 ± 0.5 (Barsoum and Radovic, 2011). We tested Antigorite at very low strain rates ($10^{-9} 1/s$) as close to the dehydration temperature as possible (480-520°C). While we do observe a change in power law exponent, mechanical data fits the low temperature plasticity law extrapolated from our other creep data well.

2.4.5 Temperature Sensitivity of Kinking

While obstacle-controlled glide offers an explanation for the temperature sensitivity of strain rate, it does not fully explain a key feature of the microstructure, namely, the reduced prevalence of kinks and smaller kink angles at higher temperature. Our experiments at 75°C display high kink density preserved in the sample with very sharp apexes (Figure 2.3). In contrast, at 400°C we observe lower density, ”wavy” kinks. Examination of samples deformed to higher strain in other studies show a transition to strain localization on sharp faults with slickensides above 550°C (Chernak and Hirth, 2010). The common feature in this works’ temperature series is increased orientation and rotation of the antigorite grains at high temperature into the shear plane that does not tear grains at high strain. The mechanism of recovery or recrystallization that allows grain rotation by either healing or recrystallizing kinks is still unknown but will be important to understand in future studies.

2.4.6 Implications of Temperature Sensitive Grain Rotation

The kink rotation mechanism may also explain some seismicity. If a shear fault forms and causes alignment around its core, shear stress could drop precipitously once stress concentration on very poorly aligned grains reaches the level required to tear them, leading to rupture on a planar surface with only a few strong patches which fail together. In addition, rotating grains such that their basal planes are parallel to fault zones would lead to localized low permeability, strongly enhancing the effectiveness of shear heating and dehydration weakening. These mechanisms could contribute to recently noted acoustic emissions of antigorite-olivine mixtures (Ferrand et al., 2017).

2.4.7 Geodynamic Implications of Flow Law Parameter Results

The work of Wada et al. (2008) on subducting slab modeling suggests strength of a 100m thick layer of weak material at the slab surface would require viscosity between 10^{19} and $10^{18} Pa \cdot s$ to match heat flow measurements constraining mantle decoupling depths. At 400°C and shear stress of 50 MPa, our results predict a viscosity of $10^{19.5} Pa \cdot s$ and at 600°C they predict viscosity of $10^{18.0} Pa \cdot s$ (deviatoric conversion after Wada et al. (2008), n=2 below 100 MPa). Extrapolation after conversion is presented in figure 2.2d. The difference between the flow law and heat flow inferred values is within experimental error, and could be accounted for with a slightly thicker 200-300m weak layer.

The rheology examined here is limited to low strain ($< 5\%$). Competition between the hypothesized temperature activated recovery (which requires long times) and hardening due to increasing kink density at high strain ($> 5\%$) could alter extrapolated viscosity.

2.5 Conclusions

In this study we redesigned a Griggs-type apparatus and assembly for constant stress creep testing of antigorite at low temperature, low strain rate, and high pressure. Antigorite was tested at temperatures between 75°C and 550°C, acquiring 8-12 rheology results per temperature. The microstructure of samples recovered after deformation highlights the importance of kinks to antigorite deformation. Deformation data suggests activity of barrier-controlled low temperature plasticity, further supporting the hypothesis that kink formation is the rate-limiting deformation mechanism. When extrapolated to subduction conditions, the data fit surprisingly well to model-based requirements for coupling along the subduction interface.

Acknowledgments

We thank Nicolas Bantut and Emmanuel David for helpful discussions. We would also like to thank Hannah Rabinowitz for encouragement and assistance upgrading the apparatus. In additions we thank Keishi Okazaki collected the antigorite used in this study.

2.6 Supporting Information

2.6.1 Mechanical Data Calculations

The Griggs apparatus has both external load and displacement sensors which need to be corrected to find load and displacement on the sample inside the pressure vessel. Differential stress is determined by subtracting a "hit point" stress (hydrostatic pressure+friction) from the externally measured load. Displacement is determined by subtracting displacement absorbed by the column in compression (Burdette and Hirth, 2020), and referenced relative to the "hit point".

$$x_{sample} = x_{LVDT2} - \frac{\sigma_{1,external}}{k_{lower/_{c}olumn}} \tag{2.2}$$

To calculate permanent/inelastic strain, elastic compression of the sample can also be removed:

$$k_{sample} = \frac{E}{l_{sample}} \tag{2.3}$$

$$x_{inelastic} = x_{LVDT2} - \frac{\sigma_{1,external}}{k_{lower\_column}} - \frac{\sigma_{differential,internal}}{k_{sample}} \tag{2.4}$$

Note that these equations assume sample elasticity is constant, and don't account for rate-dependent friction.

To calculate strain rates during post-processing, we used the first derivative of a first order Savitzky-Golay filter (moving line fit) over a moving time window chosen for each step. For strain rates above $10^{-6} 1/s$, the window could be as short as 100 seconds, while the lowest strain rates require a 10000 second time window. Strain rates chosen for flow law fits were the final point that was not influenced by a disturbance or loading to the next stress. Wherever strain rate is plotted as a continuous function of time (e.g. figure 2.9), a single window length was chosen over the whole plot to best display data.

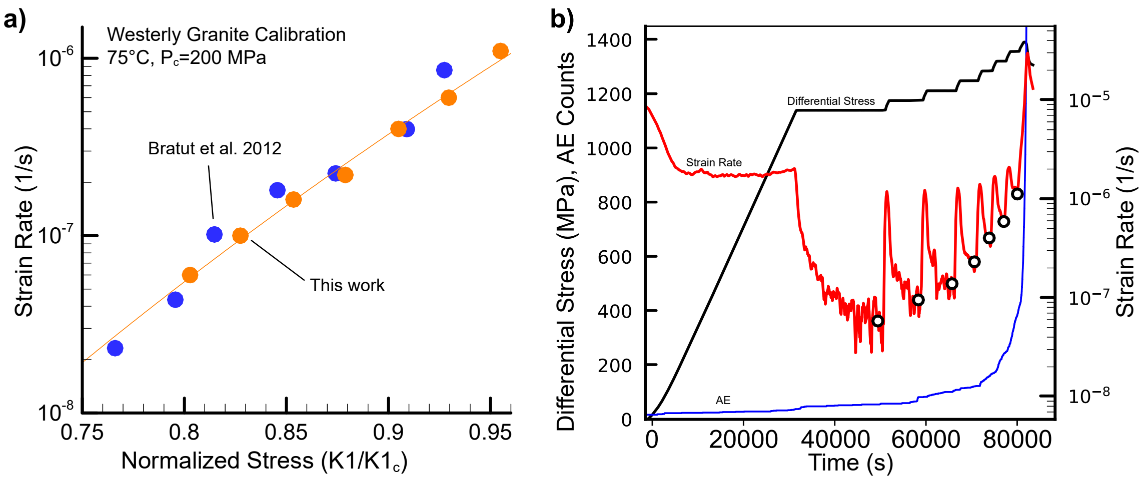

Figure 2.4: a) Comparison of normalized stress in this work to data of Brantut et al. (2012). b) Data recorded during the creep test on Westerly granite. Points denote measured strain rate after sample have settled to a constant rate. Acoustic emission (AE) data are counts/hits of events recorded during the experiment.

2.6.2 Hardening During Stress Steps

During individual stress steps samples harden over time (S2.10). Hardening is expected to some extent from other descriptions/results of brittle creep and high temperature creep tests where primary, secondary, and tertiary creep phases can be identified. For westerly granite calibration tests (S2.4), at each step samples reach constant strain rates after relatively small strains (0.2%). Post-processing of antigorite data shows that it may continue to harden over similar 0.2% strain steps (depicted in data for W2447-200 (S2.10)). This decay is not obvious in live displays of data because it requires more processing power to smooth and compute than our rig control PC has available.

The observed rate decay appears to be linear when plotted as either log(strain rate) vs. strain (2.12) and log(strain rate) vs. time (2.13). The strain rate decreases by approximately a factor of 2 over 0.2% strain as can be observed in the included strain-time plots for W2447-200 (2.10), and the decay during hydraulic oil confined experiment W2521-75 (2.12). (Data is FIR decimated by a factor of 100 to 0.1Hz for these plots).

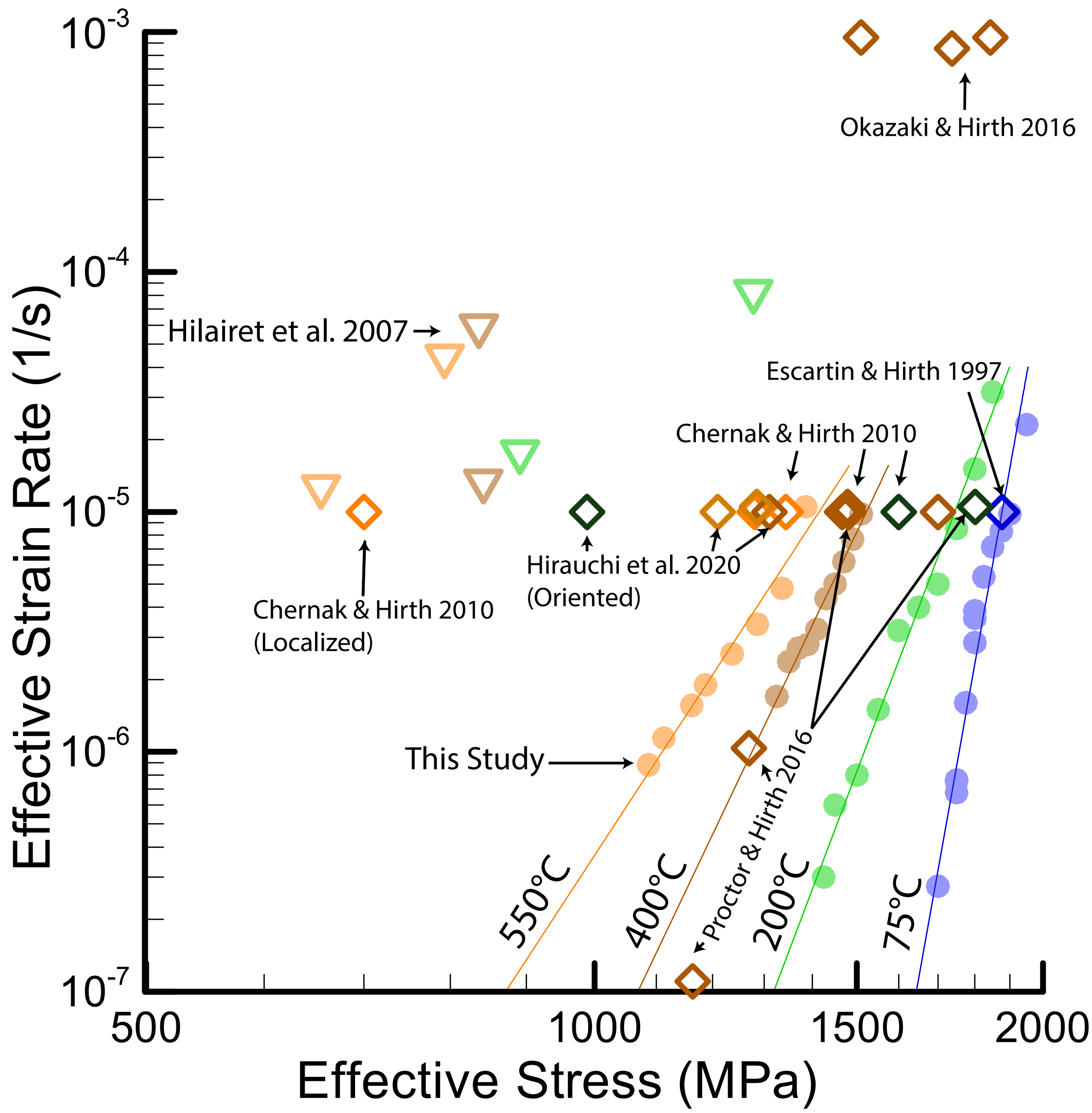

Figure 2.5: Compilation of other high pressure experimental antigorite deformation results plotted over results form the current study. Colors of points denotes temperature for all points. Both cores (Hirauchi et al., 2020; Chernak and Hirth, 2010; Escartin et al., 1997) and gouge (Chernak and Hirth, 2010; Proctor and Hirth, 2016; Okazaki and Hirth, 2016) are plotted.

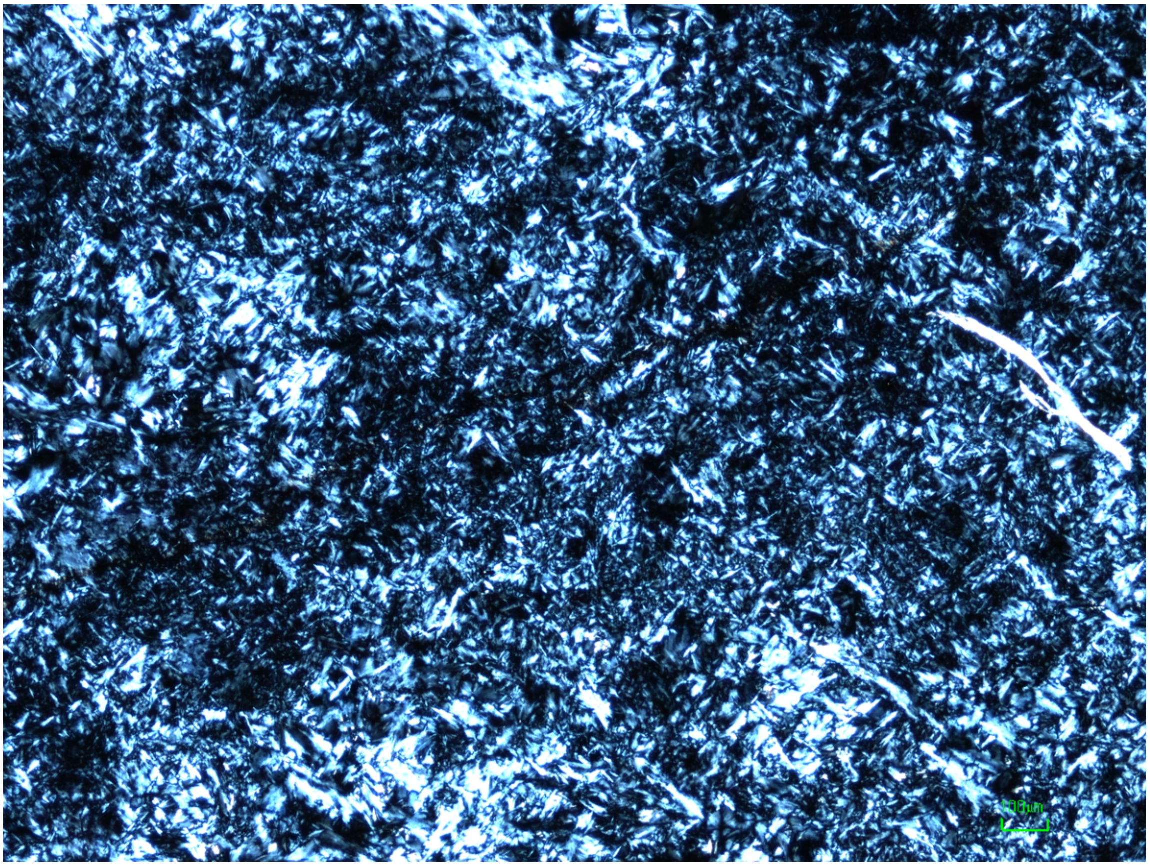

Figure 2.6: Thin section image (cross-polarized) of undeformed mesh texture. Compression of samples was in the vertical direction.

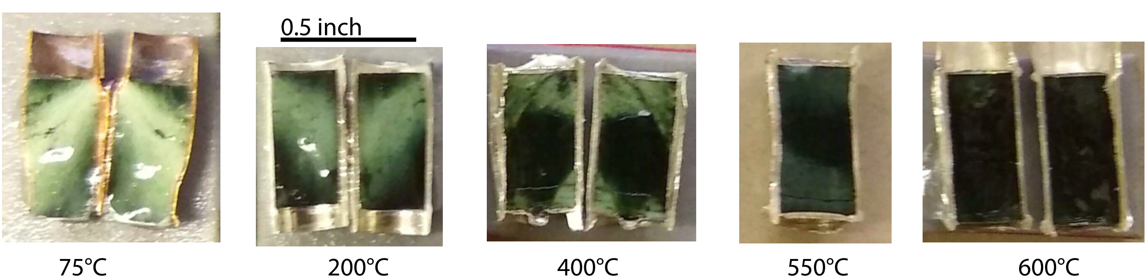

Figure 2.7: Images of antigorite core macrostructure. light/white portions of samples have shear microcracks.

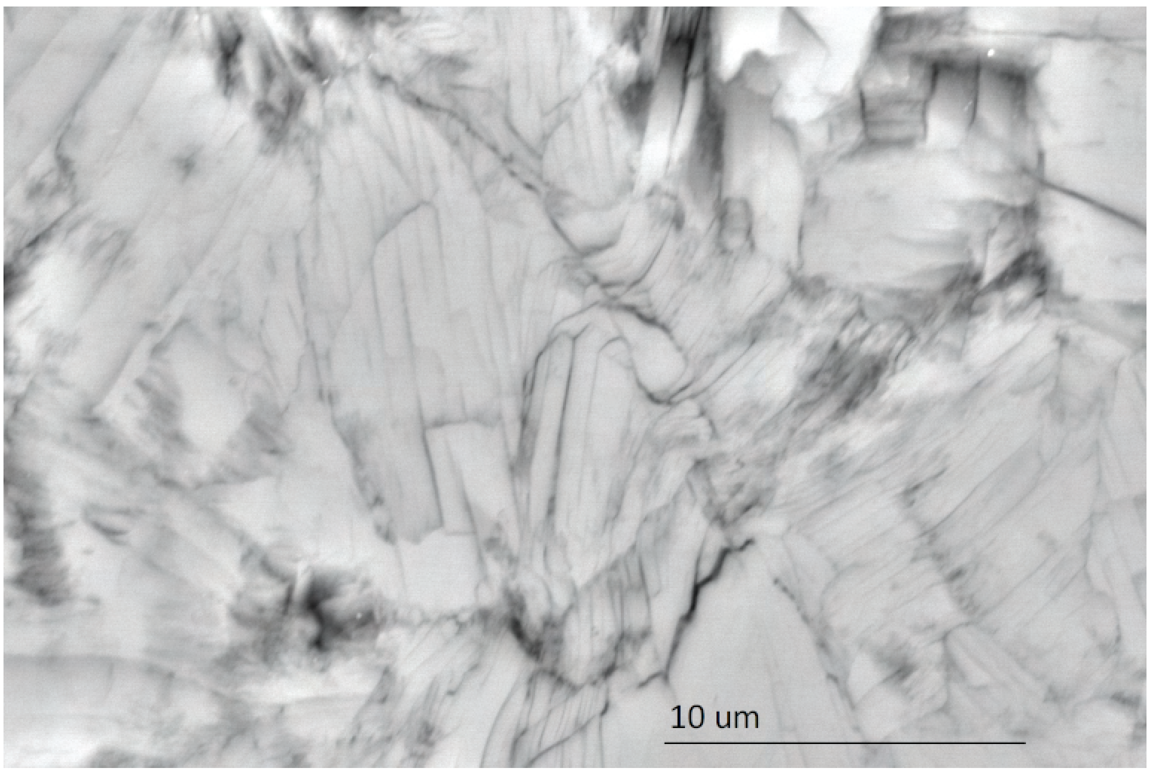

Figure 2.8: Gentle curvature of sheets recovered from 550°C sample.

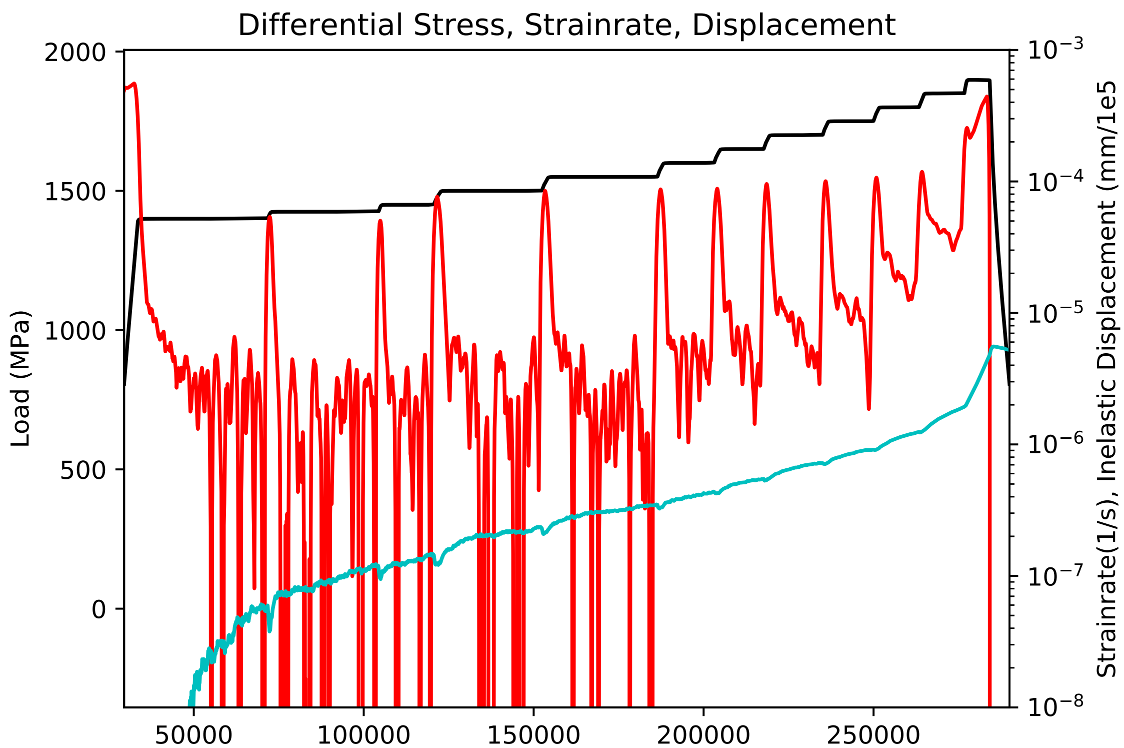

Figure 2.9: Experiment data from 200°C experiment. black->stress; red->strainrate; cyan->strain (log scale).

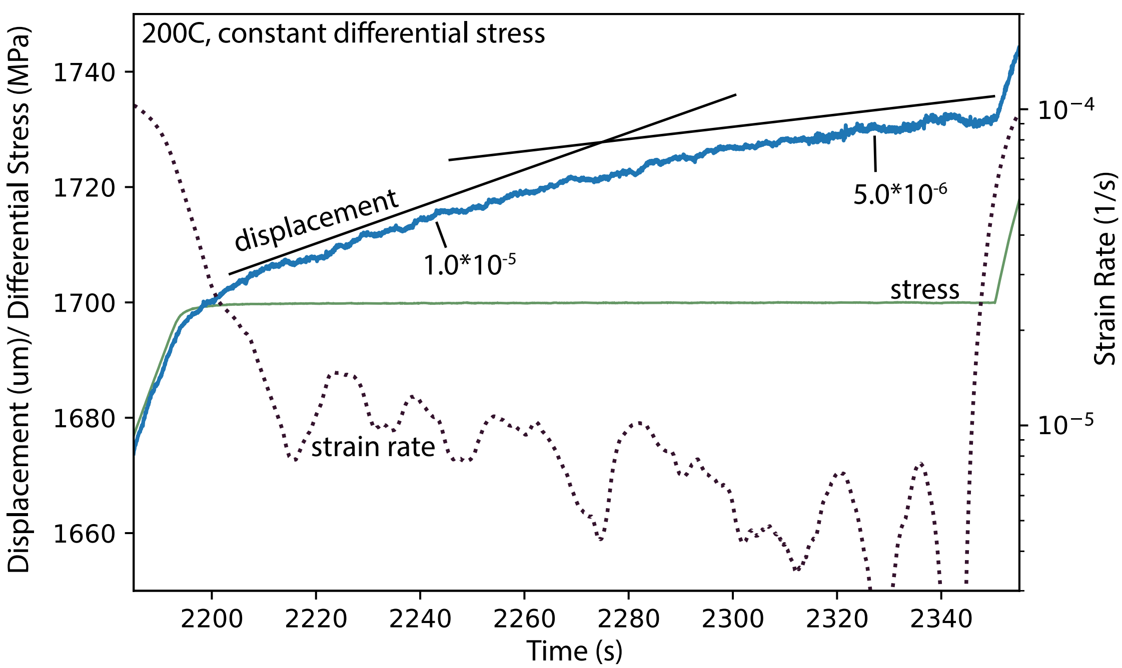

Figure 2.10: Load and Displacement plotted against time to show strain rate evolution during a stress step. Data is taken from the last portion of the curve. Rate changes by approximately a factor of 2.

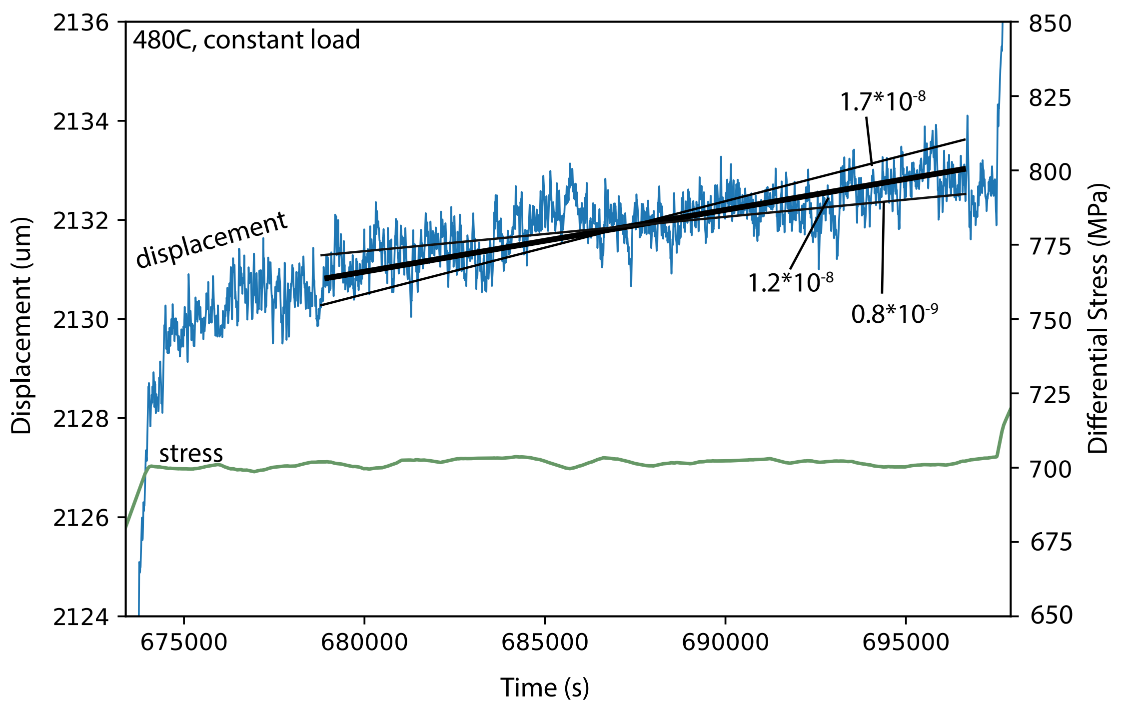

Figure 2.11: Load and Displacement plotted against time to show strain rate evolution during a stress step. For "low" stresses, the displacement resolution limits determination of strain rate

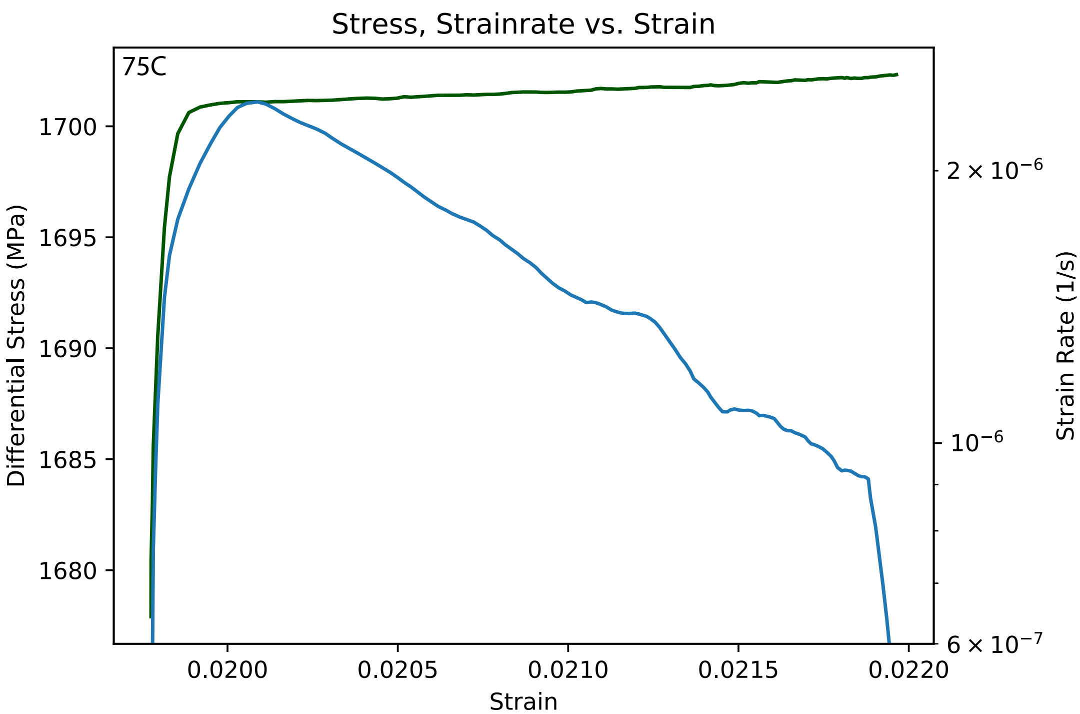

Figure 2.12: Hardening of antigorite at room temperature where rate change and stress are plotted against strain. Decay appears to be approximately log-linear.

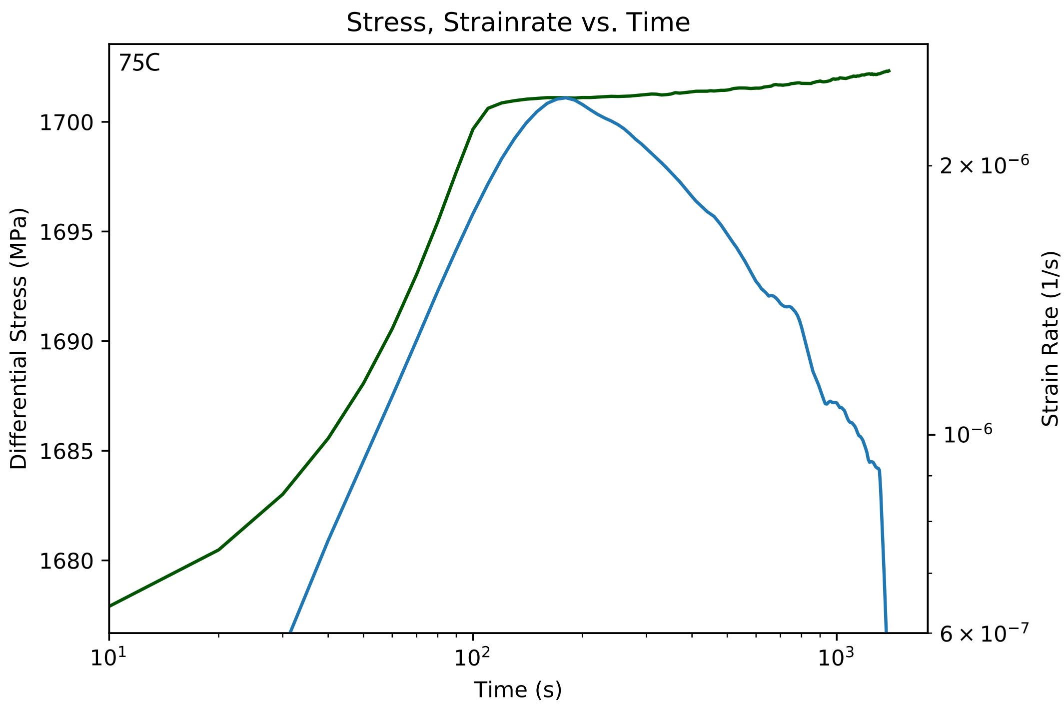

Figure 2.13: Hardening of antigorite at room temperature where rate change and stress are plotted against time.

2.6.3 Uncertainty introduced due to hardening

The ratio of initial/final strain seems to be similar at most stress steps. This makes ratio/increment (hardening slope) much larger at small strain. Hardening literature plots the change as $d\sigma/d\epsilon$ vs. σ (Kocks and Mecking, 2003). It's unclear if that's appropriate for materials with pressure-dependent strength.

To assess the potential uncertainty introduced into the flow law by choosing final instead of initial strain rates, we re-plotted the fit for initial strain rates. Because change is a similar factor of 2 for most steps, the fit exponent and athermal flow stresses don't change significantly while pre-exponential and activation energy change by 5%.

In addition, our creep data can be compared to other antigorite deformation studies at similar temperatures and pressures 2.5. Some of the comparable studies use antigorite gouge instead of cores, which is noted. Despite widely varying methodology, recorded stress/strainrate is similar to other studies, except where samples are highly aligned or deformation is highly localized.

2.6.4 Flow Law Fit Methodology

A low temperature plasticity flow law was fit to stress vs. log(strainrate) using a Markov-chain Monte-Carlo (MCMC-NUTS) optimizer due to the small local discontinuities in the fit. Results with errors are presented in Table 2.2 and distributions of the posterior are plotted in figure S2.14.

Table 2.2: Low temperature plasticity creep fit results

	Mean	Standard Deviation	hdi_2.5%	hdi_97.5%
lnA ln(1/s)	-0.624	0.118	-0.393	-0.859
Ea (J)	86283.744	1444.382	83395.443	89076.417
T_p (GPa)	2.416	0.044	2.330	2.502
q	1.177	0.048	1.081	1.268
$sigma_{obs}$	0.215	0.020	0.176	0.255

Low stress data have a larger influence on the extrapolated fit because they define the transition between stress and temperature activation dominated regions of the Peierls law. The start of this transition can be seen in the slight curvature of the fit around points at 480°C in figure

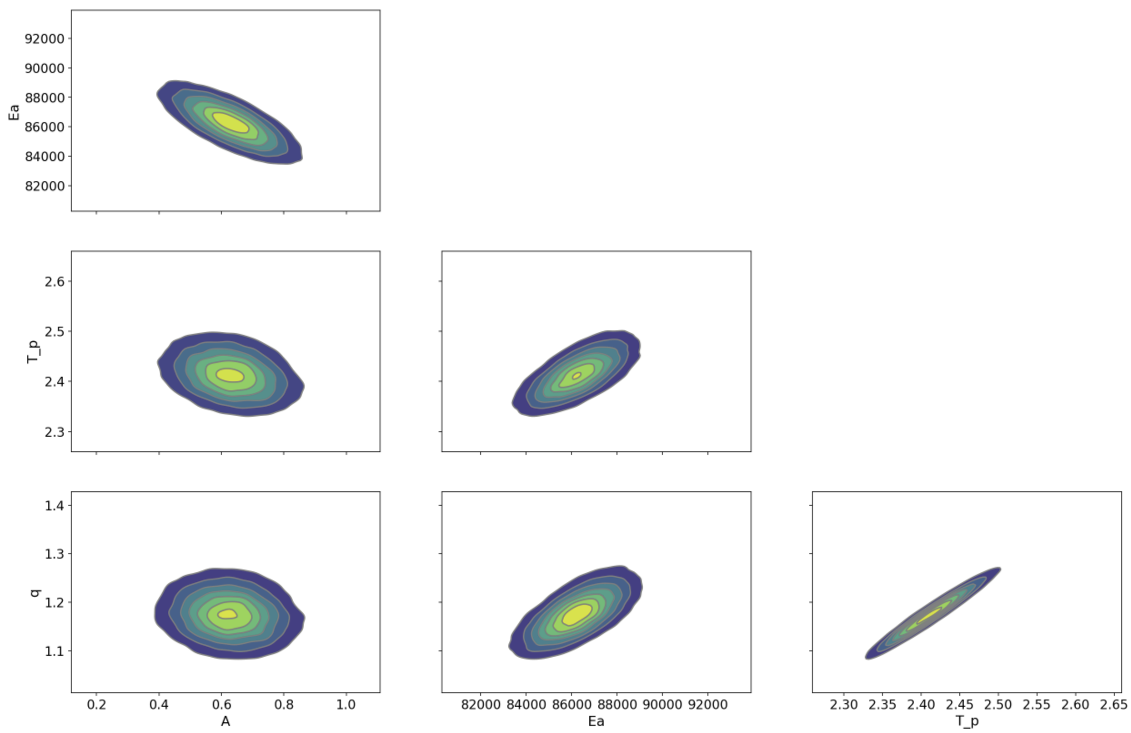

Figure 2.14: Posterior probability density functions in parameter space for the MCMC fit.

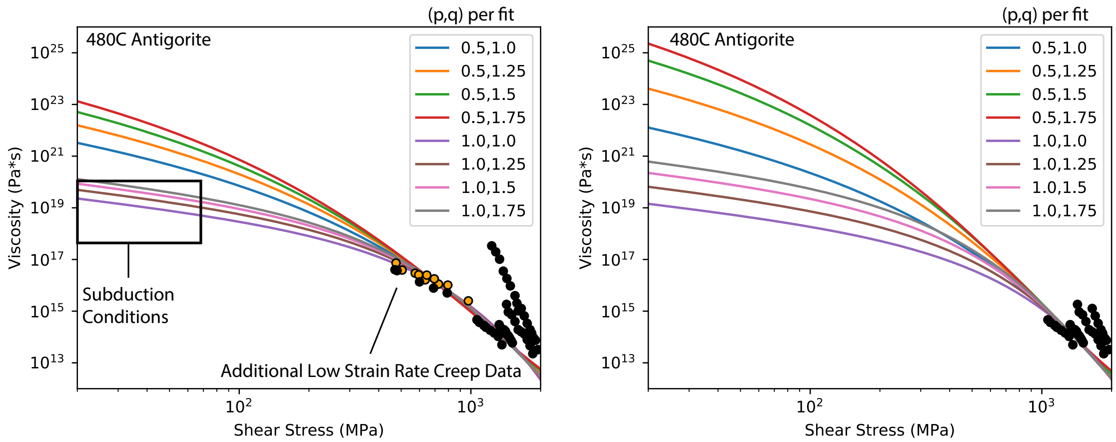

Figure 2.15: Comparison of fits for fixed exponent p,q combinations before and after slow strain rate data is added to the dataset (for illustration). Slow strain rate data has a very strong effect on extrapolated viscosity.

2.2. In the flow law, the region is defined by exponents p, q, and normalization factor τ_p. Changes in the curvature have a very large effect on extrapolated certainty of extrapolated viscosity. In this case feasible extrapolated viscosity decreases by several orders of magnitude when data at low stress is added to the fit (figure S2.15), and best fit confidence intervals shrink by an order of magnitude (figure 2.2).

2.6.5 Griggs Rig Friction/Accuracy Measurement

Several tests were completed to compare the new carbide bushing seal to the old mitre ring seal. We first deformed 360 grade brass rod, cut to simulate samples and confined by paraffin wax. The assembly was externally heated using hot water (same method as low temperature metal assembly), and repeatedly ”hit” at different temperatures. (Figure 2.16) We found that the squeezing force measured during “run-in”/”hit” roughly follows predictions for “squeeze flow” rheometry. When the viscosity of the squeezed fluid decreases (in this case by heating the wax), the force for a given piston separation decreases. There is also a hysteresis with piston direction that does not vary significantly with temperature or distance between the sample and advancing piston. This appears to be primarily bearing friction applied by the packing ring. When we change to the carbide bushing, the size of the hysteresis loop decreases by a factor of 5x. Finally, rate dependence was explored with steps in the nearly fluid confining wax. Rate changes have a smaller effect with the carbide bushing (2 MPa/10x strain rate), and do not have the small displacement dependent stress peaks the older mitre ring induces.

To further test the ability to match the results of high temperature assemblies to room temperature assemblies, we loaded fused silica at 700°C in a standard, mitre-ring assembly and in a hydraulically confined assembly at low pressure (Figure 2.17). The results compare well, with the elastic modulus of the fused silica at high temperature matching the elastic modulus at low temperature. This indicates that we can compare all assemblies used in this study to each other and older results at similar conditions.

Table 2.3: Creep data

Initial Strainrate (1/s)	Final Strainrate (1/s)	Initial Strain	Final Strain	Stress (MPa)	T (°C)	Experiment
3.20E-06	2.85E-06	0.0001	0.0015	1800	75	W2441
7.80E-07	7.63E-07	0.0015	0.0022	1750	75	W2441
3.90E-06	3.87E-06	0.0022	0.0031	1800	75	W2441
7.53E-07	7.53E-07	0.0031	0.00345	1750	75	W2441
4.00E-07	2.75E-07	0.00345	0.0036	1700	75	W2441
9.00E-07	6.75E-07	0.0036	0.004	1750	75	W2441
4.00E-06	1.60E-06	0.004	0.0064	1775	75	W2441
6.80E-06	3.60E-06	0.0064	0.01	1800	75	W2441
9.40E-06	5.36E-06	0.01	0.016	1825	75	W2441
1.30E-05	7.15E-06	0.016	0.024	1850	75	W2441
1.42E-05	8.30E-06	0.024	0.034	1875	75	W2441
1.60E-05	9.80E-06	0.034	0.05	1900	75	W2441
3.00E-05	2.31E-05	0.05	0.07	1950	75	W2441

Continuation of Table 2.3

8.00E-07	3.00E-07	0.00042	0.00087	1425	200	W2447
1.00E-06	6.00E-07	0.00087	0.0011	1450	200	W2447
1.00E-06	8.00E-07	0.0011	0.00178	1500	200	W2447
2.20E-06	1.50E-06	0.00178	0.00268	1550	200	W2447
5.00E-06	3.20E-06	0.00268	0.00338	1600	200	W2447
7.00E-06	4.00E-06	0.00338	0.00423	1650	200	W2447
1.10E-05	5.00E-06	0.00423	0.00559	1700	200	W2447
1.30E-05	8.51E-06	0.00559	0.0071	1750	200	W2447
2.60E-05	1.51E-05	0.0071	0.0096	1800	200	W2447
5.20E-05	3.16E-05	0.0096	0.0148	1850	200	W2447
2.25E-06	1.70E-06	0.0055	0.007	1325	400	W2439
2.80E-06	2.38E-06	0.007	0.009	1350	400	W2439
3.40E-06	2.70E-06	0.009	0.011	1370	400	W2439
3.80E-06	2.80E-06	0.011	0.0133	1390	400	W2439
4.00E-06	3.24E-06	0.0133	0.016	1410	400	W2439
5.00E-06	4.35E-06	0.016	0.019	1430	400	W2439
6.90E-06	5.00E-06	0.019	0.023	1450	400	W2439
7.80E-06	6.20E-06	0.023	0.028	1470	400	W2439
9.40E-06	7.70E-06	0.028	0.0325	1490	400	W2439
1.05E-05	9.80E-06	0.0325	0.036	1510	400	W2439
1.40E-06	8.82E-07	0.0005	0.00138	1062	550	W2424
1.60E-06	1.14E-06	0.00138	0.0024	1088	550	W2424
3.00E-06	1.56E-06	0.0024	0.00373	1137	550	W2424
2.60E-06	1.90E-06	0.00373	0.00474	1162	550	W2424
5.40E-06	2.56E-06	0.00474	0.00705	1212	550	W2424
7.50E-06	3.40E-06	0.00705	0.0106	1261	550	W2424
9.00E-06	4.80E-06	0.0106	0.015	1311	550	W2424

Continuation of Table 2.3						
1.40E-05	1.05E-05	0.015	0.023	1361	550	W2424
8.00E-09	5.00E-09	0.0001	0.001	480	520	W2520
2.20E-08	1.70E-08	0.001	0.0022	600	520	W2520
4.00E-08	3.40E-08	0.0022	0.0033	690	520	W2520
8.00E-08	6.00E-08	0.0033	0.0048	790	520	W2520
9.50E-08	7.50E-08	0.0048	0.0063	880	520	W2520
5.00E-09	4.50E-09	0.0063	0.0067	470	520	W2520
1.40E-07	1.20E-07	0.0067	0.018	970	520	W2520
1.41E-09	1.40E-09	0.0001	0.0003	1230	76	W2521
4.00E-09	2.50E-09	0.0003	0.0005	1280	76	W2521
8.00E-08	5.00E-09	0.0005	0.0008	1330	76	W2521
2.50E-08	1.50E-08	0.0008	0.0015	1380	76	W2521
5.00E-08	3.00E-08	0.0015	0.0028	1430	76	W2521
2.50E-07	6.00E-08	0.0028	0.0046	1480	76	W2521
1.60E-06	1.50E-07	0.0046	0.00758	1550	76	W2521
1.50E-06	3.00E-07	0.00758	0.011	1580	76	W2521
2.00E-06	6.00E-07	0.011	0.0147	1600	76	W2521
2.20E-06	5.00E-07	0.0147	0.0198	1650	76	W2521
3.30E-06	1.00E-06	0.0198	0.022	1700	76	W2521
9.00E-06	2.00E-06	0.022	0.0257	1750	76	W2521
1.20E-05	5.00E-06	0.0257	0.032	1800	76	W2521
1.10E-08	3.00E-09	0.0323	0.0325	1510	76	W2521
8.00E-09	6.00E-09	0.0325	0.0326	1560	76	W2521
1.10E-08	8.00E-09	0.0326	0.0328	1620	76	W2521
1.50E-08	8.00E-09	0.0328	0.033	1670	76	W2521
2.30E-08	2.00E-08	0.033	0.0333	1710	76	W2521
1.00E-07	4.00E-08	0.0333	0.0353	1720	76	W2521

Continuation of Table 2.3						
3.20E-07	1.50E-07	0.0353	0.0383	1750	76	W2521
7.00E-08	1.50E-08	0.0001	0.0002	635	480	W2526
5.00E-09	2.50E-09	0.0002	0.0005	475	480	W2526
1.00E-08	7.50E-09	0.0005	0.001	575	480	W2526
1.20E-08	1.00E-08	0.001	0.0013	645	480	W2526
3.00E-08	2.50E-08	0.0013	0.0021	725	480	W2526
2.00E-07	1.50E-07	0.0021	0.0028	975	480	W2526
8.00E-09	5.00E-09	0.0028	0.0032	505	480	W2526
1.50E-08	9.00E-09	0.0032	0.0036	595	480	W2526
1.90E-08	1.50E-08	0.0036	0.004	695	480	W2526
3.50E-08	3.00E-08	0.004	0.0044	795	480	W2526
End of Table						

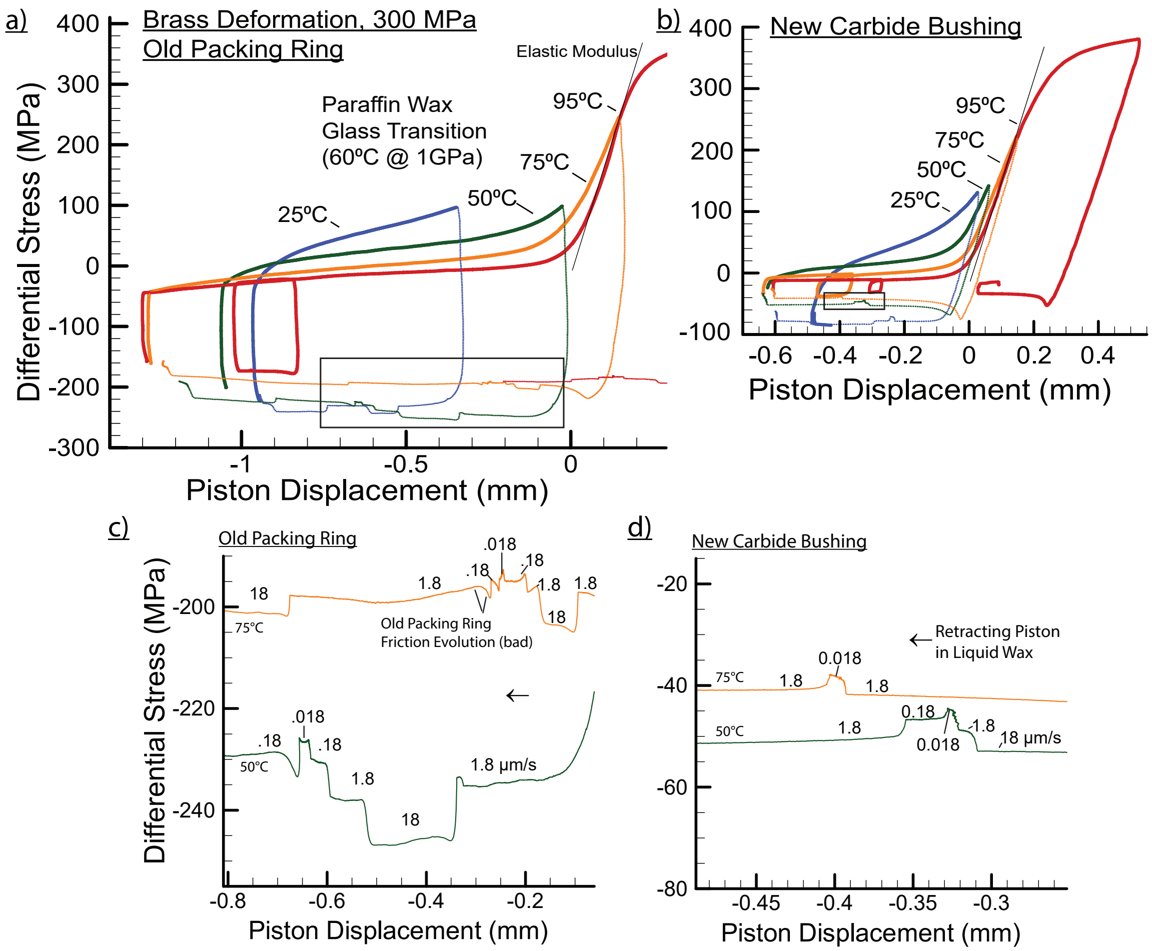

Figure 2.16: Plots of differential stress and displacement data from experiments deforming grade 360 (leaded) brass. Assemblies have no furnace, and all confining media is paraffin wax. Samples were first pressurized to 300 MPa. Then the piston was advanced towards the sample, retracted, heated, and advanced again repeatedly. Retraction is plotted as thin dotted lines. Hysteresis between advancing and advancing stresses is a measure of seal friction (30 MPa new carbide, 140 MPa old packing ring). Rate steps were completed while retracting far from the sample to measure rate dependent friction.

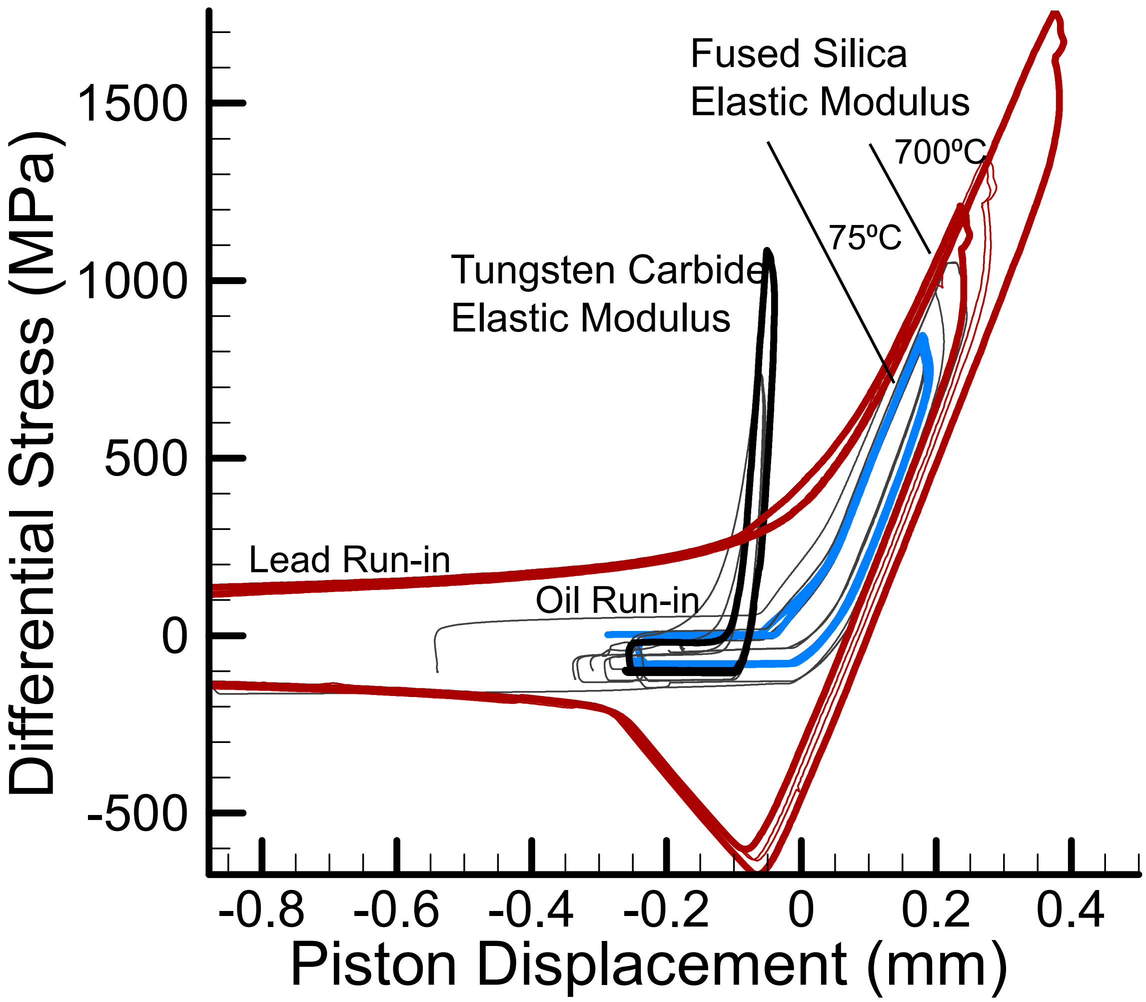

Figure 2.17: Elastic tests of fused silica at room temperature in hydraulic oil and a solid salt assembly at 700°C with traditional packing rings. Despite the differences in friction and hit quality, load and displacement data match at high loads indicating correct calibration of our load and displacement transducers in both new and old assemblies.

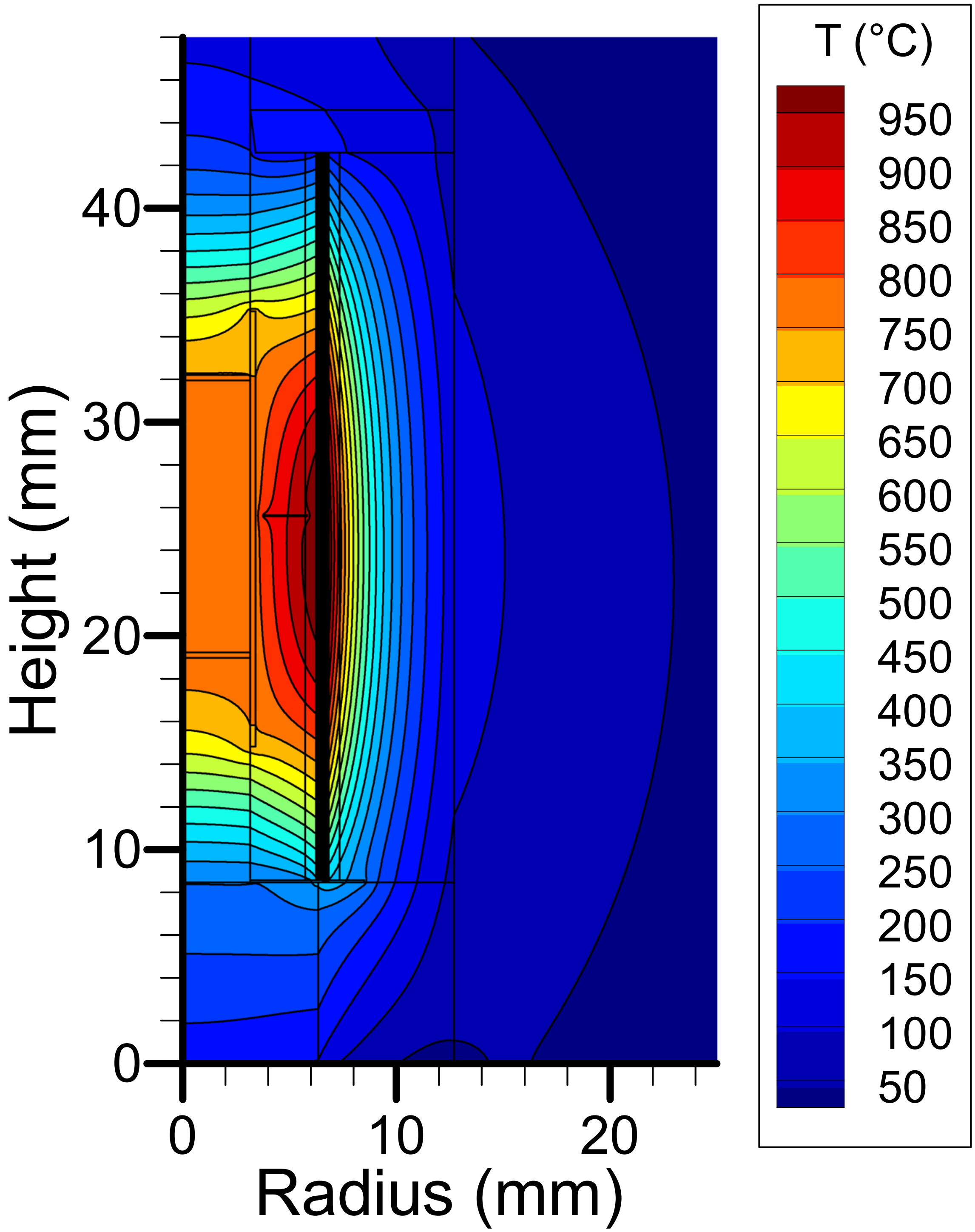

Figure 2.18: Thermal model results. Methods are detailed in Moarefvand et al. (2021)

2.7 Dehydrating Creep Data

Additional data was collected at 620°C using the same methods, materials, and assembly as other creep experiments above 400°C. This is slightly above the reaction equilibrium line between antigorite and Forsterite+Talc (Wunder and Schreyer, 1997). The deviation from behavior of lower temperature samples is notable, but possibly an entirely different and not fully explored mechanism so it is addressed here separately.

Mechanical data is plotted in Figure 2.19 and Figure 2.20. Stresses of only 500 MPa are needed to deform the sample at $10^{-}6$ 1/s, two orders of magnitude faster than predictions of the unreacted antigorite flow law. Surprisingly, strain rate does display a systematic dependence on stress, with a power law exponent of 2.3. Strain rate evolution (hardening) is difficult to examine because experiments were completed in several hours to avoid significant reaction.

Recovered samples have less intergranular porosity and relict shear cracks than lower temperature samples, with significantly more decompression cracks. This particular sample has a single, localized fault at 35° to axial stress running one third of the length of the sample which terminates before it reaches the edge of the sample (figure 2.21). Approximately 100 μm offset is still visible at the top surface where the crack initiated, corresponding to the amount of stick-slip observed in mechanical data of the last loading step (Figure 2.20. Outside of the fault there are no signs of the kinking and shear-accommodated plasticity that lower temperature samples display. The fault is generally smooth and straight, with little gouge. There are several sections in which grains were originally oriented nearly perpendicular to the fault plane. The fault is rougher in these poorly oriented sections, and grains are bent around by fault slip, tearing to form fault gouge. Several of these sections have high backscatter contrast, which could indicate reaction, but this is difficult to distinguish from edge contrast from the sharp edges of the fault and individual grains.

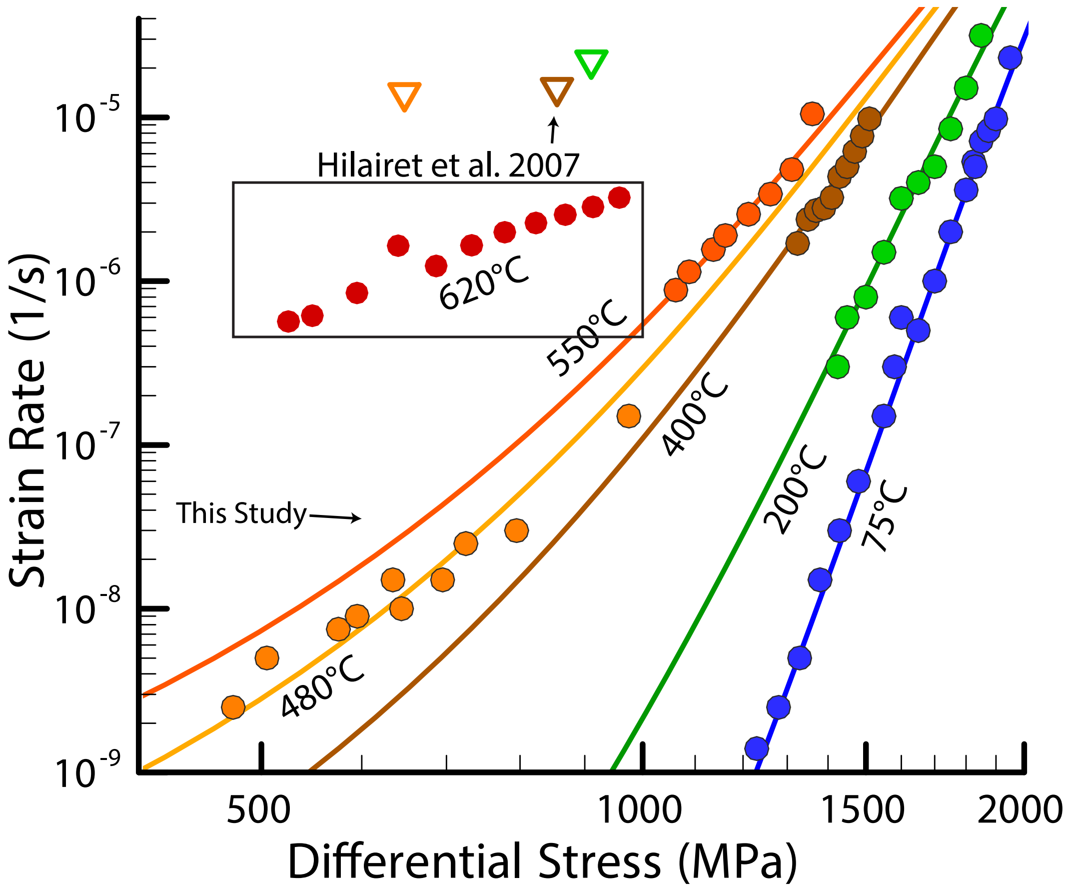

Figure 2.19: Antigorite creep data including partially dehydrating data.

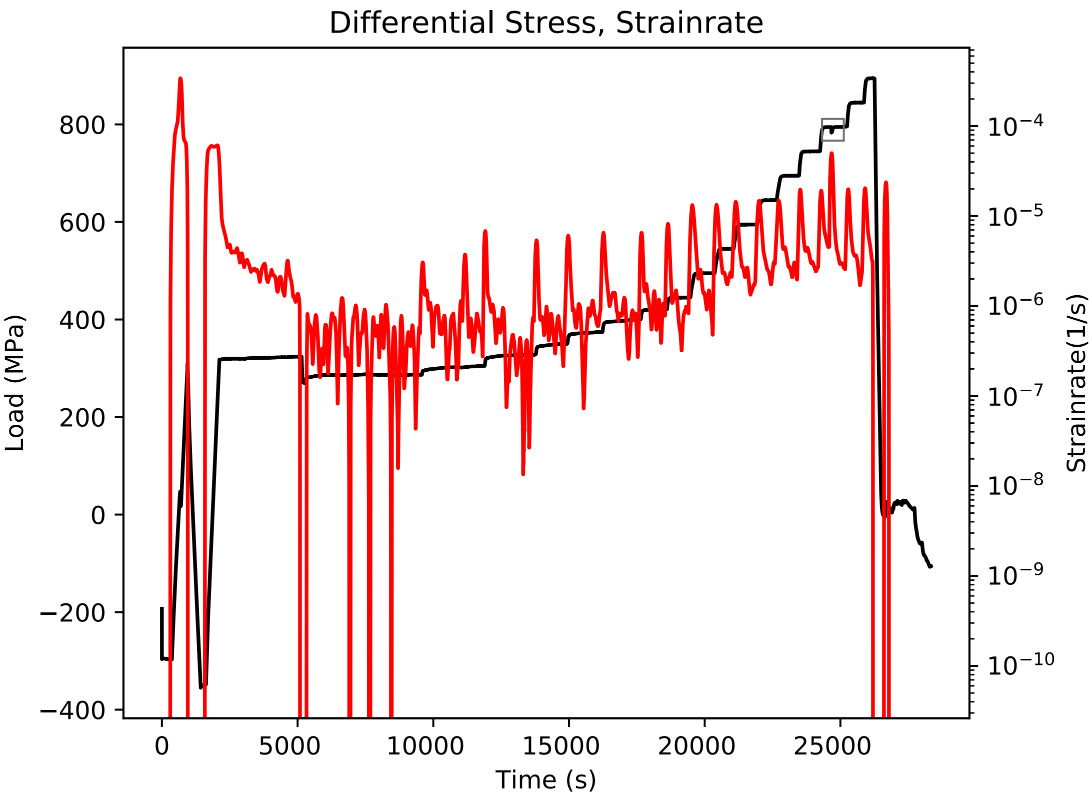

Figure 2.20: Stress (black), and strain rate (red) during creep of antigorite at 620°C. Gray box highlights stick-slip event.

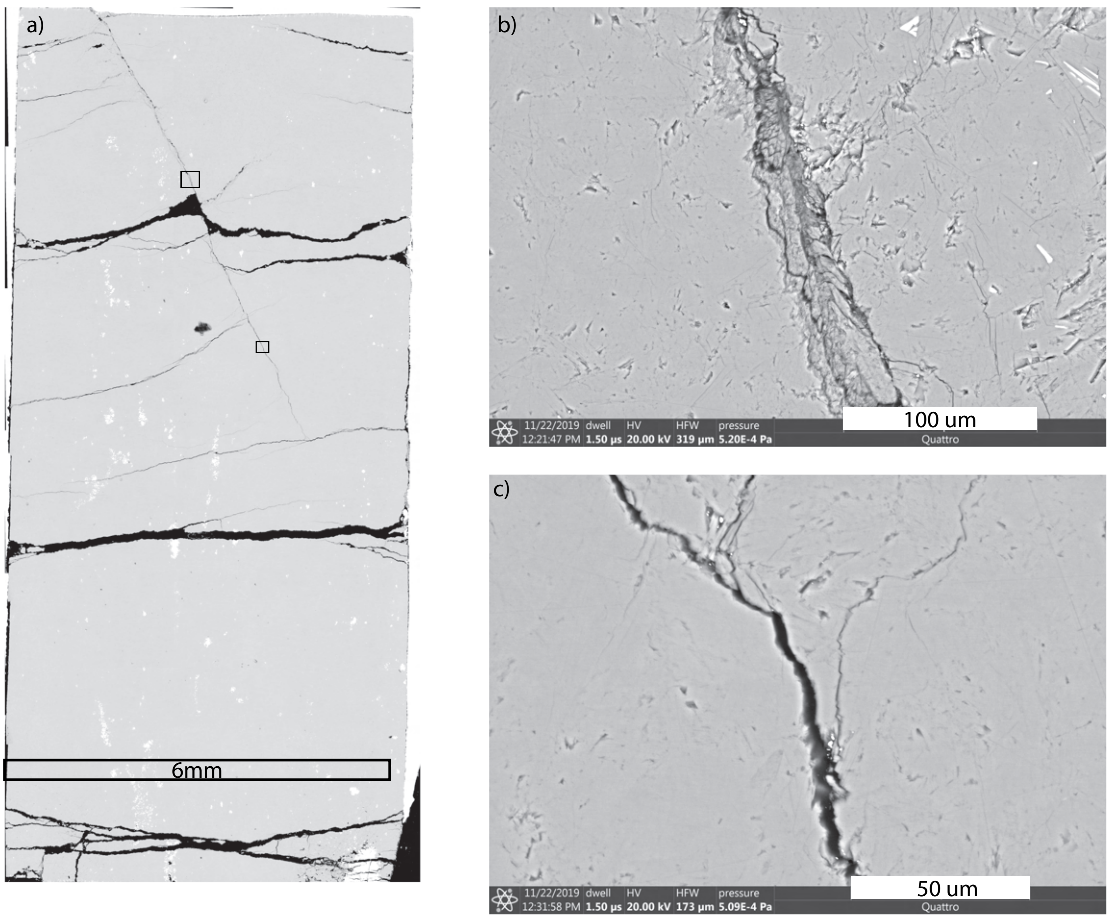

Figure 2.21: a) Wide SEM image showing entire 620°C creep sample. Horizontal cracks are opened during decompression. A fault formed during deformation is visible running from the top left corner through the sample. Offset of this fault is Approximately 100 μm. b) Zoomed in view of a poorly oriented section of the fault showing grains bent nearly 120 degrees and heavily damaged. c) Zoomed in view of a smooth section of the fault.

Chapter 3

Stability of Rate-State Frictional Faults in Sawcut Triaxial Geometry.

Eric Burdette

[1]Department of Earth, Environmental and Planetary Sciences, Brown University, Providence, RI, USA

Key Points:

- High and low angle faults are less stable
- Our results follow Dieterich and Linker (1992), adding an explicitly defined compliance
- Stiff confining media is surprisingly ineffective for stabilizing faults, while friction between pistons strongly destabilizes faults

Abstract

The frictional stability of a confined saw-cut fault is not only a function of frictional rate parameters, but also fault angle, friction coefficient, and external forces resisting movement of the fault. We re-derive a relationship which experimentalists can use to assess stick-slip stability between different machines and experiments on the same material. As Dieterich and Linker (1992) found, very high angle and very low angle faults are theoretically less stable. Additional Experimental factors also affect stability. Confining resistance is only mildly stabilizing, while fault parallel shear resistance is strongly stabilizing. Friction between pistons is surprisingly destabilizing because it substantially increases normal stress. Low and high angle natural faults are predicted to be particularly unstable, even though they would rarely rupture due to the large stresses required.

3.1 Introduction

Rock friction is an important tectonic parameter relevant for crustal strength, faulting, and earthquakes. Standard methods for studying rock friction involve pressing two blocks together with gouge material in between and controlling their shear displacement (direct shear configuration). In unconfined geometry this test is relatively simple to accomplish with square blocks and two hydraulic rams. For confined (triaxial) stress conditions present in the earth due to overlying rock, a hydrostatic pressure must be applied, which is commonly accomplished with a gas or soft solid surrounding the sample compressed in a cylindrical pressure vessel. For friction studies, two matched pistons are cut at some angle ψ and pressed together with gouge in between (Figure 3.1). Shear stress is applied by increasing axial force σ_1. Confining pressure σ_3 is applied perpendicular to axial force. In this configuration there is geometric coupling between shear stress and normal stress that prevents direct use of mechanical stability relations formulated for constant normal stress. Studying geologic materials at relevant confining pressures to study earthquakes in a variety of tectonic environments requires the use of triaxial confined saw-cut piston geometry (Figure 3.1), despite its complexity. Here we present frictional stability conditions for saw-cut triaxial samples following the approach outlined by Dieterich and Linker (1992) and include cases for several common sources of experimental error.

3.2 Stability of Triaxial Samples

3.2.1 Standard Saw-cut Geometry

A sample with frictional parameters μ_0, A, B, and D_c, under confining pressure σ_3 will be stable if axial stiffness $K_{ax} = \frac{\Delta\sigma_1}{\Delta x}$ satisfies the inequality:

$$K_{ax,stable} \geq \frac{2}{\cos(\psi)\sin(2\psi)} \frac{\sigma_3}{1-\mu_0\tan(\psi)} \frac{(B-A)}{D_c} \frac{1}{1-(\mu_0-\alpha)\tan(\psi)} \tag{3.1}$$

The variables used here have the same meaning as those of Ruina (1983) (μ_0 is friction coefficient, A is the rate strengthening coefficient, B is rate weakening coefficient, and D_c is characteristic weakening distance). Variable x is displacement in the axial loading direction of σ_1. This relationship shares terms with the relationship derived in Dieterich and Linker (1992), but also explicitly describes a measurable machine stiffness K_{ax} (axial stiffness), and has normal stress σ_n in terms of measurable quantities σ_3 and μ_0 (Figure 3.2) The conversions are written here and the full derivation can be found in the supplement.

$$K_{D\&L(1992)} = \frac{d\tau}{d\delta} = \frac{d\sigma_1}{dx} \frac{\sin(2\psi)}{2} \cos\psi \tag{3.2}$$

$$\sigma_n = \frac{\sigma_3}{1-\mu_0\tan(\psi)} \tag{3.3}$$

Here τ is shear stress, σ_n is normal stress, and δ is displacement on the saw-cut fault. The unstable regimes of the new relationship shares the characteristic of fault locking above angles $\psi > arctan(\frac{1}{\mu_0})$ (Figure 3.2). In addition fault behavior becomes asymptotically unstable as fault angle (ψ) approaches 0. This is due to reduced shear compliance (3.1, 3.2, 3.27). This effect could also be important in natural settings for low angle faults.

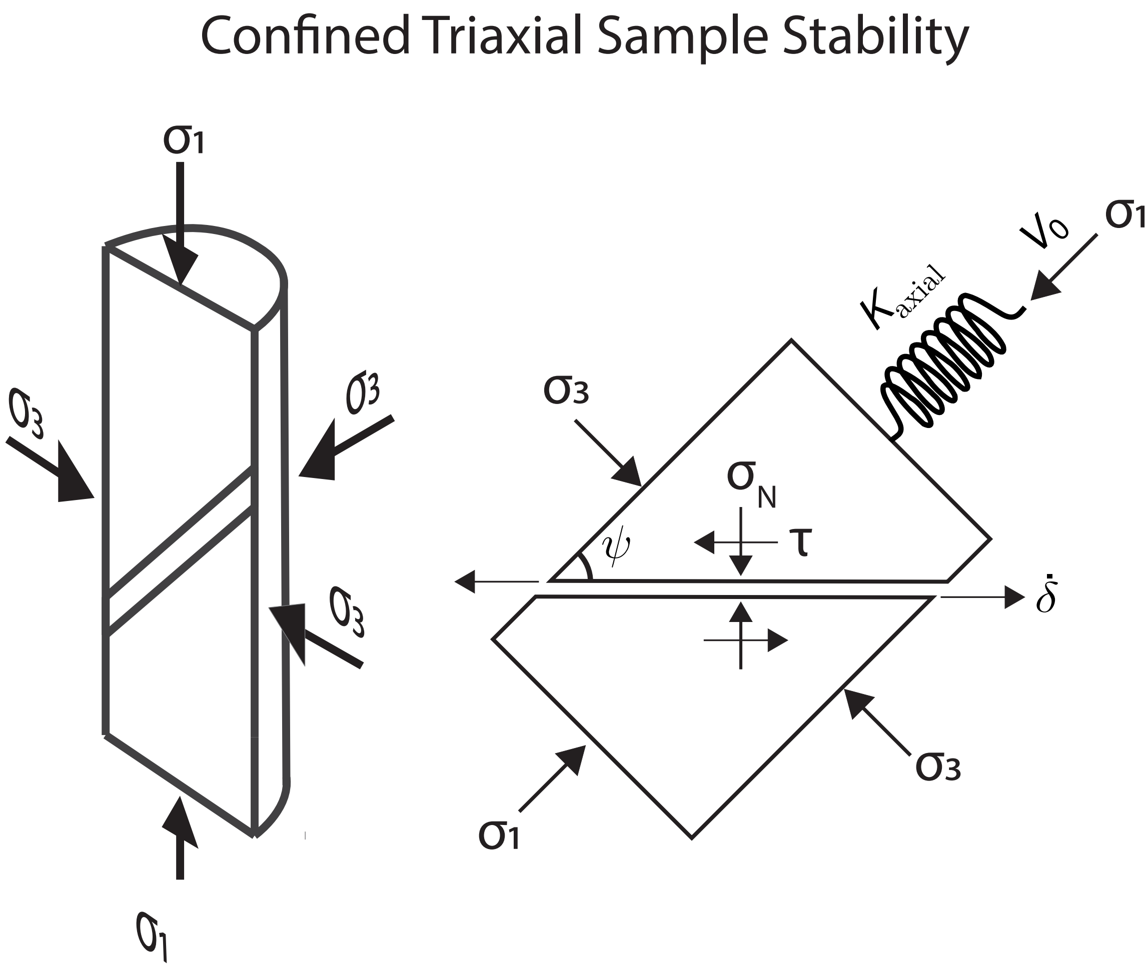

Figure 3.1: Geometry of a triaxially confined gouge sample between two shear pistons with a schematic spring element included to represent machine stiffness. Confining stress is labeled σ_3 and axial stress is labelled σ_1. The sign convention for the angle of the fault plane to axial stress (ψ) follows Karato (2008) instead of Dieterich and Linker (1992)

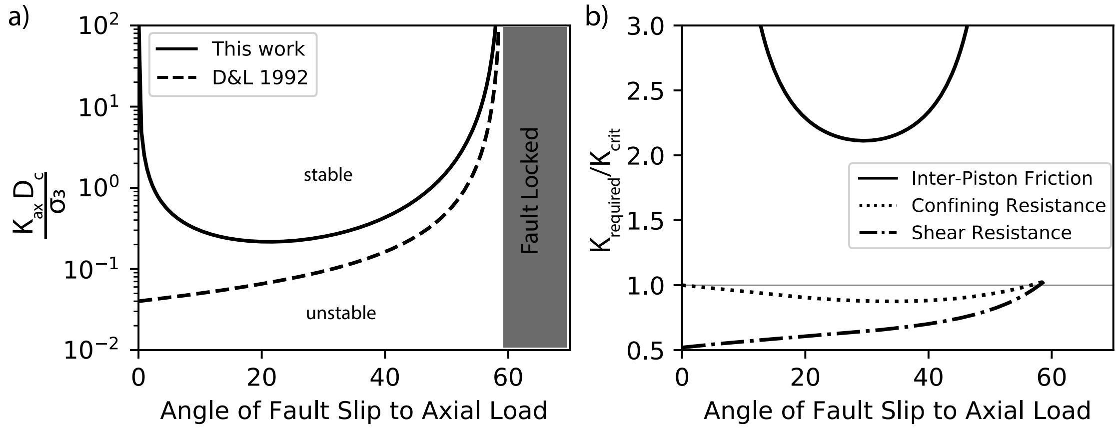

Figure 3.2: **a)** Plot of pressure normalized critical stiffness vs fault angle in a triaxial apparatus ($\mu_0 = 0.6, A = 0.05, B = 0.1$) **b)** Plot of critical stiffness of each apparatus effect relative to standard critical stiffness

3.2.2 Effects of Inter-Piston Friction

Frictional resistance in the direction of σ_3 will decrease sample stability by increasing fault normal stress. Cylindrical saw-cut deformation columns have an interface between an axial piston (not pictured) and the saw-cut piston so that the saw-cut piston can move normal to σ_1. If this interface were frictionless it would not affect results, but it has some resistance in practice. The piston interface friction μ_r, which is always normal to σ_1 can be simply added to the confining resistance as:

$$\sigma_3' = \sigma_3 + \mu_r \sigma_1 \tag{3.4}$$

When this is used in the derivation it results in both changes in steady state normal stress as well as the stiffness inequality:

$$\sigma_{n,ss} = \frac{\sigma_3}{1 - \mu_r - \mu_0 \left(\mu_r \cot(\psi) + \tan(\psi)\right)} \tag{3.5}$$

$$K_{ax} \geq \frac{2}{\cos(\psi)} \sigma_{n,ss} \frac{(B-A)}{D_c} \frac{1}{(1-\mu_r)\sin(2\psi) - (\mu_0 - \alpha)\left(1 - \cos(2\psi) + \mu_r(1 + \cos(2\psi))\right)} \tag{3.6}$$

Both of these quantities are greater (less stable) than their standard counterparts and a piston interface friction coefficient of 0.1 will double required axial stiffness to stabilize 30 degree faults (Figure 3.2).

3.2.3 Effect of Confining Resistance

Some triaxial apparatuses use weak solids/liquids around their samples. The confining media presents resistance to piston expansion normal to axial stress. This can be easily represented by adding a linear viscosity to σ_3 :

$$\sigma_3' = \sigma_3 + \eta\dot{\delta}\sin(\psi) \tag{3.7}$$

This can be used to derive the stability inequality:

$$\sigma_{n,ss} = \frac{\sigma_3 + \eta\dot{\delta}_{ss}\sin(\psi)}{1-\mu_0\tan(\psi)} \tag{3.8}$$

$$K_{ax} \geq \frac{1}{\cos(\psi)\sin(2\psi)}\frac{1}{(1-(\mu_0-\alpha)\tan(\psi))}\frac{1}{D_c}\Big(2\sigma_{n,ss}(B-A)-\mu_0\eta\dot{\delta}_{ss}\sin(\psi)(1+\sin(2\psi)+\cos(2\psi))\Big) \tag{3.9}$$

The resulting stability inequality has higher normal stress, but also terms resisting high speed fault movement, which have opposing effects on stability (Table 3.1). In most cases confining resistance does not substantially affect fault stability (Figure 3.2).

3.2.4 Effect of Shear Drag

Most triaxial pistons are covered in rubber or metal jackets whose resistance can easily be represented by a linear viscous term ($\eta\dot{\delta}$) added to shear stress. The effect opposes velocity weakening and stabilizes faults.

$$\sigma_{n,ss} = \frac{\sigma_3 + \eta\dot{\delta}_{ss}\tan(\psi)}{1-\mu_0\tan(\psi)} \tag{3.10}$$

$$K_{ax} \geq \frac{1}{\cos(\psi)\sin(2\psi)} \frac{1}{1-(\mu_0-\alpha)\tan(\psi)} \frac{1}{D_c} \left(2\sigma_{n,ss}(B-A) - 2\eta\dot{\delta}_{ss}\right) \tag{3.11}$$

The stabilization provided by viscous strengthening can be very strong and is especially effective on shallow faults due to their low shear stresses (Figure 3.2).

3.3 Piston Offset Stiffness Effects

The triaxial piston geometry has a significant limitation in that area of contact changes during slip. This causes stress for a given force to increase ($\tau_f ault$, equation 3.15) on the effective fault which also changes effective stiffness to decrease. To illustrate this we switch displacement to a general fractional shear length s ($\frac{slip}{\text{fault length}}$) and consider fault shear stress τ:

$$s(\delta) = \frac{\delta}{d_0/\sin\psi} \tag{3.12}$$

$$f(s) = \frac{\text{Area}}{\text{Area}_0} = 1 - 1.2082s - 0.19134s^2 + 0.39461s^3 \tag{3.13}$$

where piston diameter is d_0. $f(s)$ is a polynomial less than 1 for slip s from 0 to 1. We can define the spring portion of a block-slider system in terms of fractional slip:

$$\tau_{\sigma_1}(s) = \tau_{\sigma_1,ss} - K_{d\tau_{\sigma_1},ds} * (s - s_{ss}) \tag{3.14}$$

where τ_{σ_1} is shear stress calculated from applied load and geometry, ss denotes steady-state, and stiffness $K_{d\tau_{\sigma_1},ds}$ is defined in terms of axial/geometric quantities that do not change with slip (see supplement). The affect of area change can then be accounted for:

$$\tau_{fault} = \tau_{sigma_1}(s)/f(s) \tag{3.15}$$

where τ_{fault} is shear stress on the portion of the fault in contact. We are interested in the fault properties so we need to substitute eq. 3.14 into 3.15, and then differentiate with respect to s using

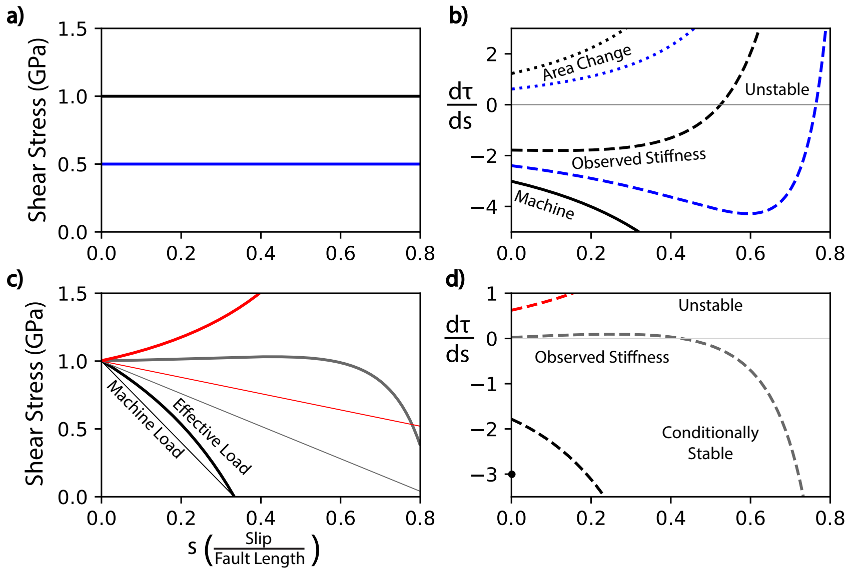

Figure 3.3: **a)** Constant applied shear stress at two levels vs s ($K_{\tau,s} = 3$) **b)** Resulting shear stress derivatives split into area reduction contribution (dotted), machine stiffness change (solid), and the resulting instantaneous combined stiffness (dashed) **c)** Relaxation shear stress vs s (machine=thin, area corrected=thick) for three different machine stiffnesses (3 GPa/mm (black), 1.2 GPa/mm (grey), and 0.6 GPa/mm (red)) on a quarter inch diameter sample with a 45 degree fault. **d)** Relaxation area corrected instantaneous stiffness vs s.

the product rule which yields:

$$\frac{d\tau_{fault}}{ds}(s) = \tau_{\sigma_1}(s) * \frac{-1}{f^2}\frac{df}{ds} - K_{\tau,s}/f(s) \tag{3.16}$$

The two resulting terms for effective slip stiffness counteract each other. They also always have different polynomial orders which allows the possibility of transitional stability.

The most important effect to note is that steady-state shear stress controls the first term in equation (3.16). If starting load is too high, effective stress will only increase during unloading and the fault will always be unstable (Figure 3.3).

Table 3.1: Experimental influences on stability.

Effect Type	Stability?	Normal Stress	Velocity Dependence
Inter-Piston Friction	Less Stable	Increases	No Change
Confining Resistance	More Stable	Increases	Rate Strengthens
Shear Resistance	More Stable	No Change	Rate Strengthens

3.4 Implications

3.5 Apparatus Application

Okazaki and Katayama (2015) observe stick-slip in antigorite at 250 MPa confining pressure, with shear stiffness of 58 MPa/mm, a steady state friction coefficient of 0.7 and a saw-cut piston angle of 30 degrees. A-B is -0.005 with a transition to the relevant negative values above 500C. Proctor and Hirth (2015) do not observe stick-slip at 1000 MPa confining pressure with axial stiffness of 2 GPa/mm, steady-state friction coefficient of 0.4 and a saw-cut piston angle of 45 degrees. Burdette and Hirth (2020) observe shear heating, but no unstable-stick slip under the same conditions as Proctor and Hirth (2015) with axial stiffness reduced by an order of magnitude.

3.5.1 Laboratory Implications

Observing instability in the laboratory is important for understanding earthquake phenomena. Accuracy in measurements is critical for extrapolating the observed data to the earth so the derived relationships should be incorporated into stability assessments. A few rules of thumb are substantiated here: stiff machines prevent instability and stability determination is most accurate at low fault displacement. A few new rules should be considered: friction between axial and shear pistons should be minimized, and low fault angles may be unexpectedly unstable. A summary of each of the external experimental effects on stability is presented in the table below.

3.6 Conclusions

1. Confined saw-cut fault stability is not only a function of frictional rate parameters, but also fault angle, friction coefficient, and external forces resisting movement of the fault.

2. We derive a relationship which experimentalists can use to assess stick-slip stability between different machines and experiments on the same material.

3. Very high angle and very low angle faults are theoretically less stable.

4. Experimental conditions affect stability. Confining resistance is only mildly stabilizing, while fault parallel shear resistance is strongly stabilizing. Friction between pistons is surprisingly destabilizing because it substantially increases normal stress.

5. Low and high angle natural faults are predicted to be unusually unstable, even though they rarely rupture due to the large stresses required.

Acknowledgments

I would like to thank Jim Dieterich for kindly providing his notes from the original derivation.

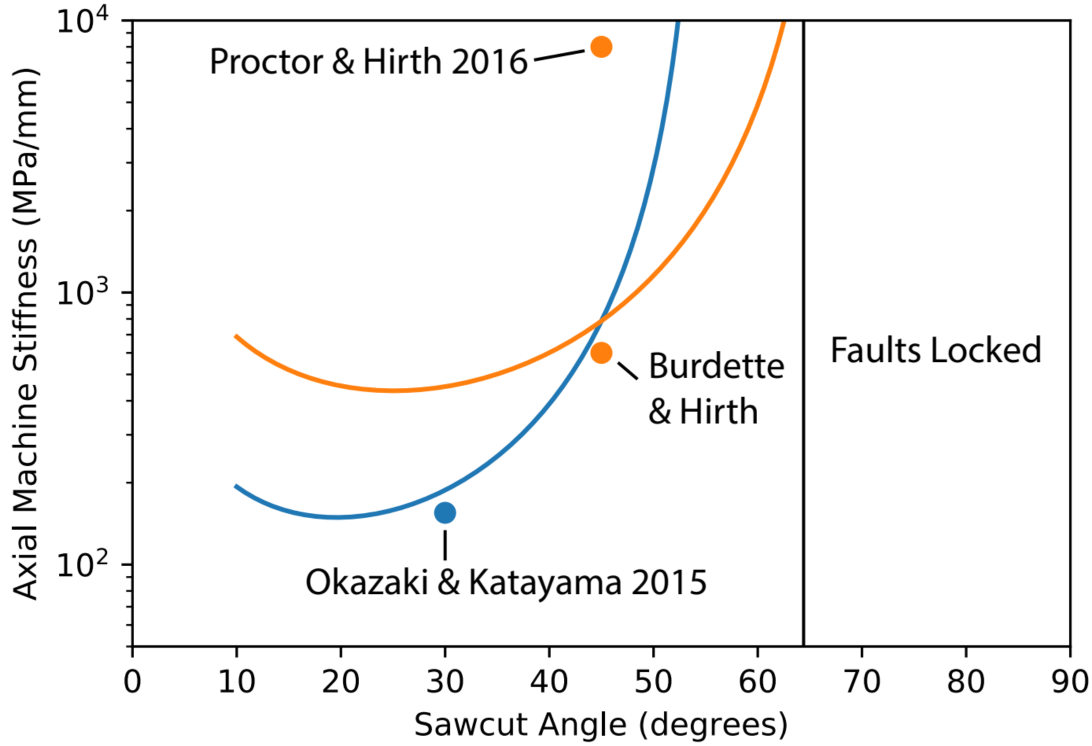

Figure 3.4: Plot of required machine stiffness for stable sliding of gouge between saw-cut pistons in triaxial compression. The blue line was determined using parameters from Okazaki and Katayama (2015) ($\mu_0 = 0.7, A - B = -0.005, Dc = 55\mu m, \sigma_3 = 250MPa$), and the blue point is at the conditions of 600C experiments showing slow-slip. The orange line (higher up in the figure) was calculated with measured friction and confining pressure from Proctor and Hirth (2015) ($\mu_0 = 0.5, \sigma_3 = 1000MPa$). Orange Dots correspond to run conditions of standard stiffness experiments of Proctor and Hirth (2015), and reduced stiffness experiments of Burdette and Hirth (2020).

3.7 Supplemental Normal Stress Algebra

For a confined, axially loaded piston with a plane whose normal is rotated ψ from the compression axis (Karato, 2008):

$$\tau = \frac{\sigma_1 - \sigma_3}{2} \sin(2\psi) \tag{3.17}$$

$$\sigma_n = \frac{\sigma_1 + \sigma_3}{2} - \frac{\sigma_1 - \sigma_3}{2} \cos(2\psi) \tag{3.18}$$

$$\sigma_n = \frac{\sigma_1 + \sigma_3}{2} - \frac{\tau}{\sin(2\psi)} \cos(2\psi) \tag{3.19}$$

$$\sigma_n = \frac{\tau}{\sin(2\psi)} + \frac{\sigma_3}{2} + \frac{\sigma_3}{2} - \frac{\tau}{\sin(2\psi)} \cos(2\psi) \tag{3.20}$$

$$\sigma_n = \sigma_3 + \tau \frac{1 - \cos 2\psi}{\sin 2\psi} \tag{3.21}$$

$$\cos 2\psi = 1 - 2\sin^2 \psi \tag{3.22}$$

$$\sin 2\psi = 2 \sin \psi \cos \psi \tag{3.23}$$

$$\sigma_n = \sigma_3 + \tau \tan \psi \tag{3.24}$$

3.8 Supplemental Derivation of Stability Relationships

While the relations derived by Dieterich and Linker (1992) cover one aspect of the coupling of shear and normal stress to find a value of friction for the rate-state equation, the stiffness of the machine is ambiguously defined. Here we repeat their derivation and include the derivation of axial to shear stiffness.

3.8.1 Derivation of Rate-State Fault Stability in Axisymmetric Saw-Cut Deformation Geometry (Triaxial)

Rate-state friction behavior of a block slider can be described by the equations: (Dieterich and Linker, 1992)

$$\tau = \sigma_n \left(\mu_0 + \mathrm{Aln}\left(\frac{\dot{\delta}}{\dot{\delta}_{ss}}\right) + \mathrm{Bln}\left(\frac{\theta}{\theta_0}\right)\right) = F\left(\dot{\delta}, \theta, \sigma_n\right) \tag{3.25}$$

$$\dot{\theta} = 1 - \frac{\theta\dot{\delta}}{D_c} - \frac{\alpha\theta\dot{\sigma_n}}{B\sigma_n} = G\left(\dot{\delta}, \theta, \sigma_n\right) \tag{3.26}$$

For a confined, axially loaded piston with a plane which is rotated ψ from the compression axis (Karato, 2008):

$$\tau = \frac{\sigma_1 - \sigma_3}{2}\sin(2\psi) \tag{3.27}$$

$$\sigma_n = \frac{\sigma_1 + \sigma_3}{2} - \frac{\sigma_1 - \sigma_3}{2}\cos(2\psi) \tag{3.28}$$

Eliminating σ_1:

$$\sigma_n = \sigma_3 + \tau\tan(\psi) \tag{3.29}$$

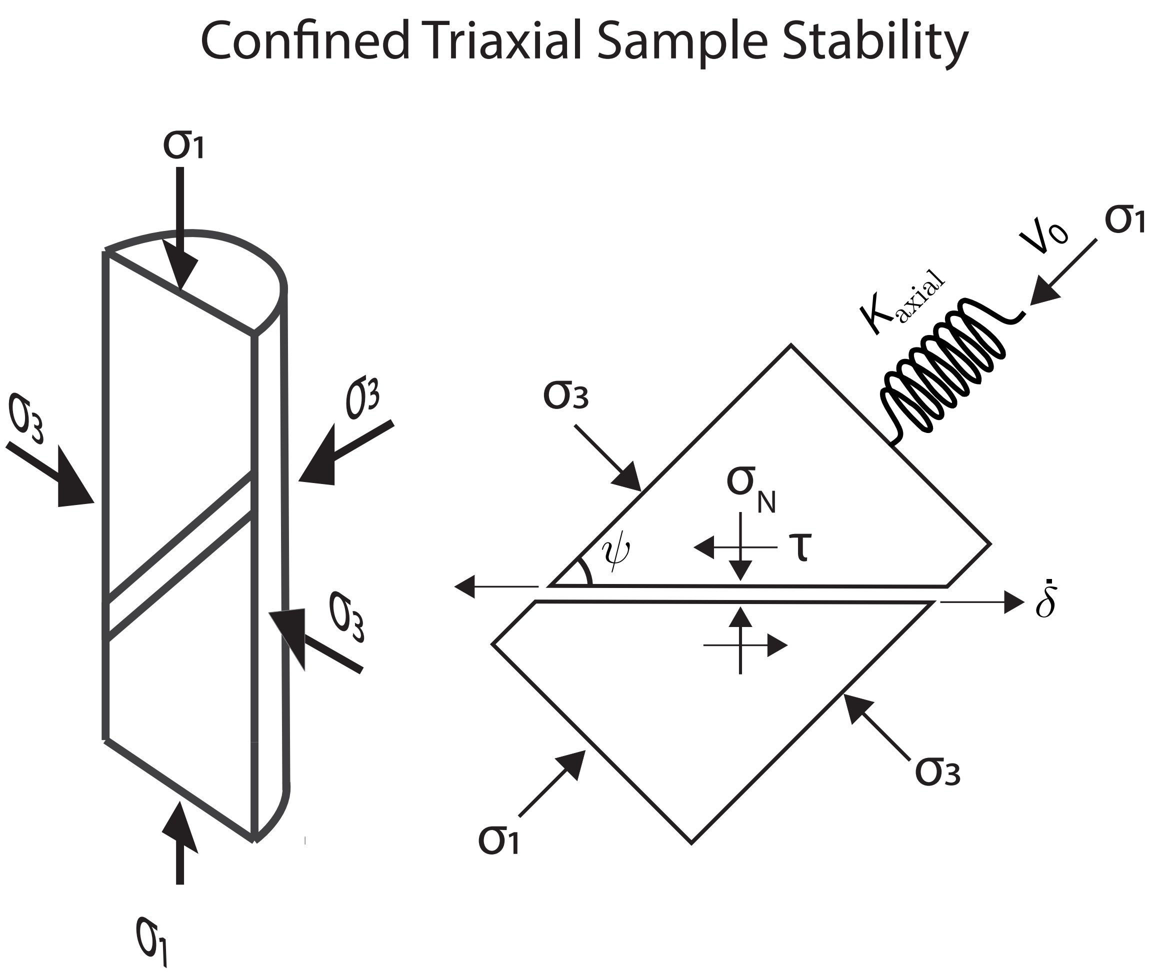

Figure 3.5: Geometry of a triaxially confined gouge sample between two shear pistons with a schematic spring element to represent machine stiffness included. Confining stress is labeled σ_3 and axial stress is labelled σ_1. The sign convention for the angle follows Karato (2008) instead of Dieterich and Linker (1992).

For the rest of the analysis we assume confining stress (σ_3) to be constant. Stability analysis is performed for perturbations about a steady state: $\tau = \tau_{ss},\ \theta = \theta_{ss},\ \dot{\delta} = \dot{\delta}_{ss},$ and $\sigma_n = \sigma_{n,ss}$ for both shear stress and state:

$$\hat{\tau} = \frac{\partial F}{\partial \dot{\delta}}\hat{\dot{\delta}} + \frac{\partial F}{\partial \theta}\hat{\theta} + \frac{\partial F}{\partial \sigma_n}\hat{\sigma_n} \tag{3.30}$$

$$\hat{\dot{\theta}} = \frac{\partial G}{\partial \dot{\delta}}\hat{\dot{\delta}} + \frac{\partial G}{\partial \theta}\hat{\theta} + \frac{\partial G}{\partial \sigma_n}\hat{\sigma_n} \tag{3.31}$$

For a block - slider type system, the shear force is balanced by force in the spring (for sign conventions see Ruina (1983)) :

$$\sigma_1 = K_{ax}\left(v_{0,ax}t - x_{ax} + L_{ss}\right) \tag{3.32}$$

The relation between angled fault displacement and axial displacement is:

$$x_{ax} = \delta\cos\psi, v_0 = \dot{\delta}_{ss}\cos\psi \tag{3.33}$$

$$\sigma_1 = K_{ax}\cos\psi\left(\dot{\delta}_{ss}t - \delta\right) \tag{3.34}$$

Partial derivatives at steady state are:

$$\frac{\partial F}{\partial \dot{\delta}} = \frac{\sigma_{n,ss}A}{\dot{\delta}_{ss}} \tag{3.35}$$

$$\frac{\partial F}{\partial \theta} = \frac{\sigma_{n,ss}B}{\theta_{ss}} \tag{3.36}$$

$$\frac{\partial F}{\partial \sigma_n} = \mu_0 \tag{3.37}$$

State derivatives are more complex. We need to solve in terms of δ and θ so we rearrange normal stress relations in terms to substitute into (3.26).

We use the time derivatives of (3.27), (3.29), and (3.34) to find the normal stress time derivative (numerator in (3.26)):

$$\dot{\sigma_n} = K_{ax}\left(\dot{\delta}_{ss} - \dot{\delta}\right)\sin(\psi)\sin(2\psi)/2 \tag{3.38}$$

Using (3.29), (3.25), and assuming $\theta = \theta_{ss}$ at the time we perturb the system (denominator in (3.26)):

$$\frac{1}{\sigma_n} = \frac{1}{\sigma_3} - \frac{\tan(\psi)}{\sigma_3}\left(\mu_0 + \mathrm{A}\ln\left(\frac{\dot{\delta}}{\dot{\delta}_{ss}}\right)\right) \tag{3.39}$$

Then partial derivatives are:

$$\frac{\partial G}{\partial \dot{\delta}} = -\frac{\theta_{ss}}{D_c} - \frac{\alpha\theta_{ss}}{B}K_{ax}\sin(\psi)\sin(2\psi)\frac{\mu_0\tan(\psi) - 1}{2\sigma_3} \tag{3.40}$$

$$\frac{\partial G}{\partial \theta} = -\frac{\dot{\delta}_{ss}}{D_c} \tag{3.41}$$

$$\frac{\partial G}{\partial \sigma_n} = 0 \tag{3.42}$$

((3.41) is unintuitive until we consider that we substituted (14) whose steady state value is 0)

We would like to solve for only the 2x2 system δ and θ so we need relationships for $\hat{\tau}$ and $\hat{\sigma}$ in terms of shear displacement $\hat{\delta}$. Using (3.27),(3.29), and (3.32):

$$\hat{\tau} = K_{ax}\cos(\psi)\left(-\hat{\delta}\right)\sin(2\psi)/2 \tag{3.43}$$

$$\hat{\sigma_n} = \hat{\tau}\tan(\psi), \hat{\sigma_n} = K_{ax}\sin(\psi)\left(-\hat{\delta}\right)\sin(2\psi)/2 \tag{3.44}$$

Using those in (3.30) we get:

$$K_{ax}\cos(\psi)\left(-\hat{\delta}\right)\sin(2\psi)/2 = \frac{\sigma_{n,ss}A}{\dot{\delta}_{ss}}\dot{\hat{\delta}} + \frac{\sigma_{n,ss}B}{\theta_{ss}}\hat{\theta} + \mu_0 K_{ax}\sin(\psi)\left(-\hat{\delta}\right)\sin(2\psi)/2 \tag{3.45}$$

which reduces to

$$\dot{\hat{\delta}} = \frac{\dot{\delta}_{ss}}{\sigma_{n,ss}A}\left[\frac{K_{ax}\sin(2\psi)}{2}(\mu_0\sin(\psi) - \cos(\psi))\hat{\delta} - \frac{\sigma_{n,ss}B}{\theta_{ss}}\hat{\theta}\right] = a_{11}\hat{\delta} + a_{12}\hat{\theta} \tag{3.46}$$

$$a_{11} = \frac{\dot{\delta}_{ss}}{\sigma_{n,ss}A}\left[\frac{K_{ax}\sin(2\psi)}{2}(\mu_0\sin(\psi) - \cos(\psi))\right] \tag{3.47}$$

$$a_{12} = -\frac{\dot{\delta}_{ss}B}{\theta_{ss}A} \tag{3.48}$$

Now we can solve (3.31). Note that we need to substitute for $\dot{\hat{\delta}}$:

$$\dot{\hat{\theta}} = \left(-\frac{\theta_{ss}}{D_c} - \frac{\alpha\theta_{ss}}{B}K_{ax}\sin(\psi)\sin(2\psi)\frac{\mu_0\tan(\psi) - 1}{2\sigma_3}\right)\dot{\hat{\delta}} + -\frac{\dot{\delta}_{ss}}{D_c}\hat{\theta} = a_{21}\hat{\delta} + a_{22}\hat{\theta} \tag{3.49}$$

$$a_{21} = \left(-\frac{\theta_{ss}}{D_c} - \frac{\alpha\theta_{ss}}{B}K_{ax}\sin(\psi)\sin(2\psi)\frac{\mu_0\tan(\psi) - 1}{2\sigma_3}\right)\frac{\dot{\delta}_{ss}}{\sigma_{n,ss}A}\left[\frac{K_{ax}\sin(2\psi)}{2}(\mu_0\sin(\psi) - \cos(\psi))\right] \tag{3.50}$$

$$a_{22} = \left(\frac{B - A}{D_c} + \alpha K_{ax} \sin(\psi) \sin(2\psi) \frac{\mu_0 \tan(\psi) - 1}{2\sigma_3} \right) \frac{\dot{\delta}_{ss}}{A} \tag{3.51}$$

As Dieterich and Linker (1992) indicates, the square matrix can be solved for its eigenvalues through a quadratic characteristic polynomial. The coefficient of the second term is the trace of the matrix and controls damping so we solve for that to be 0. The system is stable above evaluated critical stiffness and unstable below evaluated critical stiffness. Note the third and fourth portions match the relation presented in Dieterich and Linker (1992), and follow a sign convention of positive values for sawcut angle.

$$K_{ax,stable} \geq \frac{2}{\cos(\psi)\sin(2\psi)} \frac{\sigma_3}{1 - \mu_0 \tan(\psi)} \frac{(B - A)}{D_c} \frac{1}{1 - (\mu_0 - \alpha)\tan(\psi)} \tag{3.52}$$

3.8.2 Inter-Piston Friction

Friction between a guided axial piston and a shear piston sliding horizontally due to compression can be included by modifying the term for confining stress to include a friction term ($\mu_r \sigma_1$) coupled to axial stress. Because no modification is made to F or G, the equations can be worked through in the same way with minor substitutions:

$$\sigma_3' = \sigma_3 + \mu_r \sigma_1 \tag{3.53}$$

$$\sigma_n = \frac{1}{1 - \mu_r} \left(\left(\mu_r \cot(\psi) + \tan(\psi) \right) \tau + \sigma_3 \right) \tag{3.54}$$

$$\hat{\tau} = K_{ax} \cos(\psi) \left(-\hat{\delta} \right) (1 - \mu_r) \sin(2\psi)/2 \tag{3.55}$$

$$\hat{\sigma_n} = K_{ax} \cos(\psi) \left(-\hat{\delta} \right) \left(1 - \cos(2\psi) + \mu_r (1 + \cos(2\psi)) \right)/2 \tag{3.56}$$

$$\sigma_{n,ss} = \frac{\sigma_3}{1 - \mu_r - \mu_0 \left(\mu_r \cot(\psi) + \tan(\psi)\right)} \tag{3.57}$$

$$K_{ax} \geq \frac{2}{\cos(\psi)} \sigma_{n,ss} \frac{(B-A)}{D_c} \frac{1}{(1-\mu_r)\sin(2\psi) - (\mu_0 - \alpha)\left(1 - \cos(2\psi) + \mu_r(1+\cos(2\psi))\right)} \tag{3.58}$$

This is greater (less stable) than (3.39) with $\mu_r > 0$, and reduces to (3.39) when $\mu_r = 0$. In practice the piston contact friction may be larger than bending stiffness of axial forcing rods so this may not be dominant in all cases.

3.8.3 Confining Resistance

Another potential source of stabilization is resistance on the shear pistons moving laterally into the confining media. The resistance could be metal jacket stretching or deformation of the confining media. The formulation is simplified as a general linear velocity dependent resistance η with scale included.

$$\sigma_3' = \sigma_3 + \eta\dot{\delta}\sin(\psi) \tag{3.59}$$

$$\sigma_n = \sigma_3 + \eta\dot{\delta}\sin(\psi) + \tau\tan(\psi) \tag{3.60}$$

$$\hat{\tau} = \frac{1}{2}\sin(2\psi)\left(K_{ax}\cos(\psi)\left(-\hat{\delta}\right) + \eta\sin(\psi)\left(-\dot{\hat{\delta}}\right)\right) \tag{3.61}$$

$$\hat{\sigma_n} = \frac{1}{2}\left((1-\cos(2\psi))K_{ax}\cos(\psi)\left(-\hat{\delta}\right) + (1+\cos(2\psi))\eta\sin(\psi)\left(\dot{\hat{\delta}}\right)\right) \tag{3.62}$$

$$\dot{\sigma_n} = K_{ax}\left(\dot{\delta}_{ss} - \dot{\delta}\right)\sin(\psi)\sin(2\psi)/2 + \eta\ddot{\delta}\sin(\psi)\cos^2(\psi) \tag{3.63}$$

$$\frac{1}{\sigma_n} = \frac{1-\tan(\psi)\left(\mu_0 + \text{Aln}\left(\frac{\dot{\delta}}{\dot{\delta}_{ss}}\right)\right)}{\sigma_3 + \eta\dot{\delta}\sin(\psi))} \tag{3.64}$$

Here we assume that resistance is a secondary effect so the resistance term containing $\ddot{\delta}$ is small and can be neglected.

$$\frac{\partial G}{\partial\dot{\delta}} = -\frac{\theta_{ss}}{D_c} - \frac{\alpha\theta_{ss}}{B}k_{ax}\sin(\psi)\sin(2\psi)\frac{\mu_0\tan(\psi)-1}{2(\sigma_3+\eta\dot{\delta}_{ss}\sin(\psi))} \tag{3.65}$$

$$\sigma_{n,ss} = \frac{\sigma_3 + \eta\sin(\psi)\dot{\delta}_{ss}}{1-\mu_0\tan(\psi)} \tag{3.66}$$

$$K_{ax} \geq \frac{1}{\cos(\psi)\sin(2\psi)}\frac{1}{(1-(\mu_0-\alpha)\tan(\psi))}\frac{1}{D_c}\left(2\sigma_{n,ss}(B-A) - \mu_0\eta\dot{\delta}_{ss}\sin(\psi)(1+\sin(2\psi)+\cos(2\psi))\right) \tag{3.67}$$

The derived stiffness is lower (more stable), with the magnitude of the change roughly proportional to the ratio $\mu_0\eta\dot{\delta}_{ss} : 2\sigma_{n,ss}(B-A)$.

3.8.4 Shear Resistance

Another relevant scenario to consider is viscous support of the fault (Kelvin-Voight like), where a generalized velocity dependent term is added to shear stress, F. This doesn't change any of the geometric relationships, only the partial derivative of F and steady state. The schematic representation could be resistance that only generates shear traction (such as drag along the sides of shear pistons):

$$\tau = \sigma_n\left(\mu_0 + \text{Aln}\left(\frac{\dot{\delta}}{\dot{\delta}_{ss}}\right) + \text{Bln}\left(\frac{\theta}{\theta_0}\right)\right) + \eta\dot{\delta} = F\left(\dot{\delta},\theta,\sigma\right) \tag{3.68}$$

$$\frac{\partial F}{\partial \dot{\delta}} = \frac{\sigma_{n,ss} A}{\dot{\delta}_{ss}} + \eta \tag{3.69}$$

$$\sigma_{n,ss} = \frac{\sigma_3 + \eta \dot{\delta}_{ss} \tan(\psi)}{1 - \mu_0 \tan(\psi)} \tag{3.70}$$

$$K_{ax} \geq \frac{1}{\cos(\psi)\sin(2\psi)} \frac{1}{1 - (\mu_0 - \alpha)\tan(\psi)} \frac{1}{D_c} \left(2\sigma_{n,ss}(B - A) - 2\eta\dot{\delta}_{ss} \right) \tag{3.71}$$

No extra angular terms are present in the resulting stability condition because the resistance directly opposes fault motion regardless of direction and does not depend on normal stress. Steady-state normal stress decreases with decreasing fault angle so at low fault angles the resistance term can be larger and completely stabilize the system.

3.8.5 Triaxial Extension

Normal faults will be addressed here without rotating geometry because stiffness is defined for axial stress σ_1. An extensional fault would have axial stress lower than confining stress, causing the friction coefficient to be negative. Rate dependence A and B do not change. The result is much lower required stiffness for stability at high fault angles due to reduced normal stress.

The external effects can also be addressed with the change in sign required for confining viscosity and inter-piston friction (forces resist direction of movement).

1. Inter-piston friction mildly stabilizes the fault at high angles due to normal stress reduction, but causes locking at very low angles.

2. Confining resistance strongly stabilizes the fault by effectively reducing normal stress.

3. Viscous shear effects stabilize the fault for the same reasons at high stress as low stress. The difference between extension and compression at high angles is the magnitude of the frictional shear stresses (small in extension, large in compression).

3.8.6 Piston Offset

The triaxial piston geometry has a significant limitation in that area of contact changes for slipping pistons with displacement. The area change can be calculated by measuring the cross-correlation of two circles (or ellipses) offset by a fraction of their diameter d_0. For an angled sawcut overlap this is calculated as:

$$s(\delta) = \frac{\delta}{d_0/\sin\psi} \tag{3.72}$$

The area fraction can then be calculated as:

$$f(s) = \frac{\text{Area}}{\text{Area}_0} = 1 - 1.2082s - 0.19134s^2 + 0.39461s^3 \tag{3.73}$$

We refer to this function as $f(s(\delta))$. For two squares (direct shear) the function $f = 1 - s$. The area correction causes stress to increase with increasing displacement even though apparent force is decreasing.

Given a load (fault shear stress τ here) there will be an increase in effective load due to area reduction and a decrease in applied load due to spring unloading with displacement. The magnitude of these two contributions changes with displacement. In a simple case where steady-state load is fixed (constant axial stress):

$$K_{d\tau,ds} = \frac{d\tau_{spring}}{ds} = \frac{d\tau}{dF}\frac{dF}{dx}\frac{dx}{d\delta}\frac{d\delta}{ds} = K_{ax} * \frac{\sin 2\psi}{2}\cos\psi\frac{d_0}{\sin\psi} \tag{3.74}$$

$$K_{d\tau,ds,fault} = K_{d\tau,ds}/f(s) \tag{3.75}$$

$$\tau_{fault} = \tau_{ss}/f(s) \tag{3.76}$$

$$\frac{d\tau_{fault}}{ds} = \tau_{ss} * \frac{-1}{f^2}\frac{df}{ds} \tag{3.77}$$

$$K_{obs} = -K_{d\tau,ds,fault} + \frac{d\tau_{fault}}{ds} \tag{3.78}$$

These two terms have opposite signs (a stress decrease and increase, respectively) so they compete to control stability vs. fault displacement. Fixed variables are spring stiffness, fault length, fault angle, and σ_3. Note that long faults are inherently more stable here ($d_0/\sin\psi$, equation 3.74). Also note how the effective fault stiffness is affected by current load in the latter set of equations τ_{ss}. This dependence on current load will cause slipping faults to stabilize if stiffness is high.

For the particular case of relaxation, stress evolves as:

$$\tau_{\sigma_1}(s) = \tau_{\sigma_1,ss} - K_{d\tau,ds} * (s - s_{ss}) \tag{3.79}$$

These quantities are all conversions from axial stress and directly related to axial stress at constant confining pressure. To incorporate area change on the fault we again calculate the 'effective'/'real' shear stress for the reduced area as a function:

$$\tau_{fault} = \tau_{\sigma_1}(s)/f(s) \tag{3.80}$$

We then take the derivative with respect to s and use the product rule to find:

$$\frac{d\tau_{fault}}{ds}(s) = \tau_{\sigma_1}(s) * \frac{-1}{f^2}\frac{df}{ds} - K_{d\tau,ds}/f(s) \tag{3.81}$$

Many cases are more stable than constant stress because spring/applied stress decreases at large displacement.

Chapter 4

A Low Cost Fiber-Optic Displacement Sensor Designed For Use at High Pressure

Eric Burdette and Greg Hirth

[1]Department of Earth, Environmental and Planetary Sciences, Brown University, Providence, RI, USA

Key Points:

- Seal friction limits stress resolution in high pressure deformation experiments. Internal load measurement resolves this limitation.
- The cell operates by measuring displacement of an elastic cavity. It is compact and can survive temperatures up to 700°C
- Implementation is simple, requiring at minimum a PC, 96kHz sound card, telecom modulated DFB laser, and a photodiode.

Abstract

Deforming rocks presents a particularly challenging test environment. Not only are required temperatures often above 300°C, but pressures above 200 MPa are commonly required to replicate conditions in the earth. The machines (e.g. Paterson-type, Griggs-type, D-DIA, Oxford Creep Rig, etc.) designed to apply these pressures and temperatures require measurement compromises and exotic materials to accommodate common, reliable sensors. Each of these machines has a furnace which can reach 1200°C at its center, often inside a pressure vessel. Common sensors like LVDTs and strain gauges cannot survive this temperature and are placed either outside the pressure vessel, or far from the furnace with ceramic or steel connecting rods/pistons. This can introduce prohibitively large error into measurements of low stresses and specimen deformation rates sometimes as low as 1 μm/day, especially when friction is included. These applications would benefit from inclusion of a simple, compact, low cost displacement sensor with resolution better than 1 μm, which is achievable using an interferometer constructed with standard telecom fiber optic components. We have adapted designs for external cavity Fabry-Perot interferometer to build a high accuracy (2 nm, 0.1 MPa) displacement/load sensor using standard telecom fiber/lasers and a disposable sensing head. The total equipment cost is less than $5000. The design was tested inside a Griggs pressure vessel to measure loads at 700°C. A benefit of using telecom equipment is very large bandwidth. Using an FPGA for digital signal processing, bandwidth can easily reach 100 kHz, measuring speeds up to 0.02 m/s. A small modification of the light path allows a vibrometer to be constructed, unlocking significantly higher displacement rates/bandwidth (7.75 m/s, 10 MHz).

4.1 Introduction

Fiber optics allow direct measurement of sub-nanometer distances at extreme conditions which would otherwise be inaccessible to mechanical sensors like LVDTs. Other advantages include immunity in electrical interference and no requirement of additional mass. However, fiber optics lack the simplicity, reliability, and familiarity of electrical and magnetic displacement sensors. As a result laser displacement sensors are typically only found in exotic equipment at unusually low temperature, high speed, or high precision. A familiar example is the reflected red diode laser and detector used to measure position of atomic force microscopes.

Rock deformation presents a particularly challenging measurement environment. Not only are specimen temperatures often above 300°C, but pressure above 200 MPa is commonly required to replicate conditions in the earth. The machines (e.g. Paterson-type, Griggs-type, D-DIA, Oxford Creep Rig, etc.) designed to apply these pressures and temperatures require measurement compromises to accommodate common, reliable sensors. Each of these machines has a furnace which can reach 1200°C at its center, often inside a pressure vessel. Common sensors like LVDTs and strain gauges cannot survive this temperature and are placed either outside the pressure vessel, or far from the furnace with ceramic or steel connecting rods/pistons. These compromises can introduce unacceptable error into measurements of low stresses and specimen strain rates that approach 1μm/day, especially when uncertainty due to friction is included. These applications would benefit from inclusion of a simple, compact, low cost displacement sensor with resolution better than 1μm, which is achievable using an interferometer constructed with standard telecom fiber optic components.

Mass production of diode lasers has driven down cost to the point that a fiber-coupled, temperature stabilized laser diode system can be purchased for $2000, while telecom fiber and detection equipment can be purchased for less than $1000. Modulation, demodulation, and processing of laser intensity can be driven with common PC sound card equipment, bringing total cost to less than $5000.

Two interferometer types stand out for application to our displacement applications: Mach-Zender and Fabry-Perot. Designs for Mach-Zender interferometers are already common in free space laser-doppler vibrometers which could be fiber-coupled. Fabry-Perot designs are also common for strain/pressure sensing, and commercial fiber-coupled versions can be purchased for $25,000. We describe a simpler version using laser intensity modulation.

An external cavity Fabry-Perot interferometer (EFPI) modulates reflected/transmitted intensity due to mutual interference between standing waves established in a cavity with partially reflecting mirrors. The simple design which we use is outlined by Nowakowski et al. (2016). The

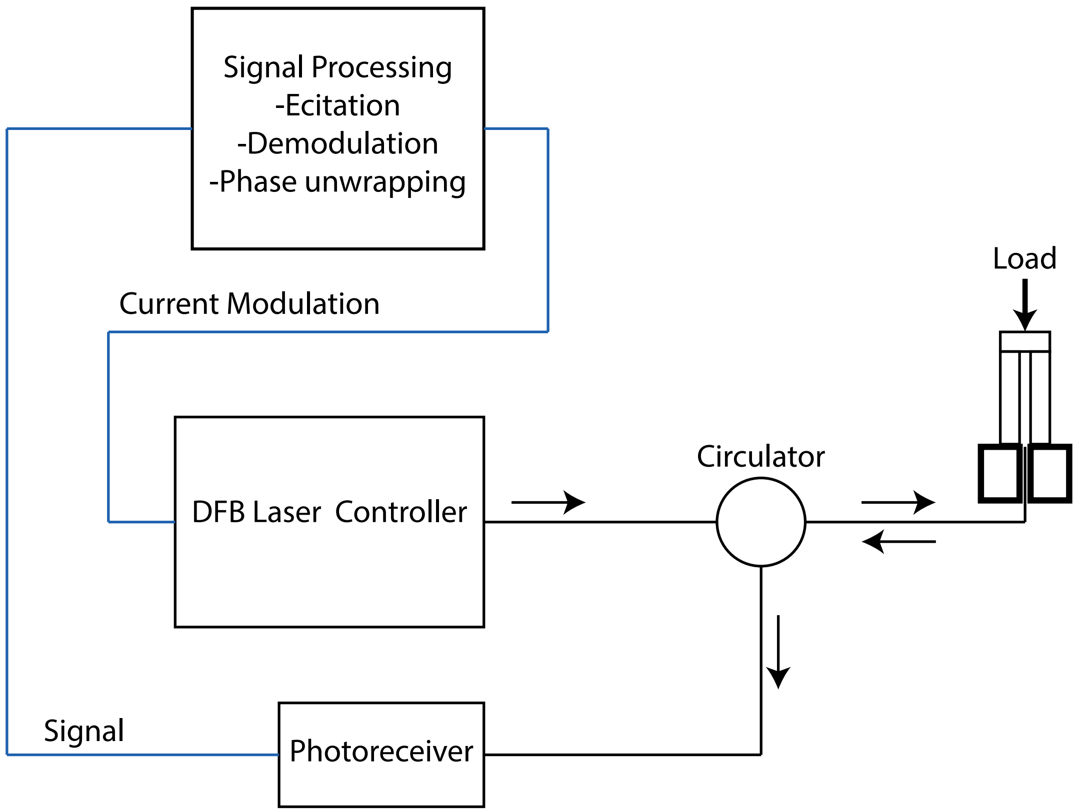

Figure 4.1: Schematic of elements required for this EFPI (External cavity Fabry-Perot Interferometer) system to measure load.

equation for intensity returning from the cavity is:

$$\frac{I_{refl}}{I_{inc}} = \frac{(1+R)^2}{2}\frac{1-\cos\frac{4\pi}{\lambda}h}{1+R^2-2R\cos\frac{4\pi}{\lambda}h} \tag{4.1}$$

where I is incident and reflected intensity, R is reflectance of the cavity surfaces, h is cavity length, and λ is laser wavelength. Note that intensity changes with both cavity length and wavelength on a period of half the incident wavelength.

Nowakowski et al. (2016) use a tunable wavelength laser (±25 nm) to oscillate wavelength at frequency f, and recover the reflected direct cavity response slope at f, while also recovering the curvature of the cavity response at frequency 2f. These signals are 90 degrees out of phase, so they can be separately demodulated and fed into an arctangent function to recover the phase of the cavity response, which is directly related to half the incident wavelength (See Kirkendall and Dandridge, 2004). A system using a 1550 nm laser with 10 bit phase accuracy can measure a 1 nm cavity length change over a range of several centimeters.

4.2 Sensor Design and Machine Integration

4.2.1 Interferometer System

A schematic of the EFPI implementation is presented in Figure 4.1. The system is comprised of a DFB laser controller (Koheron CTL200 with a QPhotonics qdfbld-1550-5), 2:1 FBT coupler, Fabry-Perot cavity (simplest form is a polished reflector and FC coupler terminated fiber), fiber coupled photodiode reciever (TTI TIA-950), and a digital-to analog/analog-to-digital converter on the same clock source with a signal processor (Digilent Eclypse Z7 FPGA or PC + sound card). A simple single frequency, current modulating laser is used instead of a tunable laser used by Nowakowski et al. (2016). The intensity and wavelength of the single-frequency laser changes with current. The wavelength-current coefficient is approximately 10 pm/mA, so the effective ±25 mA modulation depth of the laser is enough to interrogate cavities greater than 5 mm long (Nowakowski et al., 2016).

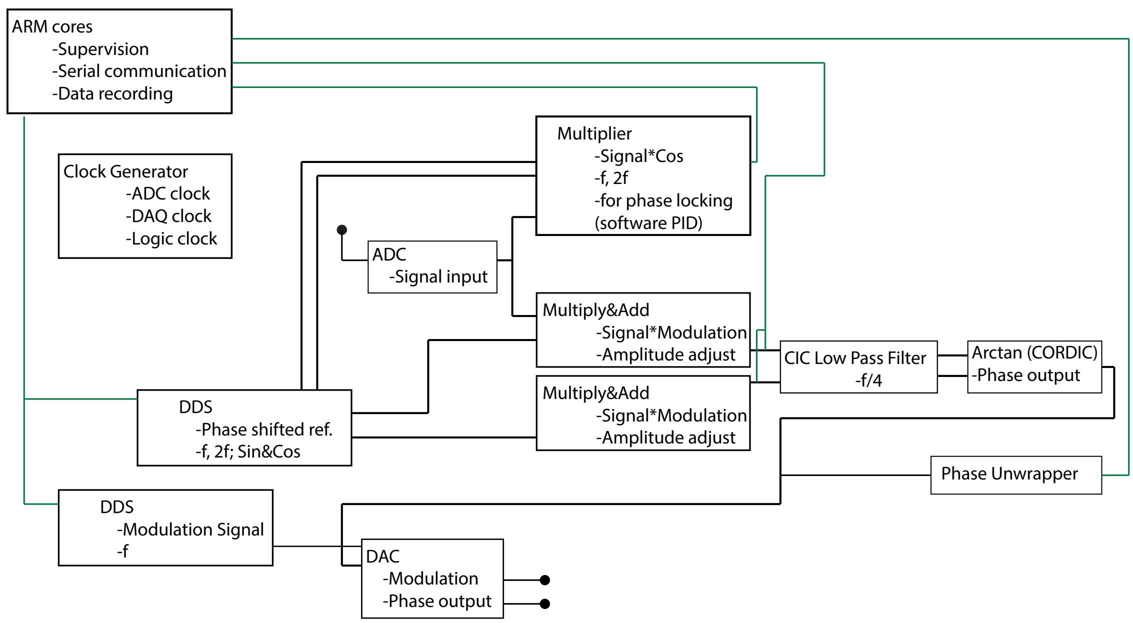

Figure 4.2: Schematic of the EFPI (External cavity Fabry-Perot Interferometer) modulation and demodulation system implemented on a Digilent Eclypse Z7 FPGA.

Processing of the cavity length can be performed in realtime by a PC or FPGA with the scheme illustrated in Figure 4.2. Maximum tracking speed at 6 kHz modulation frequency (for a PC sound card sampling at 96kHz) is 2 mm/s, while maximum tracking speed at 1.5 MHz modulation frequency is 300 mm/s. Bandwidth is limited by filtering to 3 kHz and 400 kHz respectively.

Because the amplitude of the 2f cavity response produced by current/wavelength modulation is a secondary effect, its amplitude is always lower than that of the fundamental modulation frequency. This leads to a slightly acircular path when the two components are plotted against each other (Figure 4.3) which can be corrected at system startup (e.g. Nowakowski et al., 2016).

4.2.2 Bench Testing

Simple Bench tests were performed to demonstrate simple applications of the displacement sensing capability. A polished fiber was aimed at a reflector attached to either a piezoelectric actuator, a speaker cone, or a micrometer. The piezoelectric actuator (Physik Instrumente PI-840.30) was driven in both a triangle wave and square wave configuration. Results of the triangle wave driving are plotted in figure 4.4. Surprisingly, the records reveal frictional hysteresis during unloading (similar to the behavior of the spring system of Burdette and Hirth (2020)). The step response of the actuator is limited to approximately 1kHz by the amplification system, and is displayed in figure 4.5. The sensor resonance is reported to be 10kHz (which is above the amplifier response), so there is no observed resonant ringing associated with the step. The largest measured speed of the actuator is 8 $nm/\mu s$ (8 mm/s).

4.2.3 Implementation to Measure Internal Axial Stress in a Griggs-Type Apparatus

Figure 4.6 shows how a cavity can be introduced into the loading column of a Griggs-type rock deformation apparatus. Fiber is fed up a hole in the central column and glued into the base carbide. An EFPI cavity is formed by placing an alumina tube on top of the base carbide, with a polished carbide reflector at its end, below the sample to be deformed. A 10mm alumina tube with an elastic

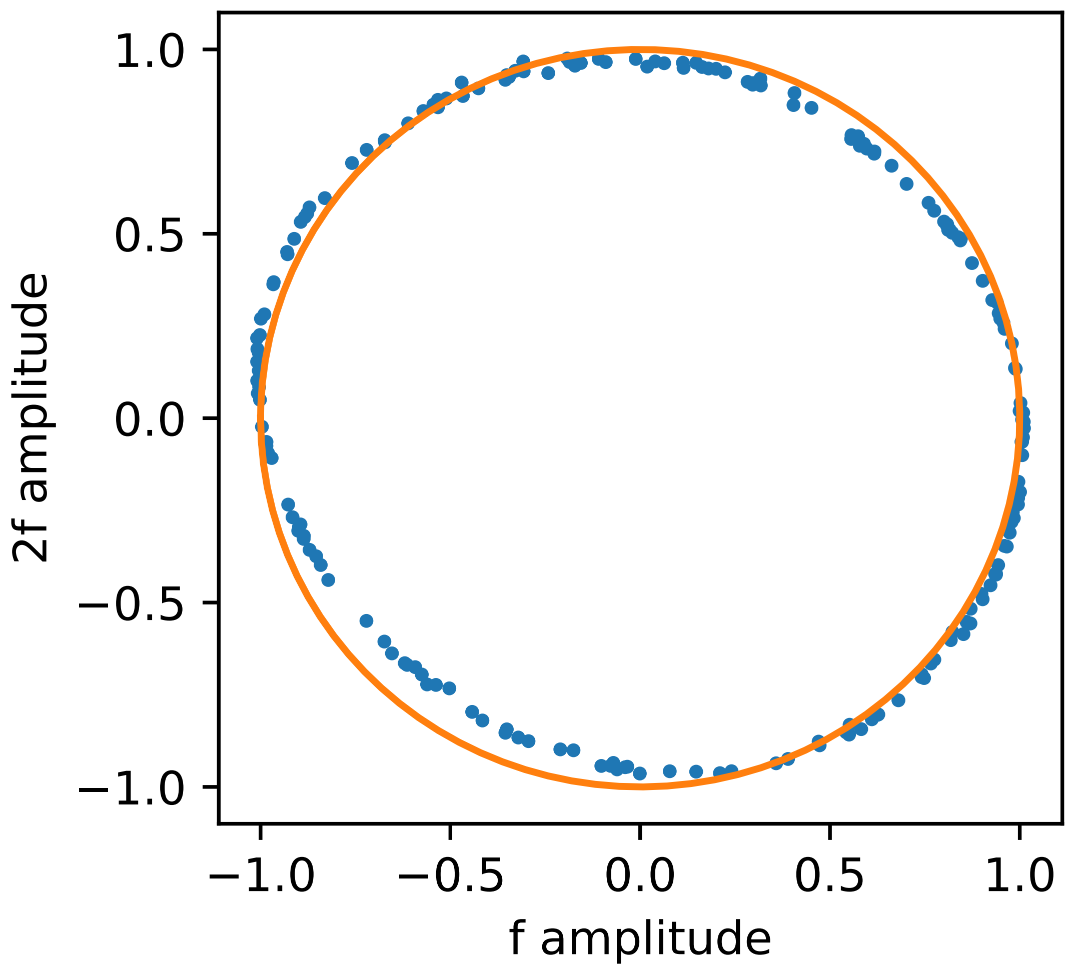

Figure 4.3: Plot of recorded amplitudes at the carrier frequency against two times the carrier frequency returning from the Fabry-Perot cavity during movement of a reflector attached to a piezoelectric actuator. Data are blue points. A reference unit circle is plotted in orange.

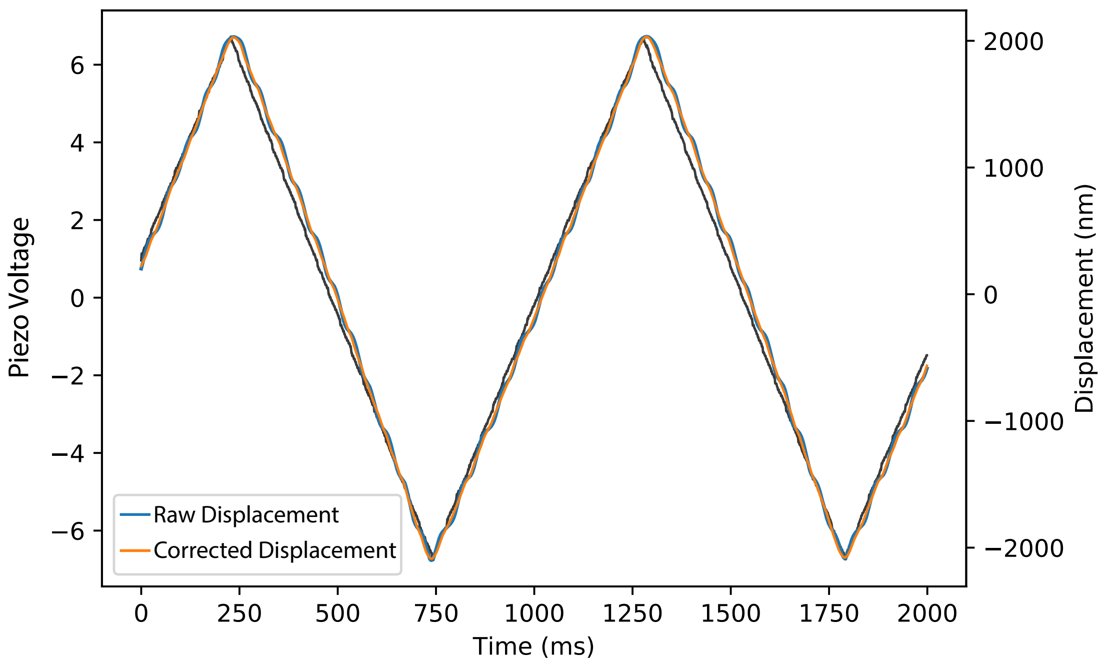

Figure 4.4: Displacement of a reflector attached to a piezoelectric actuator measured by the EFPI system. Differences while displacement decreases are due to frictional hysteresis.

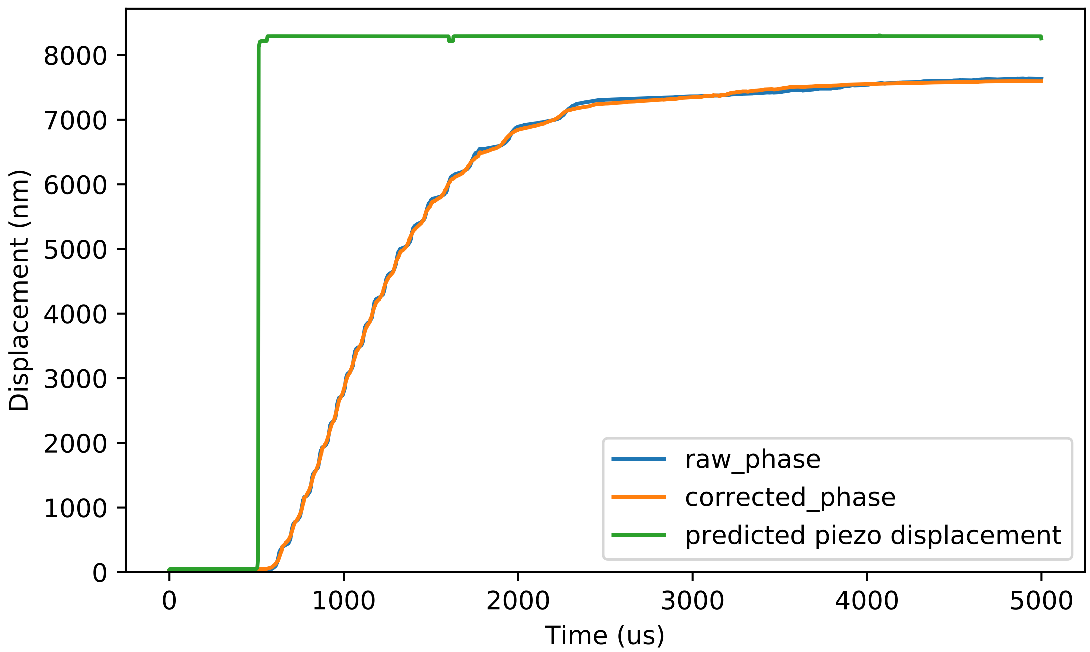

Figure 4.5: Plot of step response of the piezoelectric actuator and its amplifier to an instantaneous command voltage change. Command voltage to amplifier input is plotted in green (step). Raw and processed records of the phase output of the EFPI system are plotted in blue and green, respectively. Note that actual amplifier output response is somewhat slower than the expected step because high power is required to charge the capacitive piezo elements.

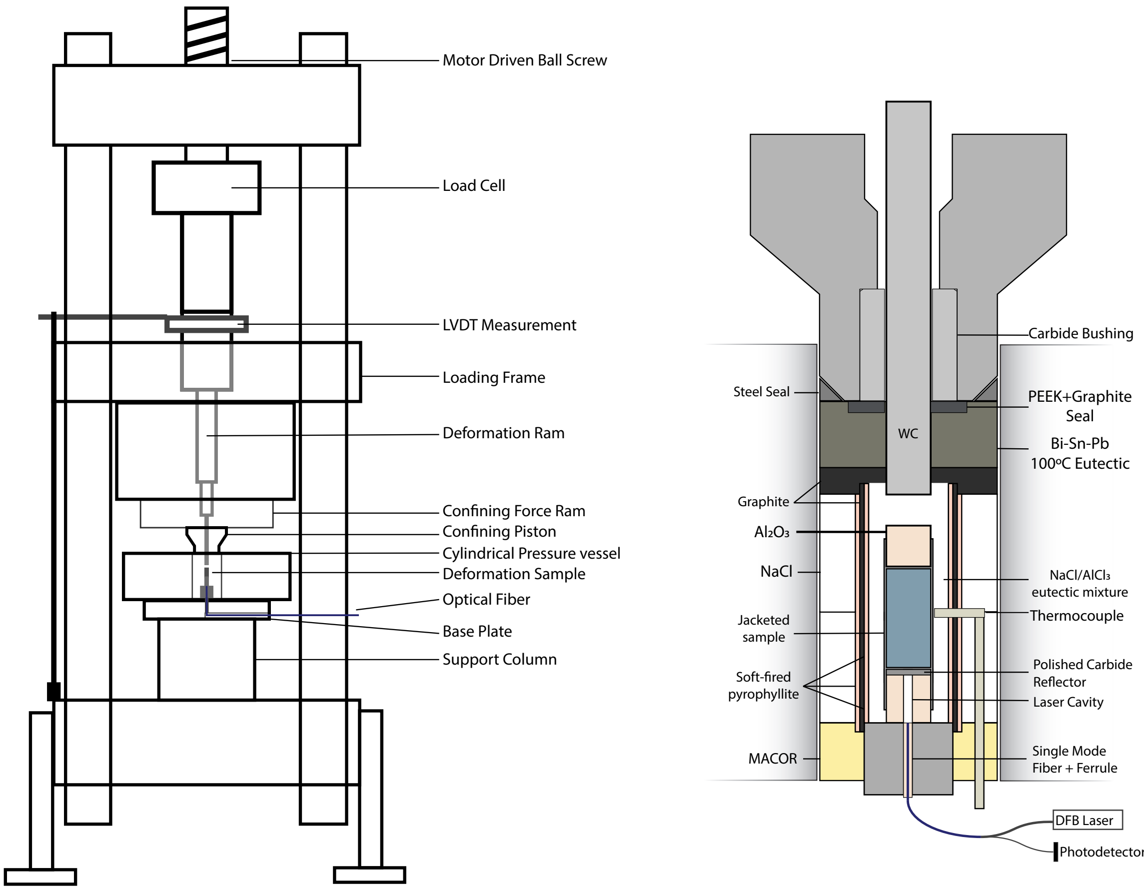

Figure 4.6: Schematic of implementation of the EFPI as a load cell in a Griggs-type high pressure deformation apparatus.

modulus of 400 GPa will change length by 25 nm for a 1 MPa stress change, which is well within the detection capabilities of the EFPI system.

A similar design was built by Blacic and Hagman (1977) with excellent sensitivity. Our design improves on their implementation by: improving immunity to pressure changes, improving immunity to vibration, and constructing the cavity from simple, inexpensive replaceable parts. The wide machined carbide pedestal of Blacic and Hagman (1977) has an axial area exposed to confining media which applies axial shortening force 3x the axial deformation force. Thus, small changes in pressure result in large cavity displacements that are indistinguishable from sample deformation loading. The cavity we implemented has the same diameter as the sample, so pressure changes can only affect its length through the Poisson effect. We improve noise immunity by using a terminated fiber glued directly underneath the cavity to avoid external vibration influences. Blacic and Hagman (1977)'s cavity was 14.6 cm including a significant amount of metal that changes size with total apparatus load/vibration and changes in room temperature. Finally, the fiber ferrule, alumina tube, and polished carbide are standard parts from materials suppliers (McMaster-Carr, Thorlabs), while the carbide is EDM drilled after purchase. After use, glue is burned out of the base carbide and ferrule at 400°C, and another is inserted and glued in for the next use.

4.3 Results

4.3.1 Mechanical Results

For calibration, 1/4" cylinders of 360 grade brass were purchased from McMaster-Carr and deformed with the Griggs-type appratus inside a pressure vessel filled with melted paraffin wax at 150 MPa confining pressure. The lower portion of the loading column is jacketed in polyolefin to prevent wax from intruding in between column elements. A gap is left between the top piston and an externally connected piston so that the sample and lower column do not interact with the external piston until it is advanced after pressurization.

Results from our traditional external load measurement and the new internal load cell

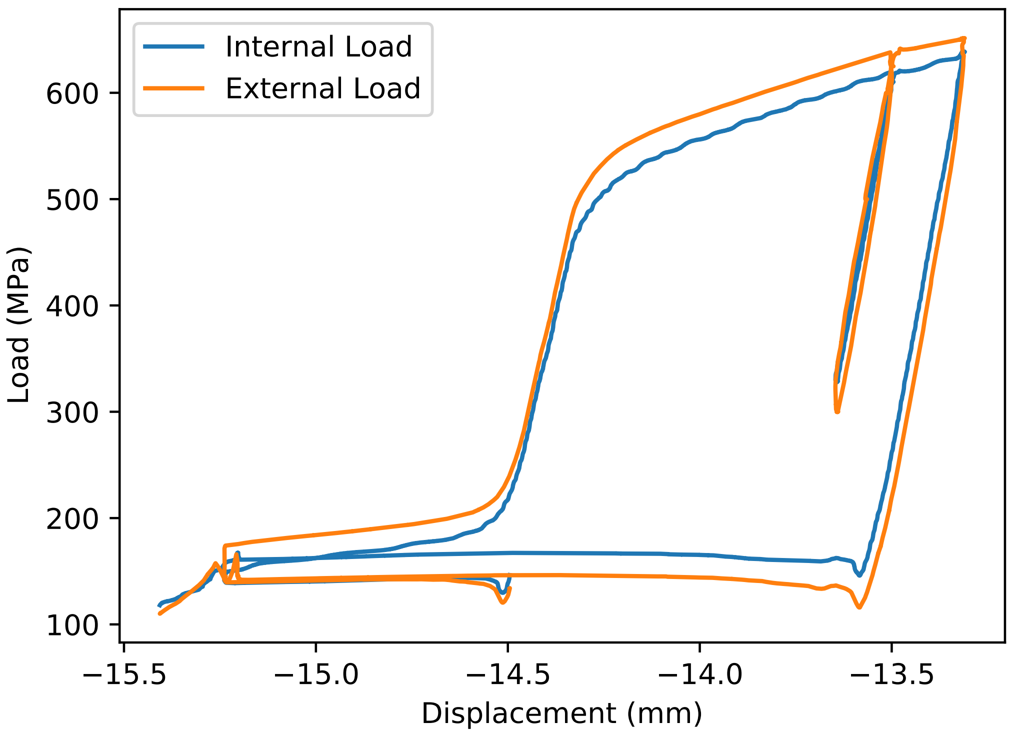

Figure 4.7: Plot of load and external displacement records from an experiment deforming a 360 grade brass sample.

are plotted against externally measured piston displacement (Figure 4.7). When the externally connected piston is out of contact with the sample, internal load does not change regardless of which direction the piston is moving. While the piston is in contact with the column, deforming the sample, there is a static, direction dependent offset as would be expected for frictional hysteresis due to the seals.

4.4 Conclusions

1. We designed and tested an EFPI load sensor for high confining pressure deformation.
2. Designs for the sensor are published here and can be replicated at low cost.
3. Tests of pressure show the sensor has precision that meets or exceeds current requirements.
4. The technology also can be used for high speed/precision displacement sensing during creep of brittle rocks.

Acknowledgments

We would like to thank Steve Kidder for purchasing the initial DFB laser controller. We would also like to thank Doug T. Smith at NIST for his helpful advice when attempting to replicate designs from Nowakowski et al. (2016).

4.5 Supporting Information

4.5.1 Temperature Sweep Displacement Tracking

With the same components, a laser die temperature sweep can change wavelength by more than a nanometer to cross several fringes of the Fabry-Perot cavity. The approach is slow, requiring 8 seconds for a single wavelength scan cycle, but it allows calculation of the absolute cavity length. Figure 4.8 shows scans at 10 MPa and 50 MPa. Fringe spacing changes slightly, by a factor of $\Delta\sigma/E$. The position of the fringes, or alternatively the wavelength spectra of the cavity, is recorded over time and displayed in Figure 4.9, along with the modelplots of equation 4.1 considering displacement on the loaded 10 mm alumina elastic element and temperature dependent wavelength.

4.5.2 Vibrometer Modifications

A vibrometer can easily be incorporated into the design of the interferometer if optocouplers and another leg (e.g. fiber) are added to mix returning light with the incident, modulated signal. The sensor face needs and anti-reflective coating to avoid Fabry-Perot effects. I-Q demodulation can be used to track the position of the reflector to higher speeds.

4.5.3 Use at High Temperature

High temperature deformation in a Griggs-type apparatus is a challenging environment, with sample temperatures up to 1200°C less than 2 cm from the exterior of the pressure vessel. Existing pressure vessel and assembly design choices are mostly a legacy from eras when numerical modeling was inaccessible, which has made some thermal problems intractable to solve. To insert the ferrule 1 cm from the hot sample requires adequate water cooling close to the sample to keep temperatures below fiber epoxy temperature limits of 100°C. Adding cooling tubes/channels sacrifices metal required to support the sample and pressure vessel. To explore the design space we developed a 2D axisymmetric thermal model published in Moarefvand et al (2021), and modified it to include a 'baseplate' supporting the pressure vessel, with heat transfer coefficient boundary conditions to water representing our actual cooling conditions rather than the simplified fixed temperature

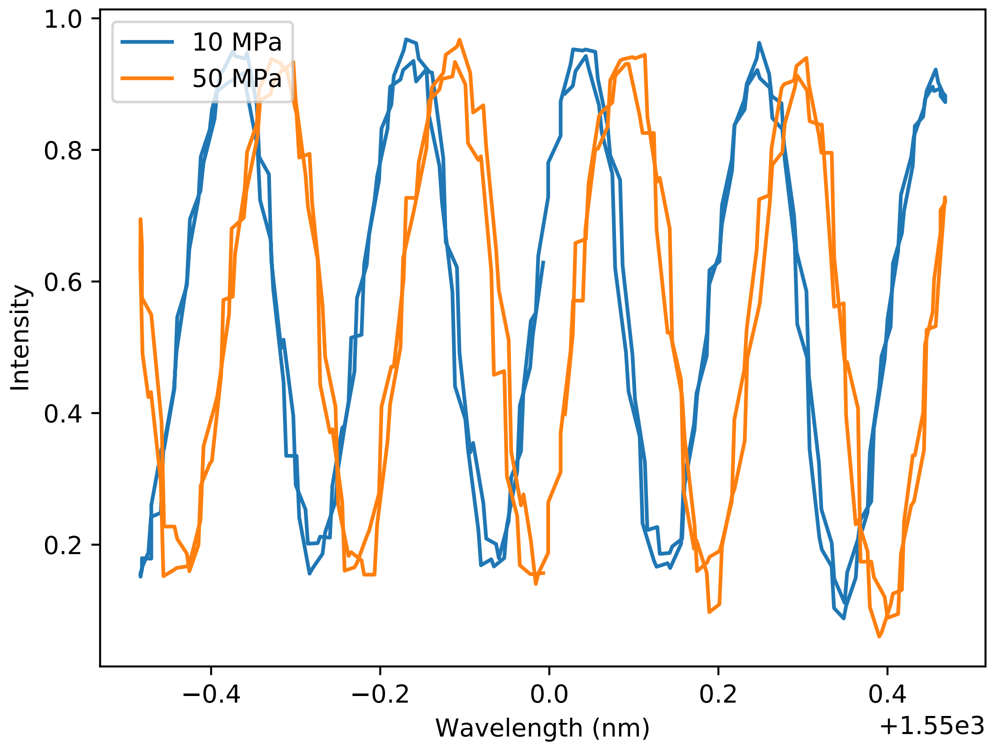

Figure 4.8: Data from an unconfined elastic loading experiment. Scans were taken at 10 MPa and 50 MPa axial loads.

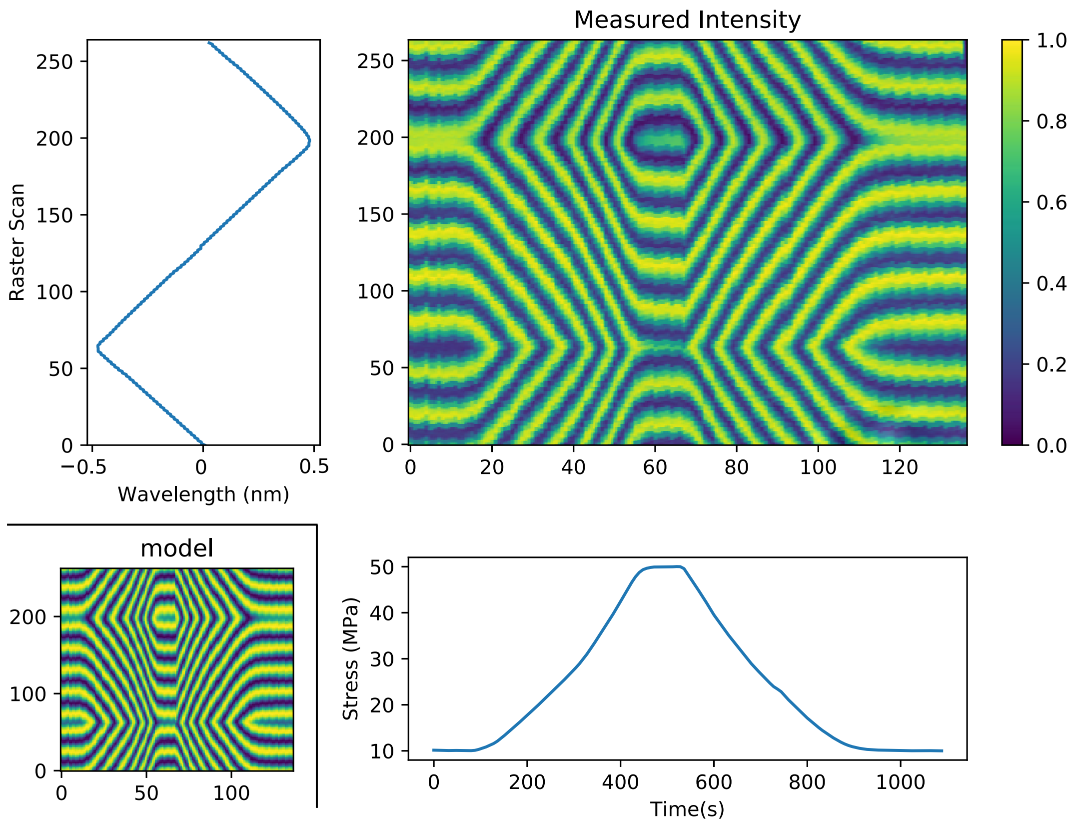

Figure 4.9: Plots of temperature scans recorded during a ramp in load. Fringes pass in the horizontal (x, time) direction for a given wavelength (y) as they would for the direct (frequency f) amplitude in the current modulated design.

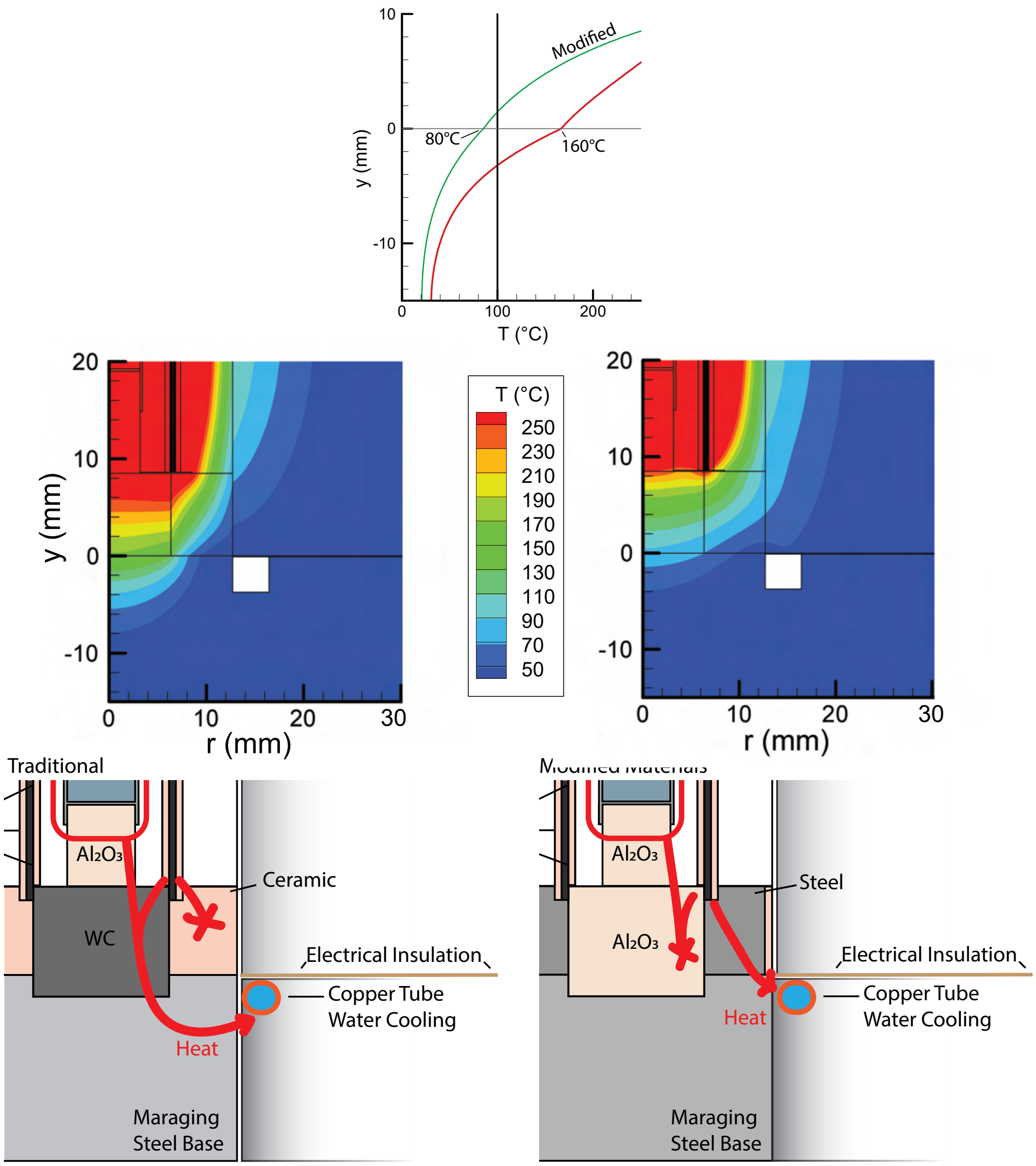

Figure 4.10: Thermal model comparing an assembly with ceramic outer pieces to a modified assembly with material changes. Temperatures at the surface of the baseplate drop by 80°C, allowing a feasible implementation of a glued Fabry-Perot cavity.

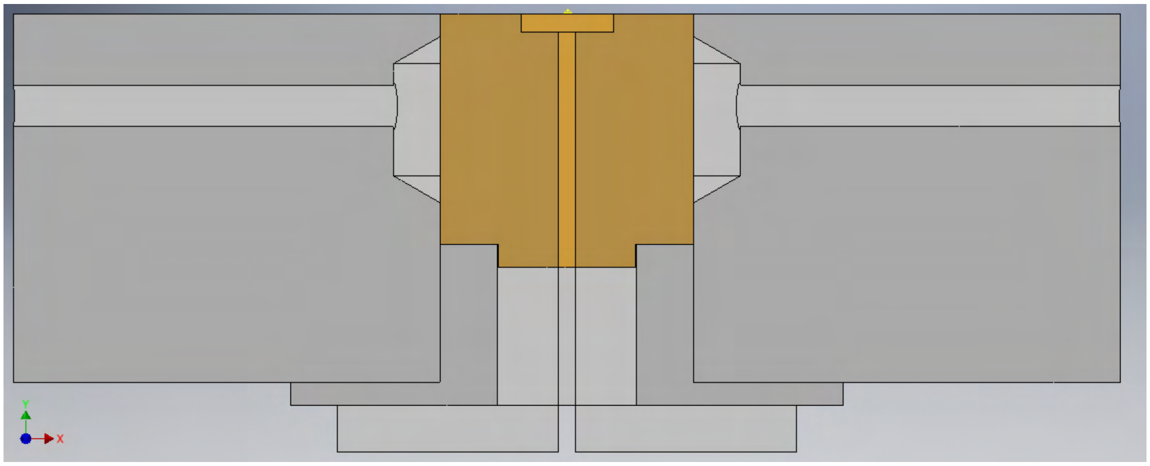

Figure 4.11: Cross section of re-designed baseplate.

commonly used. We find that:

1. Assembly material thermal conductivity (inside the pressure vessel) has a large effect on required power, and governs pressure vessel inner wall temperature. Changing from sodium chloride to potassium bromide confining media would decrease thermal conductivity by a factor of two and reduce vessel temperatures from 180°C to 100°C at 700°C sample temperatures.

2. Current water cooling is inadequate below the pressure vessel. While water channels on top of the pressure vessel have a 1" ID and 3" OD with a 1/4" height, cooling in the baseplate is provided by a single 1/8"ID, 1/4" OD copper tube. This leads to high temperatures extending below the sample, with the baseplate reaching 160°C at 700°C sample temperatures.

3. Current materials conduct along the central axis (tungsten carbide), and insulate near the pressure vessel walls (pyrophyllite) where the water cooling is placed (see model). This leads to heat flowing downward into the baseplate, and then outward towards water cooling which further increases temperatures in the base carbide where the ferrule is placed. This can be swapped, putting steel near the vessel, and using a central pillar of zirconia or alumina (Figure 4.10. Several european groups modified their assemblies to this design (Rybacki et al., 1998) but do not note this benefit.

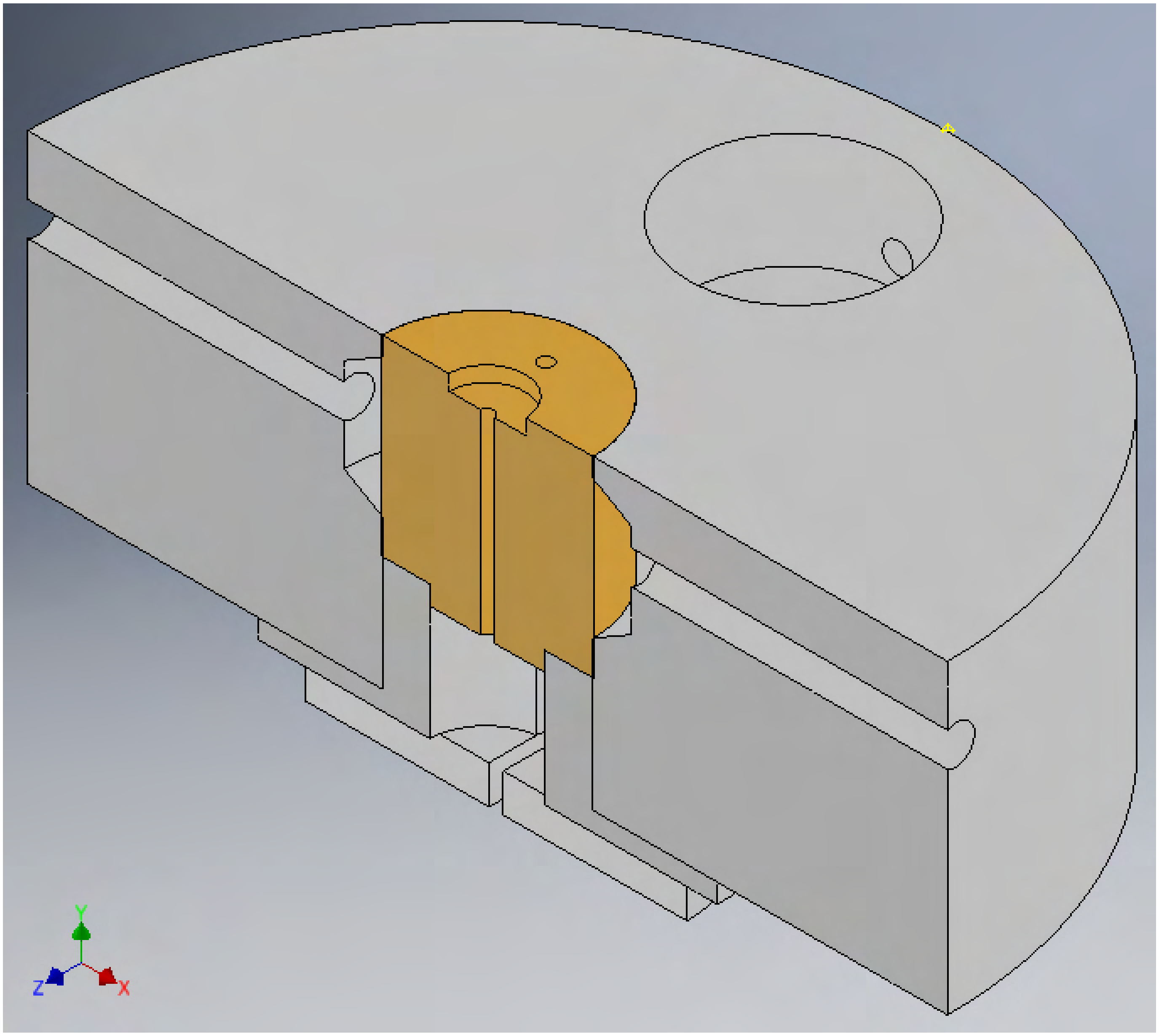

Figure 4.12: Orthogonal view of re-designed baseplate.

In addition to the planned changes to the salt used for confining media and changes to the lower insulating material, we redesigned a baseplate to incorporate large water channels and a high conductivity beryllium copper support core (Figure 4.11, 4.12). We took the opportunity to add an axisymmetric cavity at the bottom of the support post to incorporate acoustic emission sensors.

Appendix A

Setting up Dehydration Earthquakes in Dehydrating Antigorite: Grain Alignment (CPO) and Damage Controls Permeability and Fracture Toughness

Eric Burdette and Greg Hirth

[1]Department of Earth, Environmental and Planetary Sciences, Brown University, Providence, RI, USA

Key Points:

- Antigorite was deformed at two loading rates and subsequently dehydrated
- Dynamic rupture can be produced with slow (10^{-5}) loading and dehydration before samples reach peak strength.

A.1 Introduction

Subduction zones are among the most seismically active areas on earth. The wide spectrum of brittle and ductile behavior in the nearby mantle and downgoing slab control seismic coupling, deep fluid transport, and mantle convection. The interplay between rheology and metamorphic reactions is key to understanding tectonic dynamics and evolution at depth.

Slabs descending into the mantle carry chemically bound liquids in the form of hydrous minerals. Antigorite is an abundant and efficient mineral in the slab to carry this water. Heating of the slab at depth along the geothermal gradient causes dehydration (Hacker et al., 2003). The subsequent water release is hypothesized to: cause dehydration melting that generates arc volcanism, act as a mechanism for decoupling of the downgoing slab to the convecting mantle, and be the source for intermediate depth seismicity. The seismicity is thought to be due to reaction generated pore fluid pressure and velocity feedback on strength in the material (Raleigh and Paterson, 1965; Okazaki and Hirth, 2016), but this remains poorly established experimentally at relevant pressures.

Several studies at low pressure have shown that antigorite can generate unstable dynamic rupture when deformed at pressure below 500 MPa (Raleigh and Paterson, 1965; Murrell and Ismail, 1976; Reinen et al., 1994; Okazaki and Katayama, 2015). However, studies attempting to replicate the unstable behavior at pressure above 500 MPa have not produced acoustic emissions or dynamic rupture (Hilairet et al., 2007; Chernak and Hirth, 2010, 2011; Proctor and Hirth, 2015; Ferrand et al., 2017) even when stiffness was reduced by an order of magnitude, which strongly enhances shear weakening and activates shear heating, but slip rates only reach 40 um/s (Burdette and Hirth (2020)). Why is this?

Several recent studies focus on ’plastic’ deformation mechanisms that allow antigorite to deform without increasing its volume (Escartin et al. (1997); David et al. (2020)). This non-dilatant

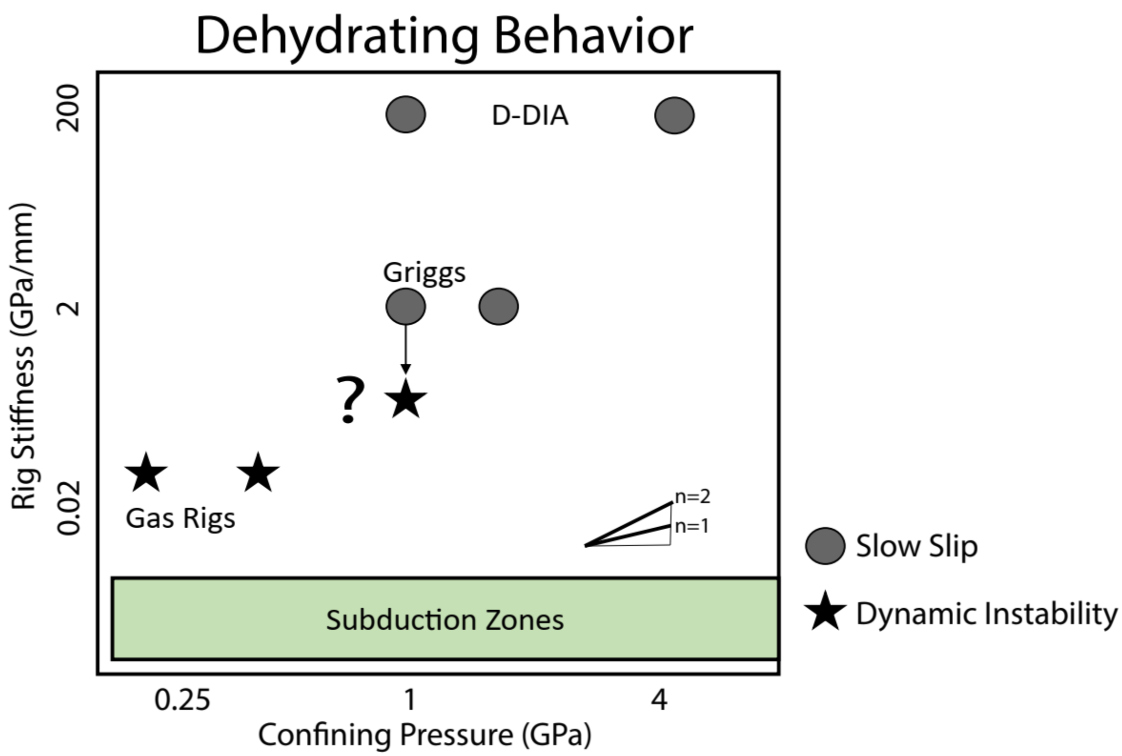

Figure A.1: Confining pressure and corresponding apparatus stiffness for studies of antigorite dehydration mechanical behavior. D-DIA studies referenced are Hilairet et al. (2007) and Gasc et al. (2011). Griggs apparatus studies referenced are Chernak and Hirth (2011), Proctor and Hirth (2015), and Okazaki and Hirth (2016). Gas Rig experiments referenced are Okazaki and Katayama (2015) and Murrell and Ismail (1976).

deformation is characterized by distributed shear sliding on mode 2 cracks whose displacement is limited by grain boundaries with sheets of a different orientation. Data from chapter 2 shows displacement along the shear cracks at grain boundaries leads to kinking of the neighboring grain, and can tear it at high strain, generating gouge. In synchrotron studies (Hilairet et al. (2007)), tearing may be the primary deformation mechanism, amorphising more than 40% of the sample (Amiguet et al., 2014, figure 6). Low strain, and low strainrate experiments above 400°C (Figure 2.3) show less microcrack damage, as outlined in Chapter 2.

The contrast in CPO and damage between high and low strain rate experiments sheds light on several unpublished results at low strain rate from our previous investigations gathered here. We were able to produce a dynamic earthquake-like slip event by slowly loading a gouge sample, and increasing temperature to dehydrate it before reaching peak stress. We were also able to produce more rapid slip by deforming a sample that was loaded quickly, and dehydrated at lower stress before significant plastic deformation occurred (in contrast to peak stress dehydration). A constant stress creep sample which produced a small, but dynamic slip event at conditions slightly above antigorite's dehydration temperature illustrates the development of an unstable fault moving through samples.

A.2 Methods

Methods for material preparation and protocols for temperature ramping dehydration experiments are detailed in chapter 1. Methods for material preparation and protocols for stress stepping experiments on solid antigorite cores are detailed in chapter 2. All experiments in this section were conducted at 1 GPa confining pressure and used the modified compliance column Burdette and Hirth (2020).

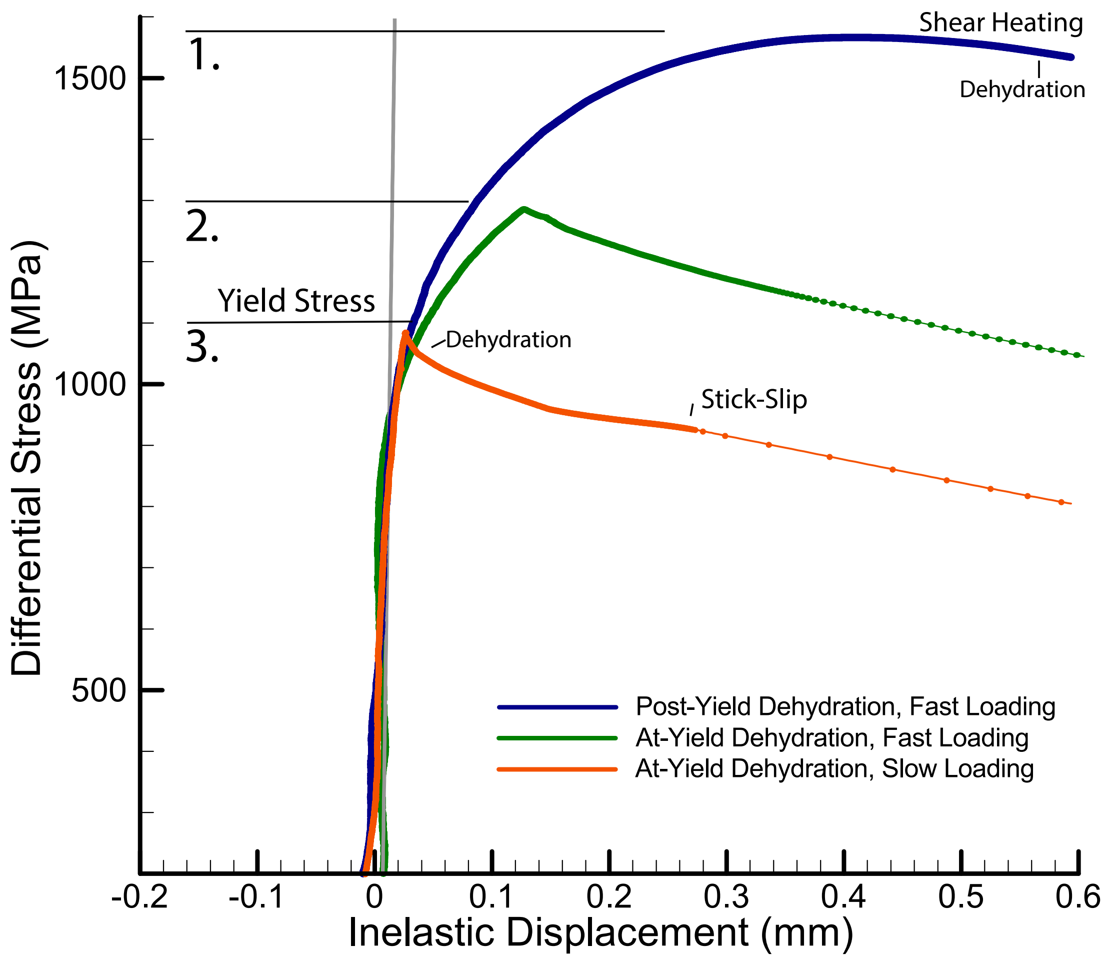

Figure A.2: Differential stress and sample displacement are shown for three dehydration experiments at 1 GPa confining pressure. The first is and experiment from previous work that was allowed to reach peak stress (”Shear Heating”) before dehydrating loaded ’Fast’ ($10^{-4}1/s$), The second is and experiment loaded ’Fast’, but dehydrated before reaching peak stress, and the third is an experiment loaded ”slowly” ($10^{-5}1/s$) and also dehydrated before reaching yield (”Stick-Slip”). Labels indicate time of dehydration. Numbered stress levels indicate peak stress for each experiment. Points are plotted at 1 Hz recording rate

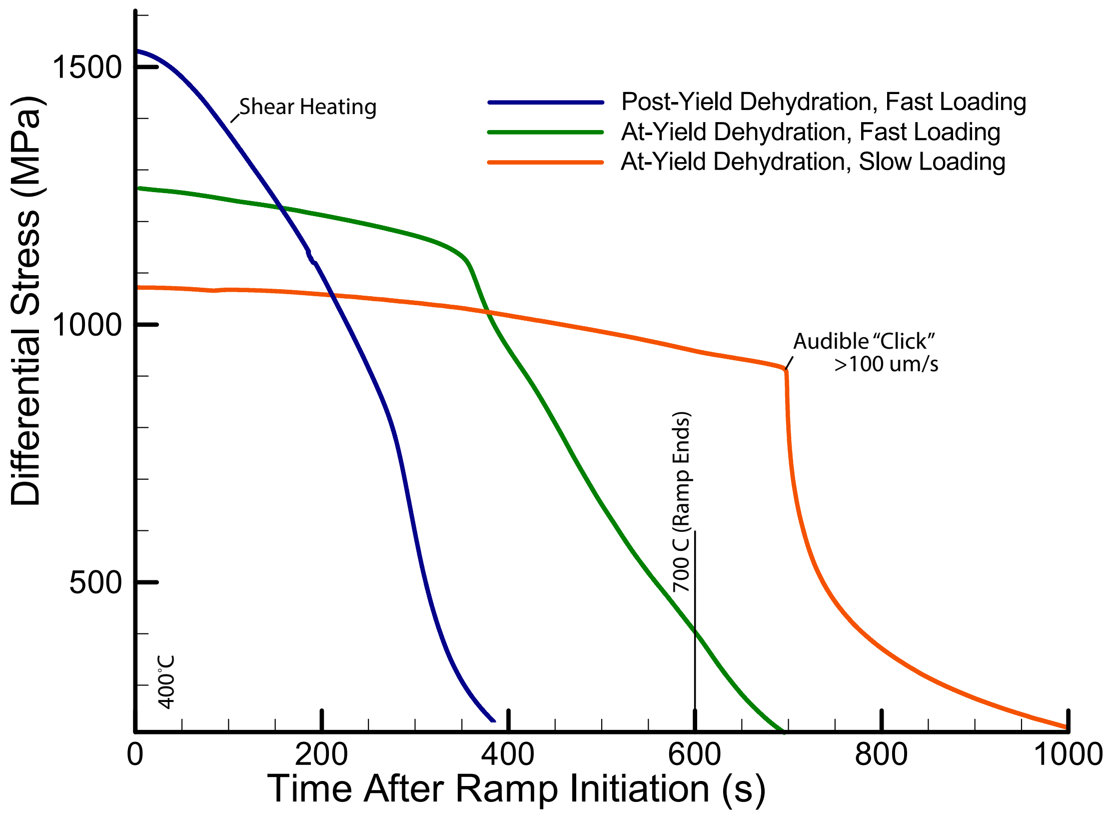

Figure A.3: Load-time data from shear heating (post-yield dehydration), and preliminary stick-slip runs (pre-yield dehydration). Temperature was ramped from 400 ^{o}C to 700 ^{o}C over 600 seconds to initiate dehydration. Sample displacement speed is noted for the pre-yield run at the time when stick-slip occurred.

A.3 Results

A.3.1 Mechanical Data

Mechanical data were collected for several dehydration experiments at 1 GPa, where the loading displacement rate and the strain at which dehydration was initiated were varied (figure A.3, figure A.2). Results of dehydration at peak stress with ”fast” (1.8 µm/s) loading are discussed in detail in chapter 1. The dehydration reaction along the fault zone completes in 400 seconds, before the imposed temperature reaches 700°C, and peak displacement rate is 40 µm/s. The displacement during dehydration is very large (10 mm) which activates shear heating.

An intermediate experiment, where the sample was dehydrated before reaching peak stress with ”fast” loading, is also displayed in figure A.2. It weakens more slowly, finishing around the 600 second time when the furnace reaches 700°C. Its peak displacement rate is 15 µm/s, and shows no signs of stick-slip activity.

In a third experiment, samples were loaded ”slowly” (0.18 µm/s) and dehydrated before yield. The sample does not weaken substantially during the ramp of imposed temperature to 700°C. Shortly after reaching 700°C, the samples slip rapidly at speeds greater than 100 µm/s, and weakens 500 MPa in 50 seconds.

Stress-stepping creep data for the dehydrating antigorite creep are discussed in section 2.7. After 7 hours at temperature (620°C), a small stick-slip event occurred, generating a fault running partway through the sample. Only two subsequent load steps were completed to prevent further deformation from overprinting the fault.

A.3.2 Microstructure

The microstructure of the first sample dehydrated at peak load has several unique characteristics. First, reaction products are clearly visible in most parts of the sample, with high contrast (bright) olivine grains decorating fractures, pore space, and the highly reacted fault core. There is a clear gradient in reaction extent away from the center of the deformed fault core where the antigorite has

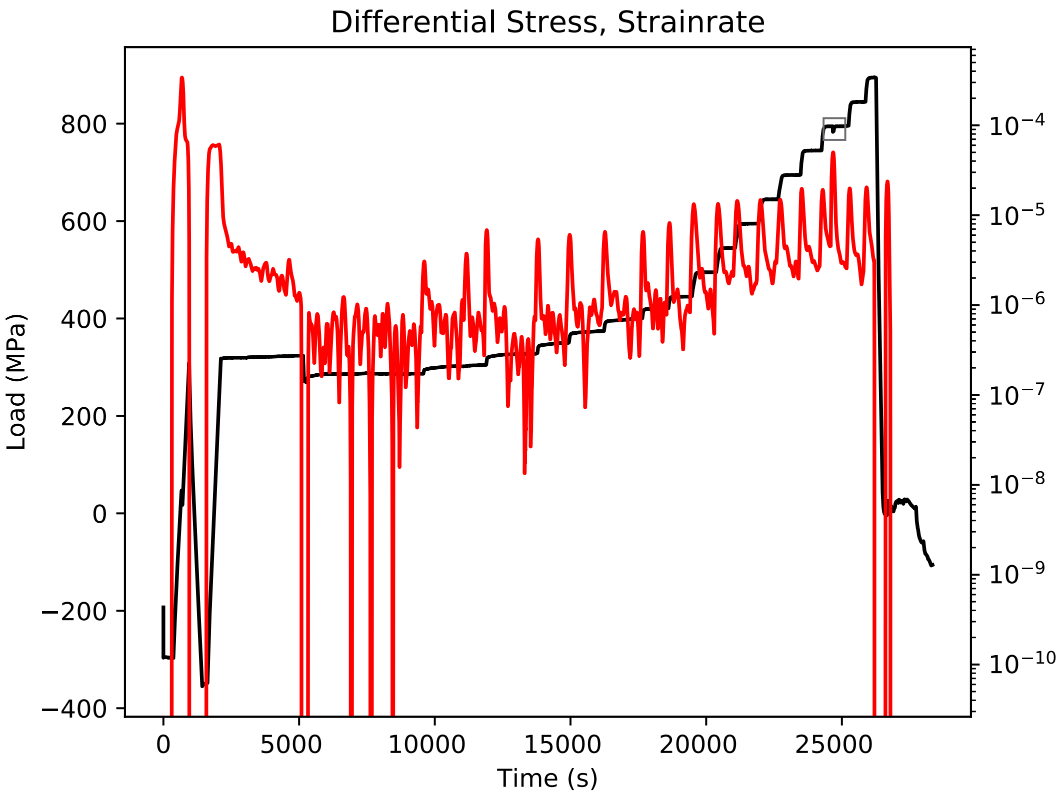

Figure A.4: Load-strainrate-time data from creep experiment W2446. The sample creeps at rates above 10^{-7} 1/s even at a stress of 500 MPa. Note the late stick-slip event outlined in grey.

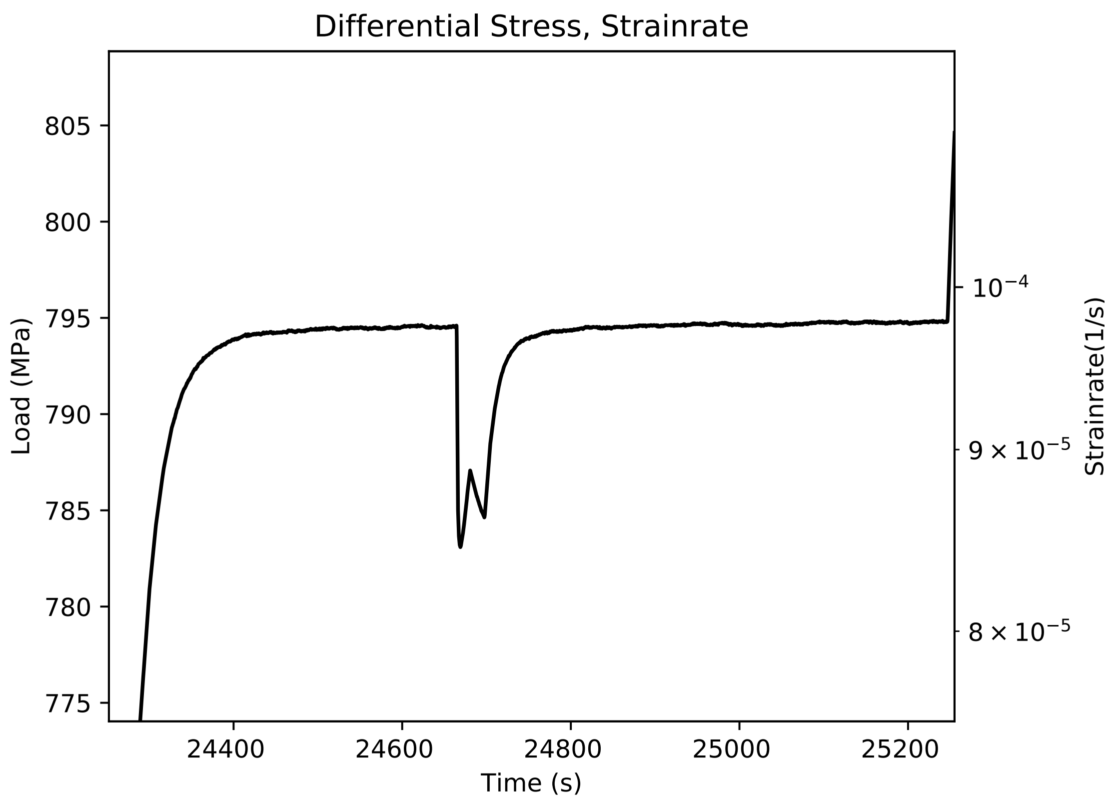

Figure A.5: Load-time data showing the rapid stick-slip event in experiment W2446. The 12 MPa load drop happens in a single sample interval at 10Hz recording rate. Corresponding microstructure and a relict fracture is shown in figure A.7

fully reacted to the shear piston surfaces, where reaction products are barely visible in intergranular porosity. Circular pores are present in the fault core which were presumably water-filled in-situ. The fault zone is relatively wide, with more than 200 µm of its 1200 µm thickness fully reacted after 10 mm of slip (Figure 1.13). Outside the fault zone, alignment of grains is poor, and a number of secondary fractures cross the sample in the R1 orientation. No kinking of the grains is preserved either inside or outside the fault core.

The second sample, which was also loaded quickly (”fast” $10^{-4}1/s$), but dehydrated before reaching peak stress, has pore space remaining throughout the sample. In contrast to the sample dehydrated at peak stress, there are fewer fractures, and less damage. Reaction extent is much lower, with reaction products mostly visible filling small (sub-micron) shear fractures. Faults are still relatively rough, with many antigorite grains torn and bent at the fault surfaces, and little evidence for plasticity outside the multiple 2 µm wide fault traces.

The sample loaded ”slowly” ($10^{-5}1/s$) and dehydrated at stress significantly below peak stress has little pore space remaining, and a single narrow ($1\mu m$) fracture running through its length (figure A.6). Porosity is not visible between grains. Antigorite grains $> 10\mu m$ from the fault surface are clearly plastically deformed, with kinks and bent grains visible. Near the fault surface deformation is more intense, with some grains displaying kink angles greater than 45 degrees. Despite this plasticity, the fracture appears very smooth (figure A.8). There is evidence of reaction on the fault, but it only extends 3 µm from the fault surface. These features roughly match the fault developed in a dehydrating creep experiment described in the next paragraph.

The creep experiment run at 620°C is a cored sample of mesh-textured antigorite, so the sample started with very low permeability and porosity, and no visible damage. The sample recovered after deformation has a single large fracture oriented 35 degrees to the compression axis. Offset on the fault matches the 200 um slip event recorded during deformation. The fault trace is jagged, with some smooth sections, apparently fractured along the grain boundaries of antigorite. Several sections of the fault rupture through grains of antigorite whose basal planes were oriented

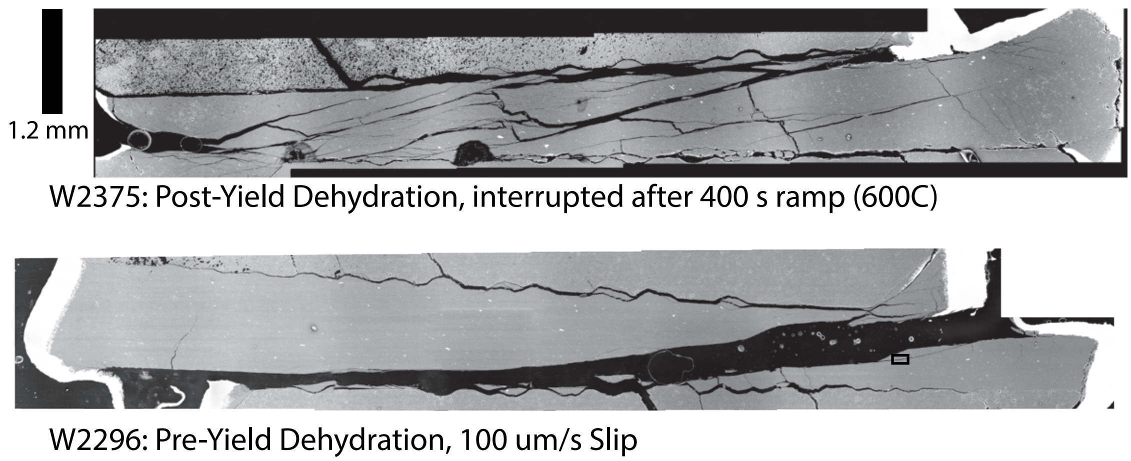

Figure A.6: Broad microstructure comparison of a sample loaded to peak stress, dehydrated, then quenched partway through the dehydration temperature ramp (top) compared to a sample dehydrated before yielding (bottom). Note differences in damage and faulting.

perpendicular to the fault surface. These poorly oriented grains are bent over and torn into submicron particles that fill short sections of the fault and have high backscatter contrast (bright) suggesting they are reacting due to the increased surface area.

A.4 Discussion

A.4.1 Overcoming Anisotropic Toughness

An unusual feature of sheet silicate deformation at high pressure is the dominance of shear cracking and linkage over dilatant wing crack bridging that causes failure in other brittle rocks. One might expect that shear crack bridging would generally be much weaker, but antigorite can reach strengths 1/2 those of granites at 1 GPa. Antigorite's strength comes from the combination of its cyrstal structure and unique mesh textures, where grains are often oriented with basal planes perpendicular to adjacent grains. Shear cracks would need to take multiple long 90 degree jogs (Escartin et al., 1997, figure 9), or penetrate through sheets of adjacent grains to bridge with other nearby cracks. When tested at room pressure, this structure also gives antigorite unusually high tensile strength among rocks (David et al., 2020, via Brazilian tensile tests), demonstrating the toughening effect the mesh texture contributes.

In-situ, the shear cracks impinging on perpendicular grains results in kinks, whose structures are discussed in chapter 2. At high strains, instead of tearing and sliding through the poorly oriented grains, new kinks form elsewhere in samples at high confining pressures. This results in highly distributed deformation in high shear stress orientations (Chapter 2, figure 2.3).

In samples deformed at 550°C in creep experiments, very few kinks are observed and grains appear "bent" and rotated from their original orientation with no additional porosity appearing (figure 2.8). It is easy to imagine how a stress-concentrating feature could generate an aligned strain localized zone above 550°C if it were given enough time to propagate through the sample. The fact that ductile features do not dominate previous experiments at this temperature (Chernak and Hirth, 2010; Proctor and Hirth, 2016) suggests that there is still some hardening that occurs, and if driven at "fast" strain rates the samples will tear grains to form a brittle fault along alignment set up during loading.

Brittle-Ductile Path and Rate Dependence

The series of experiments here describe a path through the brittle-ductile transition in antigorite that preserves/promotes what could be key elements for dynamic slip of antigorite: low permeability and localization.

In high strain rate gouge experiments there is very little time to close porosity and linked permeable paths. After yielding samples harden towards peak stress, tearing grains and opening paths between existing porosity. In addition, the hardening promotes distribution of deformation around a fault, instead of strong localization onto a single fault. The large amount of stored energy (+50% relative to dehydrating samples which showed stick-slip instability) at peak stress with a large amount of ground, amorphous antigorite gouge in the fault core contributes to rapid pore-fluid pressure weakening and shear heating as slip progresses to high strain (figure A.3). This structure is unlikely to exist in nature.

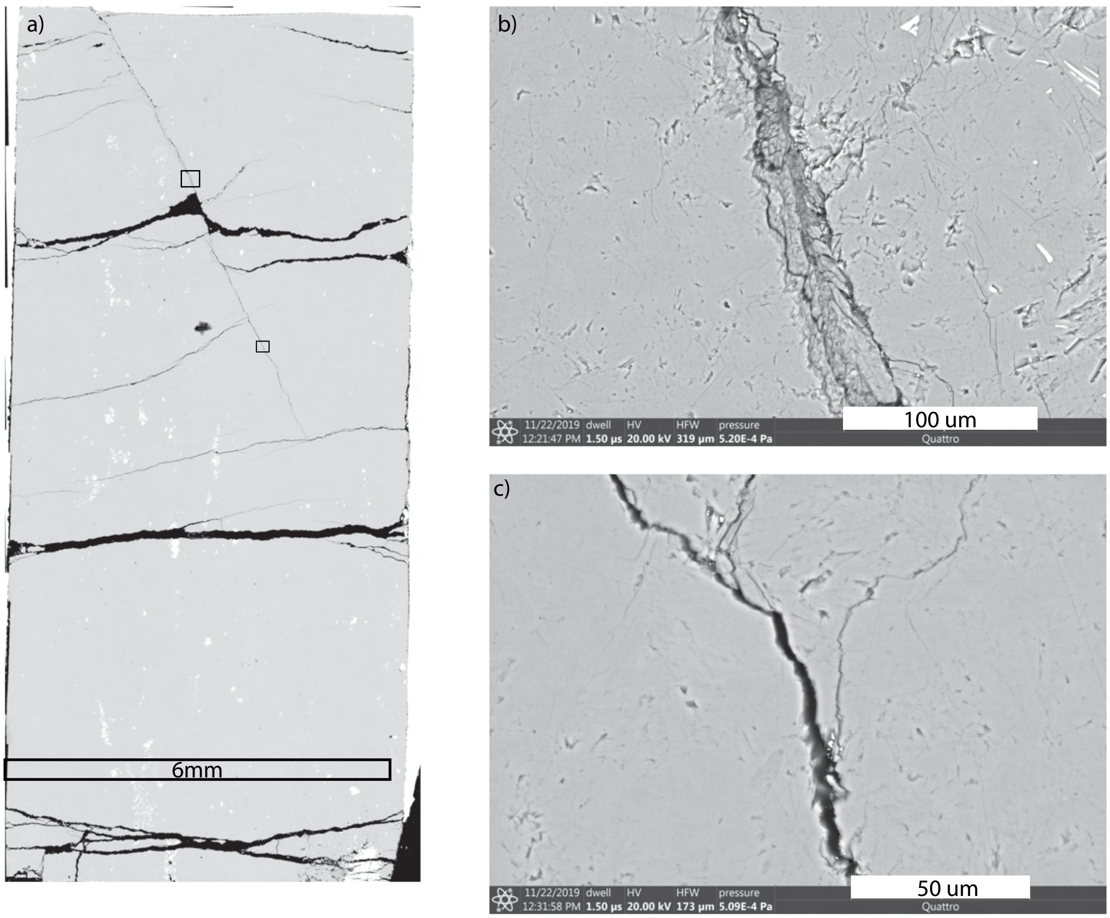

Figure A.7: a) SEM image of dehydrating creep sample W2446. Sub-image locations are noted by black boxes. b) Image of a rough fault section where poorly aligned grains are torn and bent back to form fault gouge. c) smooth section of the fault with no grains penetrating into the fault core and no visible gouge.

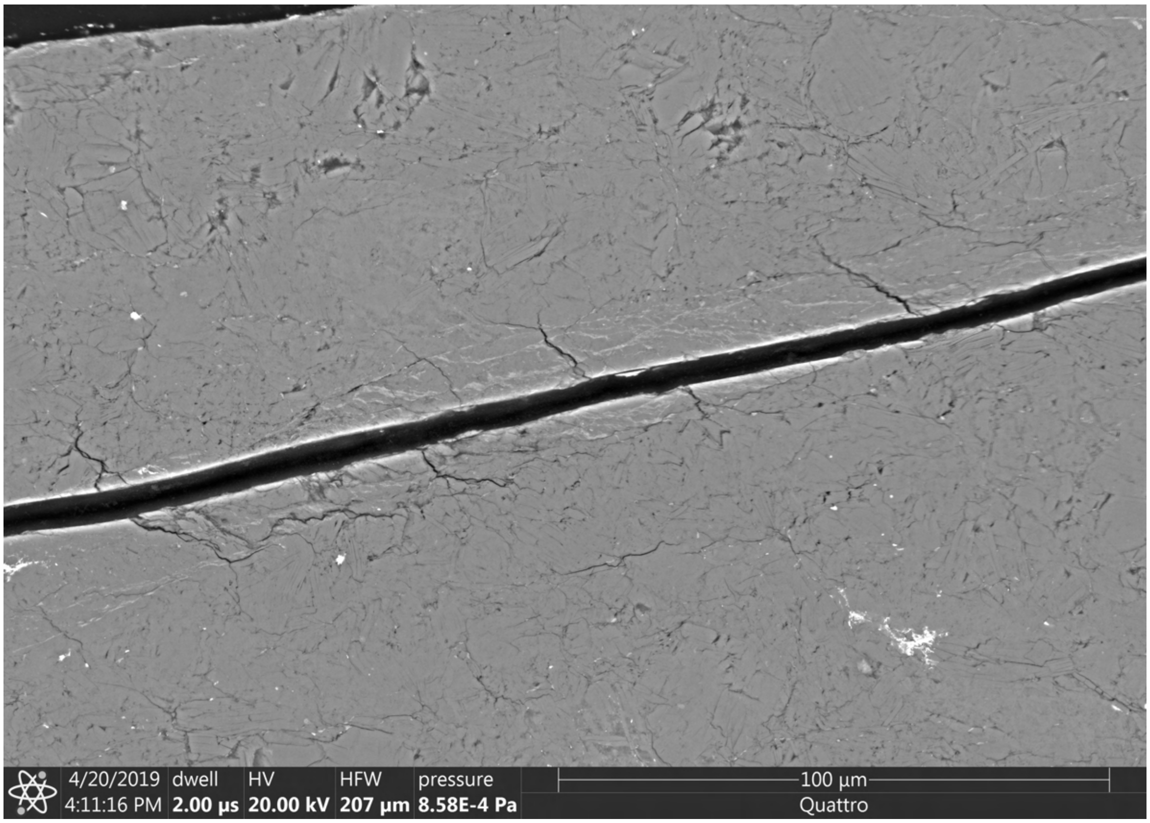

Figure A.8: SEM Image of reaction on the smooth fault surface from pre-yield experiment W2296. Location is noted in larger Figure A.6

If gouge samples are loaded to stress ”fast” but not loaded to peak stress, deformation does not distribute onto a wide fault core, but instead onto several narrow faults. The fast loading to stress does not allow time for sheets to align or close pores, so permeability remains high. The stored energy in the machine is lower at lower starting stress for dehydration, and the fault lacks gouge to react quickly so it weakens more slowly and still does not generate rapid slip events.

When gouge samples are loaded to stress ”slowly” and not loaded to peak stress, porosity/permeability normal to the fault closes (e.g. Kawano et al., 2011) and grains align to localize deformation onto a single narrow fault. The extra time to accommodate plastic deformation (several hours) allows this difference. There is very little deformation during the temperature ramping period due to the more cohesive nature of the sample, without gouge and porosity to generate significant early reaction products. Shortly after the sample reaches 700°C the smooth fault suddenly and rapidly slips, generating the small amount of observed reaction products on the fault surfaces. The very small amount of reaction products from high slip speed (in comparison to the sample loaded to peak stress) suggests the fault weakens very efficiently compared to the sample loaded to peak stress.

A.4.2 Natural Context

Natural antigorite bodies deform for very long times at low stress in subduction zones. If their microstructural development is similar to the process described above, they are most likely to behave like the slowly loaded dehydration or creep samples, developing strongly localized faults with anisotropic permeability. When these faults approach dehydration temperatures, they could rupture generating dynamic earthquake events like those we observe in the lab.

A.5 Conclusion

We deformed antigorite gouge and isotropic cores along three loading/creep paths and observed their weakening behavior. Samples loaded ”fast” to peak stress weakened quickly due to high reaction rates in their distributed, amorphized fault cores. Samples loaded ”fast” and dehydrated before peak stress weaken/react more slowly, with several active faults accommodating deformation and little shear heating activity. Samples loaded ”slowly” and dehydrated before peak stress had the least visible porosity and damage, with deformation localized onto a single fault which dynamically ruptured after very little weakening. These results together suggest further laboratory investigations of dehydration embrittlement should be conducted over long times on samples with mature, compacted faults. Natural faults are most like the ”slow” path, potentially resolving a longstanding mystery around the apparent rate-strengthening behavior coexisting with dehydration embrittlement.

Appendix B

Low Temperature Plastic Deformation of Confined Olivine With Free Surfaces

Eric Burdette, Cameron Meyers, and Greg Hirth

[1]Department of Earth, Environmental and Planetary Sciences, Brown University, Providence, RI, USA

Key Points:

- Porosity-free sintered olivine pillars were deformed at stresses up to 4 GPa at room temperature and 600°C.
- Kinks dominate surface microstructure, with many tightly spaced bands in optimally oriented bands.

B.1 Introduction

To understand the spatial and temporal distribution of earthquakes in the mantle lithosphere, as well as the processes responsible for the wide spectrum of fault slip behaviors, it is important to constrain rheological properties of olivine aggregates. Seismicity in the oceanic lithosphere is generally limited to depths at which the temperature is less than approximately 600°C. Seismic behavior is possible when the friction coefficient decreases with increasing sliding velocity (i.e., velocity weakening behavior characterized by rate-and-state friction). Laboratory studies on olivine friction at low normal stress demonstrate a transition from velocity weakening to velocity strengthening with an increase in temperature from 800 to 1000°C (Boettcher et al., 2007; King and Marone, 2012). Recent analyses of mantle fault rocks from oceanic transform faults provides evidence of fluid penetration facilitated by brittle deformation at temperatures up to 900°C – consistent with observations of seismicity in the mantle at transform faults at similar temperatures (Kuna et al., 2019; McGuire and Beroza, 2012; Roland et al., 2012). These observations have motivated analyses highlighting the importance of strain rate and temperature on lithosphere rheology near the brittle-plastic transition (e.g. Molnar, 2020).

A fundamental issue related to this problem is the magnitude of stresses supported by the mantle lithosphere near the brittle-plastic transition. Comparisons of geophysical data with geodynamic models suggest stresses do not exceed 300 MPa, a value far less than predicted by applying standard friction laws at the depth limit of seismicity (e.g., Kohlstedt et al., 1995). At these conditions, olivine aggregates are generally interpreted to deform by low-temperature plasticity (sometimes called Peierls creep) – a process that is rate-limited by dislocation glide. Laboratory tests and theory indicate that the yield strength for dislocation glide is considerably lower than the steady-state flow stress (e.g. Idrissi et al., 2016; Hansen et al., 2019), leading to more sophisticated analyses of strain hardening and grain-size effects (i.e. Hall-Petch) on dislocation glide in olivine. By accounting for these factors, the extrapolation of lab data can align with the geodynamic constraints for the stress magnitude if one considers low strain (i.e., prior to significant strain hardening) and low strain rate deformation (e.g. Hansen et al., 2019). However, these data are collected in relatively short times, making extrapolation uncertainty large, and recovered samples do not preserve microstructure (decompression stress/damage) that lead to proposed strain hardening and laws.

To better constrain low temperature plasticity mechanisms in olivine, we developed a new Griggs-apparatus assembly to deform strong pillars in hydraulic oil and loose graphite confining media which preserve pre-polished sample surfaces. The recovered samples illustrate activity of orientation-dependent kinking and grain interactions which is discussed below.

B.2 Materials and Methods

B.2.1 Materials

The samples used in our preliminary work were synthesized by evacuated hot pressing powdered San Carlos olivine in a Paterson-type gas-medium apparatus at 1250 °C and 300 MPa confining pressure. Active evacuation of the pore spaces leads to samples with <0.0001 porosity (Meyers et al., 2017, AGU abstract), such that they have high fracture toughness, enabling low-temperature plasticity at high confining pressures. Mean grain size is 10 μm.

Multiple rectangular pillars are cut from a single cylindrical hot-pressed sample. They are then squared and polished to 0.1 μm surface finish with diamond lapping paper.

B.2.2 Methods

Two new cell assemblies were designed for this work. The first relies on BUNA rubber seals to contain hydraulic oil inside the pressure vessel at room temperature (Figure B.1). Alignment of the pistons and sample are critical for even stress application so several additional elements are included which are not needed for typical oil-confined assemblies.

The second assembly adapts a standard assembly used for high temperature (600°C) creep tests by placing the sample pillar between alumina pistons inside an annealed brass sleeve. The sleeve has a drilled round hole whose diameter is slightly larger than the corner-to-corner distance of the pillar placed inside it. The space between the pillar and the sleeve is filled with loose graphite powder and the entire brass capsule is placed inside a standard annealed silver jacket. The brass prevents pre-loading of the sample during pressurization and anneals/weakens at high temperature to apply confining pressure and allow deformation of the sample. The brass jacket protects potentially brittle samples during decompression. The jacket is ground/machined off after deformation, and the pillar surfaces are protected by the graphite powder which can be brushed off.

Stress and displacement are determined using the methods described in Matej Pec's Rig 1.3 program (https://sites.google.com/site/rigprogram/home) and constant stress deformation methods described in Chapter 2.

B.3 Results

B.3.1 Mechanical Results

Broadly our results agree with Hansen et al. (2019). We record yielding at 2.4 GPa at room temperature, and strength at 600°C similar to that recorded by Hansen et al. (2019) (Figure B.2). At 2.25 GPa pressure samples are clearly less brittle, yielding and hardening for much longer than the

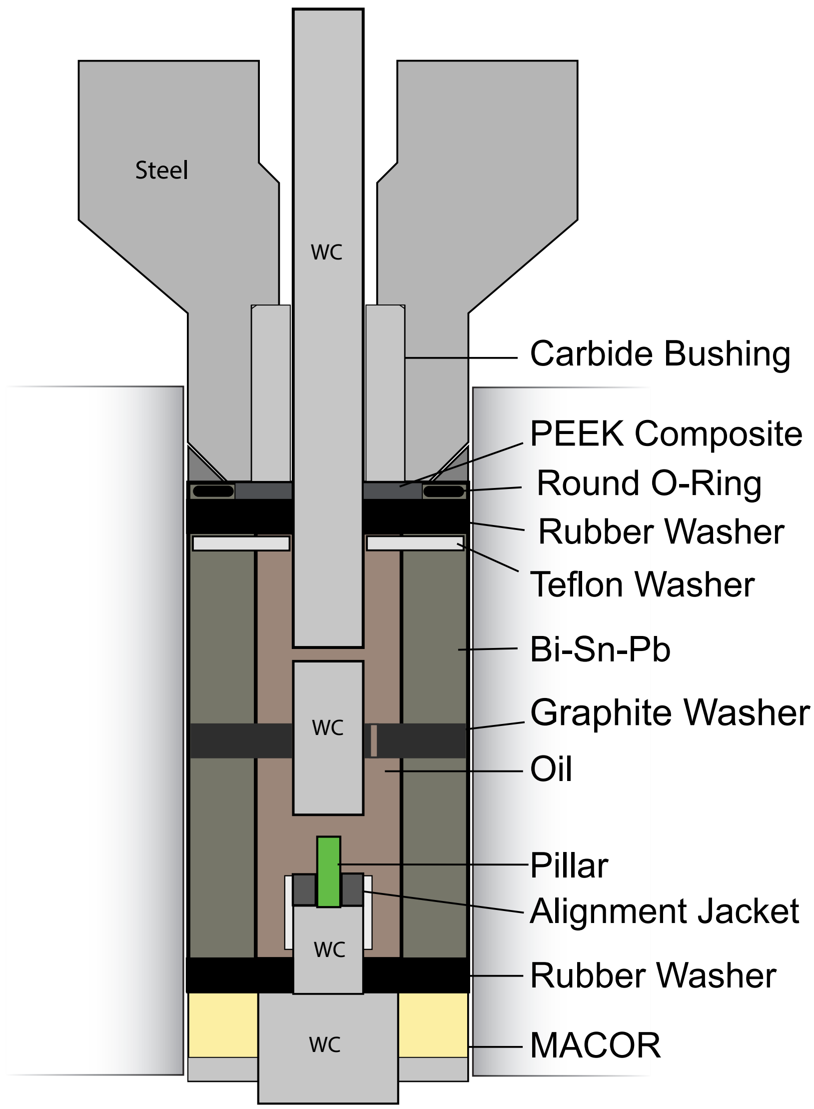

Figure B.1: Schematic of Modified assembly for olivine pillar deformation at room temperature

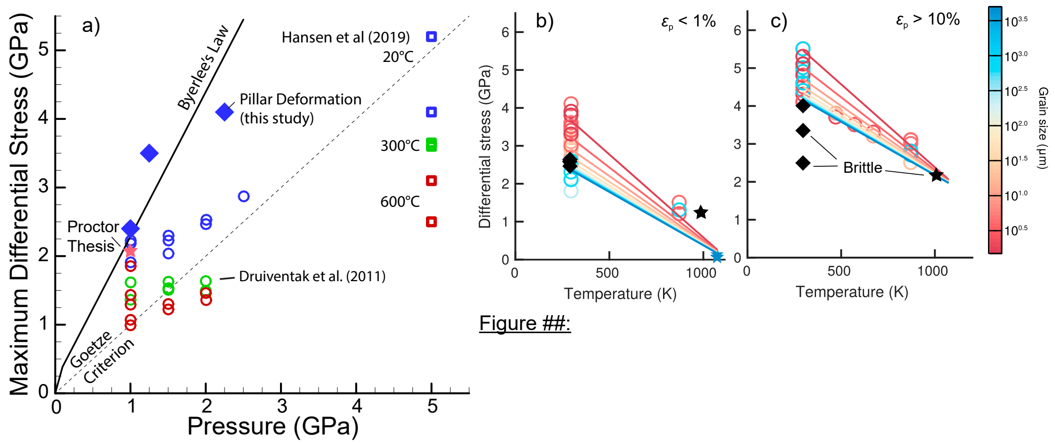

Figure B.2: Strength and yield data for olivine deformation. Diamonds are pillar experiments, star is published in the thesis of Brooks Proctor. a) is colored by temperature.

fracture at 1 GPa (Figure B.3). In all cases the samples approach brittle failure, with microcracks decorating grain boundaries (Figure B.4). Our results are significantly stronger than Druiventak et al. (2011), likely because natural dunites contain alteration phases at grains boundaries which could weaken them.

B.3.2 Microstructure

Because samples were initially lapped below 0.1 um roughness with colloidal silica, so optically visible changes represent changes in surface topography induced by deformation. Samples were characterized optically first (Figure B.4). The images show light and dark bands throughout single grains. The bands are mostly oriented perpendicular to the axial compression direction. Cracks are prevalent throughout the images, found almost exclusively along grain boundaries. Grains were also characterized with a Brukers AXS atomic force microscope and ultrasharp contact tips. The images show 'steps' at a smaller scale than was optically visible (Figure B.5). A transect perpendicular to the bands (Figure B.6) shows the existence of sharp corners on these steps, and similar angles throughout the set of about 5 degrees. Some of these steps are on the order of 1 nm potentially constituting single slip bands.

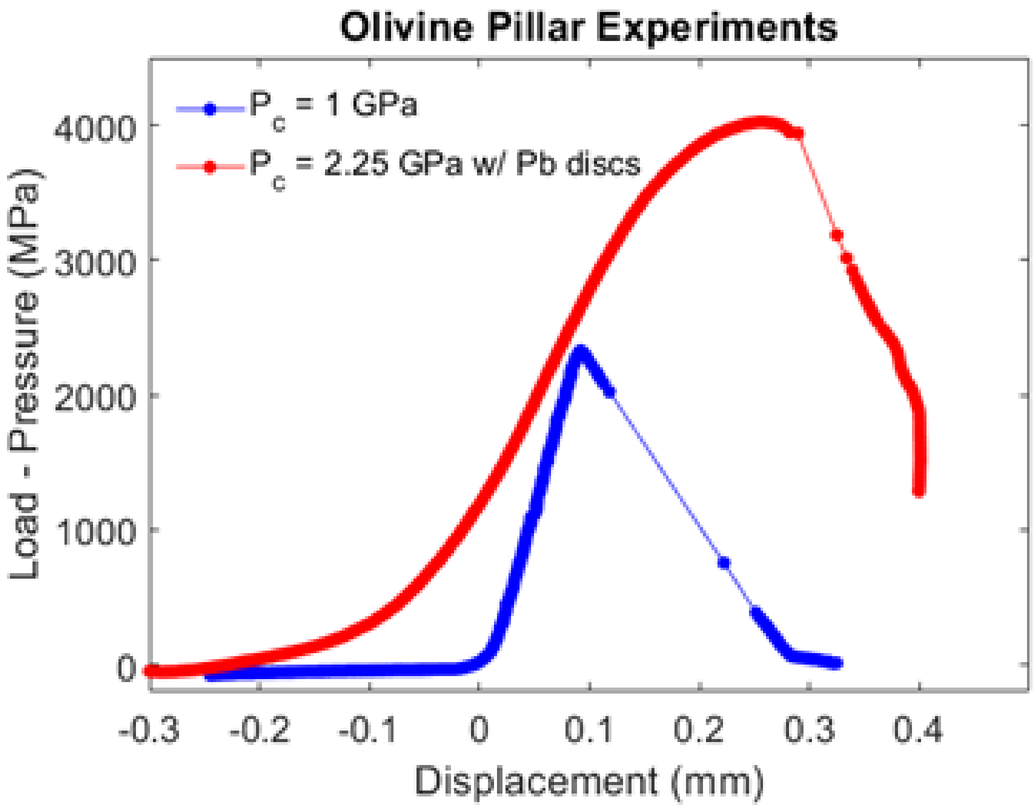

Figure B.3: Room temperature deformation data for two olivine pillars

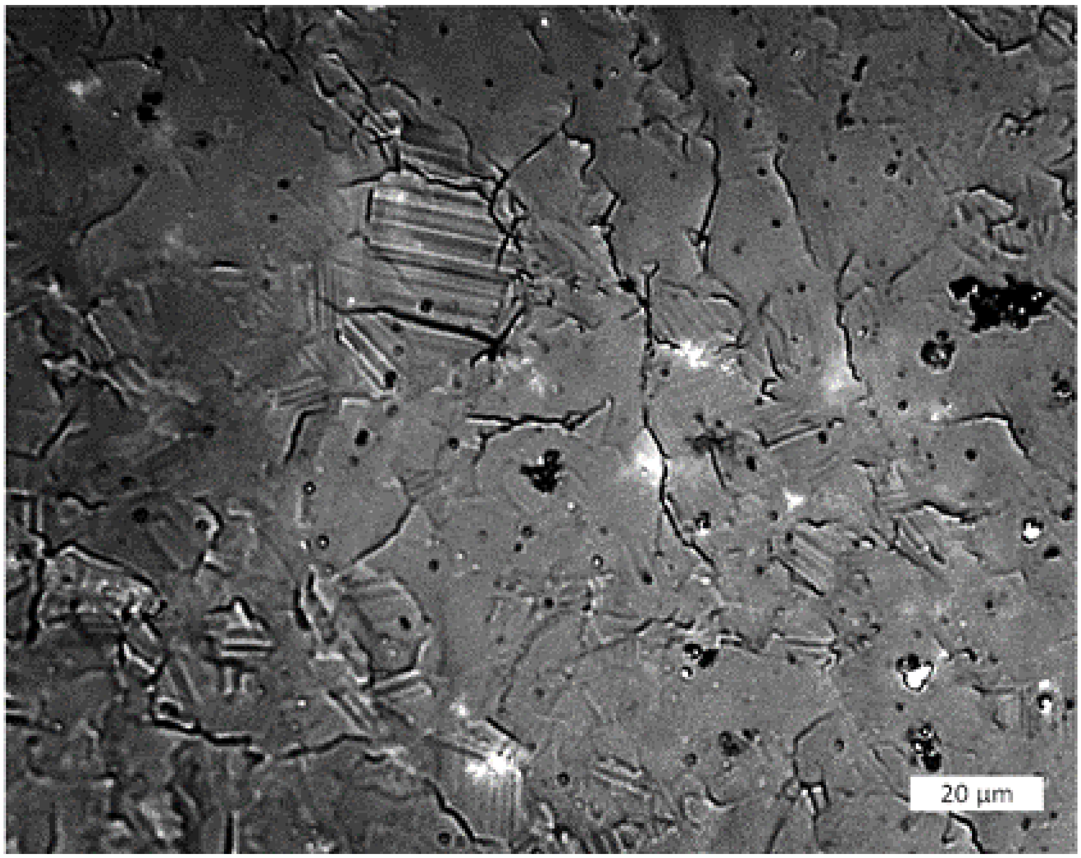

Figure B.4: Optical image of olivine surface recovered after room temperature deformation. Cracks are common along grain boundaries, and optical topography contrast is due to misorientation of kink bands to the surrounding surface. Compression direction is vertical.

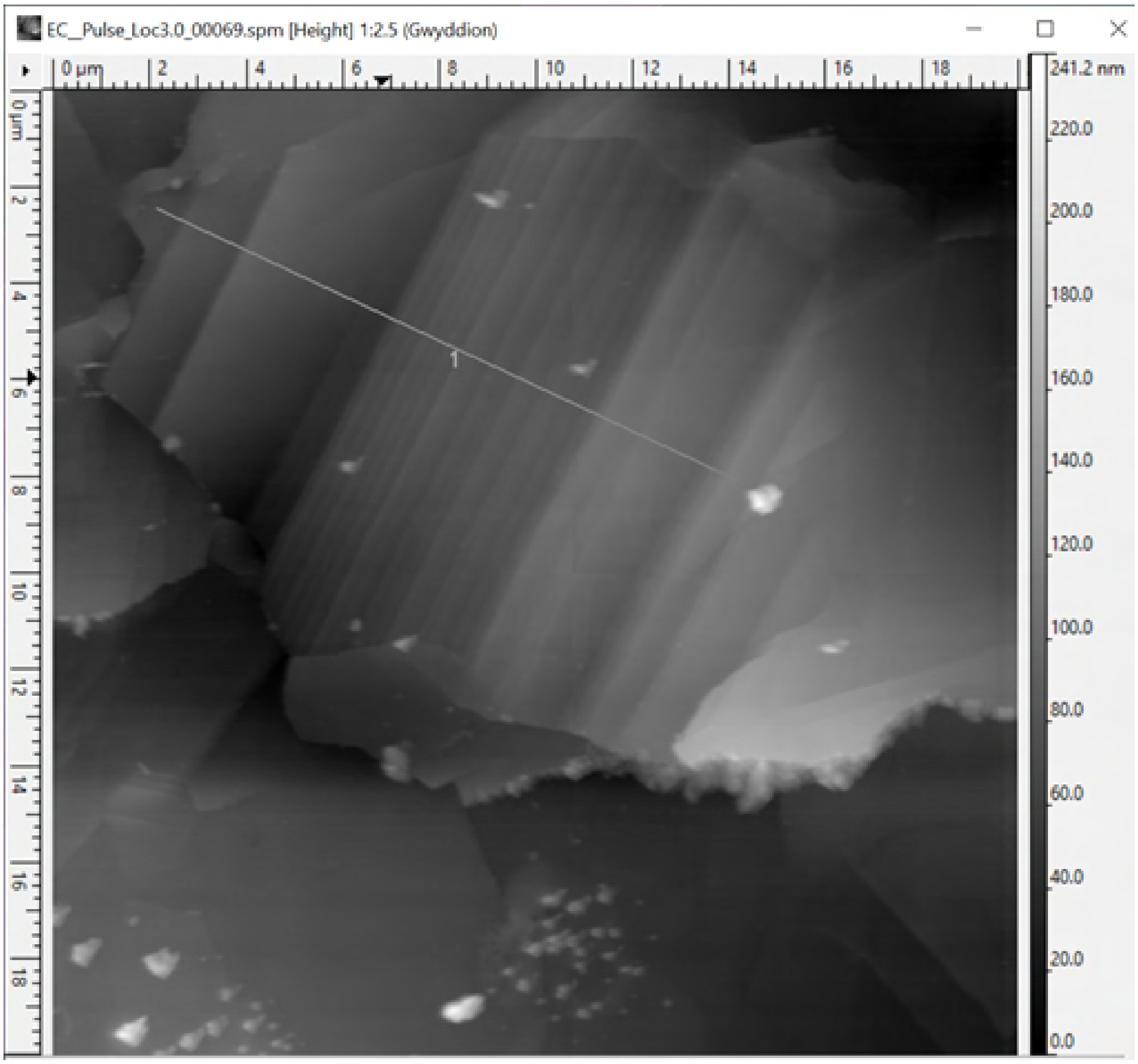

Figure B.5: AFM image of a deformed grainwith stepwise kink bands. Many small features are visible that cannot be resolved optically.

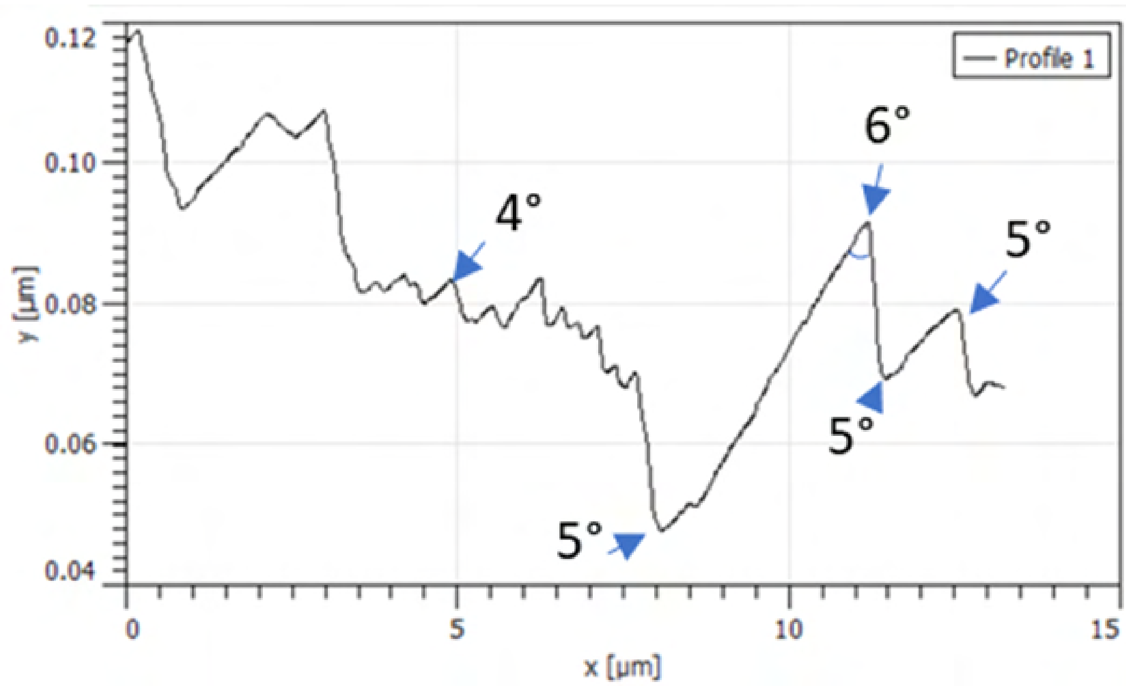

Figure B.6: Profile along transect perpendicular to kink bands in Figure B.5. Topography is exaggerated, and steps as small as 1 nm are resolved in the trace.

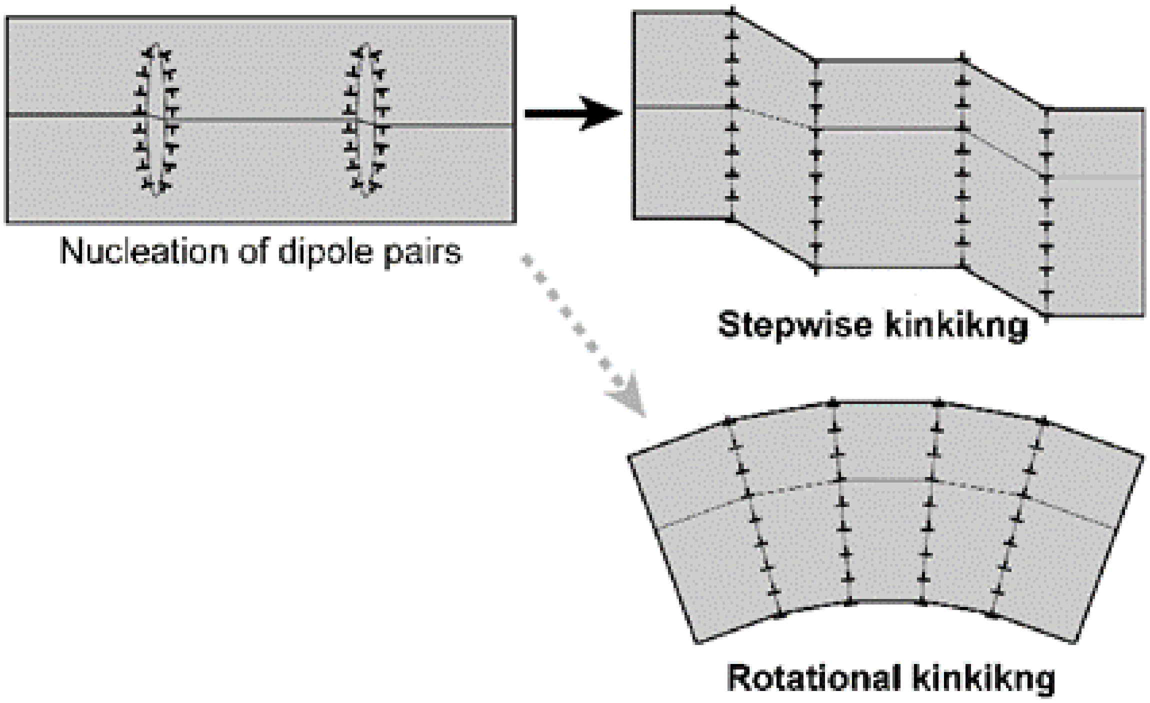

Figure B.7: Diagram showing schematically ho kinks produce the surface topography

B.4 Discussion

B.4.1 Kinks

Nucleation of pairs of dislocations in the direction of axial compression could form dipole pairs which expand until they reach the edges of the sample and form kinks (Figure B.7). The low angles we record in AFM support this hypothesis, although EBSD and TEM will be needed to characterize dislocation density variation with depth to verify the model.

B.4.2 Mechanical strength

These experiments show that even at room temperature, olivine can deform by dislocation motion in polycrystalline samples. The observed deformation is clearly strongly orientation dependent, which could pose problems for extrapolating single-crystal mechanisms to polycrystalline samples. We plan to continue examining hardening and long-term creep rate in future studies.

B.5 Conclusions

Here we deformed vacuum-sintered olivine at room temperature and 600°C in novel assemblies to preserve surface features. The samples had strengths similar toHansen et al. (2019), and show a clear surface pattern indicating orientation-dependent kinking was active.

1. Kink bands dominate room temperature deformation in olivine.
2. Small features on the order of one burgers vector are present on the surface, possibly representing the termination of single-dislocation slip bands.
3. Features are strongly orientation dependent, suggesting activation of a single slip system in olivine.

Acknowledgments
We would like to thank Lars Hansen for helpful discussions.

Appendix C

Griggs Assembly Thermal Structure

C.1 Thermal Model Notes

Thermal modeling of a Griggs-type assembly is detailed in Moarefvand et al. (2021). Solutions to the steady-state heat equation are straightforward with modern finite element solvers (e.g. MATLAB PDEmodeler), and can be easily verified with analytical solutions to simple problems such as stacked cylinders with fixed temperature at each end and radial sleeves with a central heat source. Some work was completed for piston cylinders both experimental (Watson et al., 2002) and numerical (Hernlund et al., 2006; Schilling and Wunder, 2004) . Previous work has not examined a few of the realistic concerns of high pressure assemblies. These are:

1. Inadequate water cooling
2. Salt thermal conductivity
3. Temperature dependent graphite resistivity
4. Compression of the assembly

C.1.1 Water Cooling

Previous models typically used fixed temperature boundary conditions. The fixed temperatures are often not measured because they are at an interface between a plate with water channels and the top or bottom face of the pressure vessel. They are also often very close to the edge of the pressurized assembly rather than at the walls of water cooling channels to save computational time. In assemblies with low thermal conductivity along their central axis, most of the lost heat leaves by transferring radially to high conductivity materials at the ends of the furnace (e.g. copper washers/electrodes). Some assemblies have higher axial thermal conductivity than radial thermal conductivity at their ends, which causes axial heat to penetrate relatively deep into the support plates which must be solid under volume of the pressure vessel.

In Griggs assemblies the top of assemblies has relatively high axial and radial thermal thermal conductivity, with a large cooling channel directly on the pressure vessel for setups without end loading. The bottom of the assembly is traditionally made of a 1/2 inch tungsten carbide electrode surrounded by a 1 inch outer diameter ceramic (pyrophyllite or MACOR) which has low effective radial thermal conductivity. Water channels in original baseplates have a single 1/8 inch ID copper water tube tasked with removing all heat flowing out the bottom of the assembly. This difference in heat removal capacity causes the hot zone to be lower in the vessel than symmetric assemblies, and can heat the baseplate above 200°C, decreasing its strength. Supporting information in chapter 4 shows the effect of a simple reversal of materials to a central alumina piston and an outer steel ring, reducing baseplate temperatures by 100°C.

C.1.2 Salt thermal conductivity

Salt makes up the bulk of the 'hot zone' in Griggs assemblies so its properties have a disproportionate effect on thermal structure of the assembly. NaCl and KCl have similar conductivites of 4 W/m/K at 700°C and 1 GPa, while those of KBr and KI are roughly half that. CsCl thermal conductivity is approximately 1 W/m/k, near that of pyrophyllite and MACOR (Andersson, 1985). By switching salt outside the furnace from NaCl to KBr, required power to reach a given sample temperature decreases by 25% and pressure vessel temperature decreases by as much as 80°C. CsCl would be a further improvement but its cost is higher. Thermal uniformity around the sample assembly is best when using NaCl or KCl. CaF2 has higher thermal conductivity, but possible fluoride contamination is hazardous. MgO is another excellent choice, but it is be better used with a small fraction (15%) of salt to reduce its strength.

C.1.3 Temperature dependent graphite resistivity

Graphite has well documented electrical resistivity that is dependent on temperature. Resistivity reaches a minimum fractional resistance 0.6 of its room temperature value at 700°C, and slowly rises back to its original value around 2800°C (Okada et al., 2017). Joule heating in Griggs assemblies depends directly on this resistivity, and the decrease serves to spread heat generation. A thermally conductive sleeve inside the furnace (as is used in many experiments above 1000°C) can further improve uniformity.

C.1.4 Compression of the assembly

Distortion of the assembly is also often not accounted for. Salts (even those hydrostatically pressed to 200 MPa) typically have 3-6 % porosity that is collapsed when assemblies are pressurized, and elastically compress once material is densified. In models, this would result in higher power per volume, increasing temperature and moving hot zones up to a millimeter. This could be compensated in reality by increasing thermal conductivity with temperature.

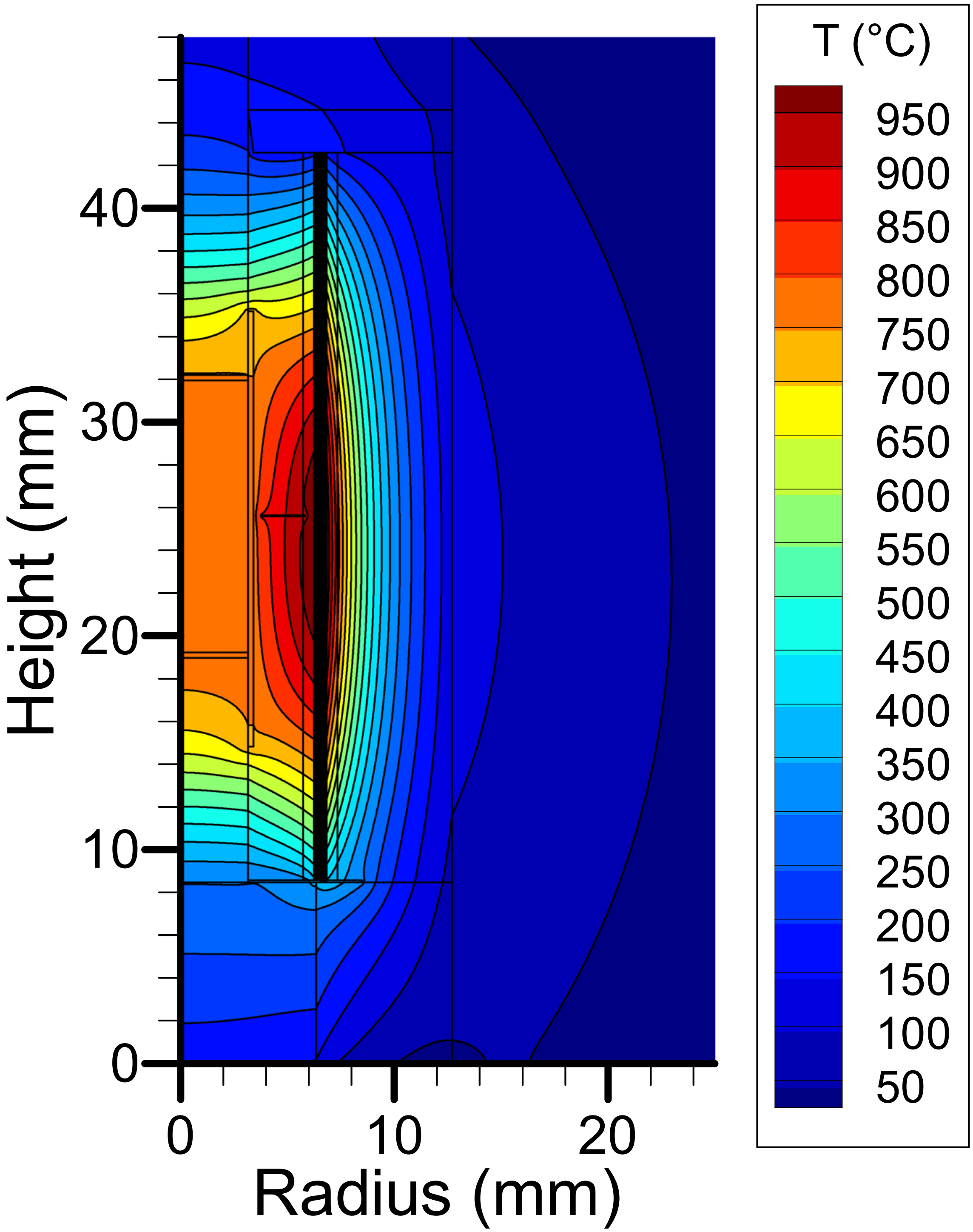

Figure C.1: Thermal model results. Methods are detailed in Moarefvand et al (in press)

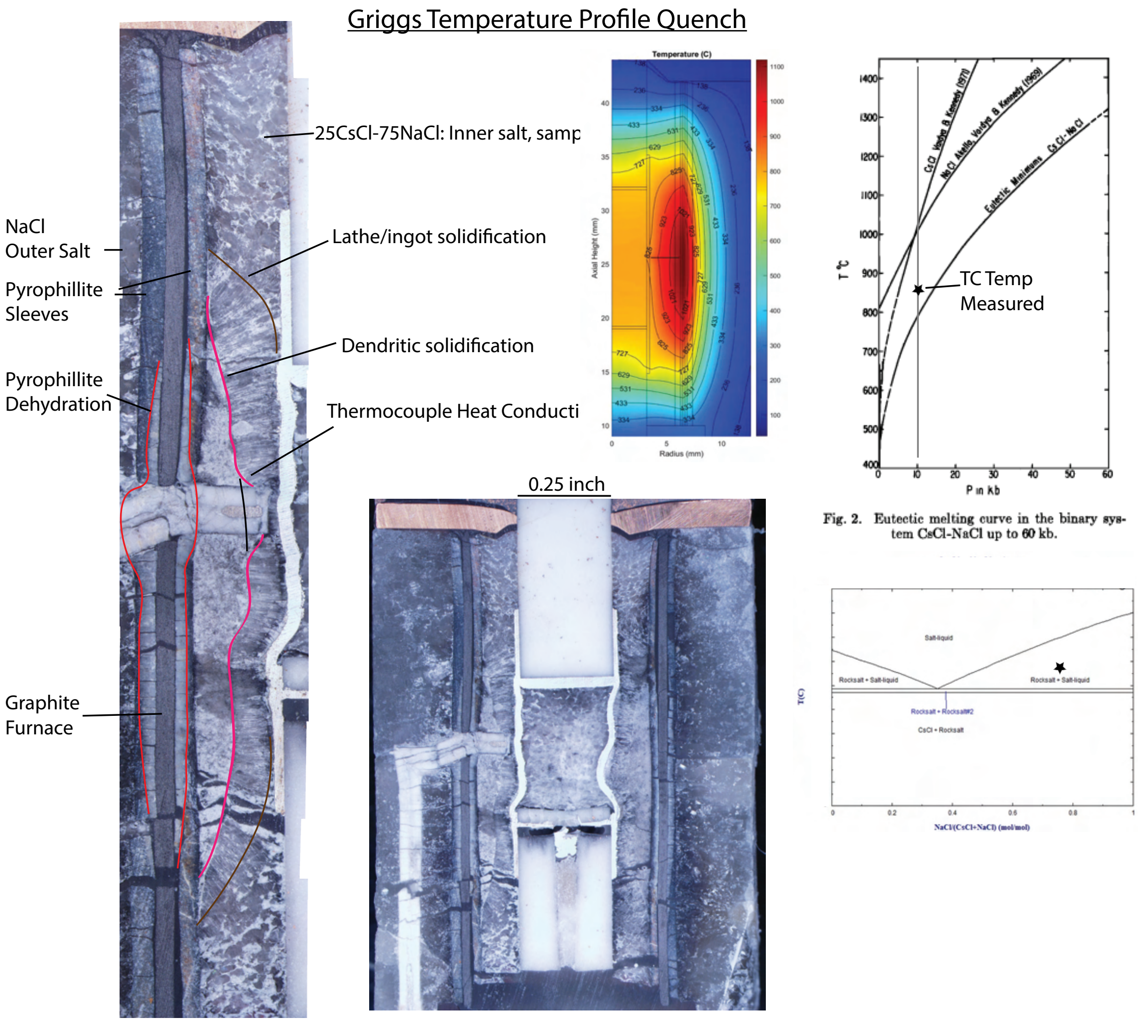

Figure C.2: A section of an assembly quenched from 850°C, impregnated with epoxy, and sectioned to determine temperate profiles. Original NaCl grains were large and are visible in the sample. Microstructural features are noted. Phase diagrams are reproduced from Kim et al. (1972)

C.1.5 Temperature profile measurement

Temperature distribution in the assembly is very difficult to accurately measure because of this compaction (thermocouples have uncertain positions). Chemical methods are employed above 1200°C, but most experiments in Griggs rigs are completed at lower temperature when salt is not completely molten. We made an attempt to quench an assembly filled with a NaCl-CsCl (75:25 molar) partial melt (Kim et al., 1972). Despite cooling from 850°C to 100°C in a minute, fractionation apparently occurred and a dendritic-lathe-granular (ingot) solidification texture developed (figure C.2). The contours of these regions outline temperature-time transitions along heat flow contours which roughly match model positions and asymmetry, but do not give quantitative temperatures. Future activity will focus on magnesite-dolomite reactions which can be used at 800°C.

Bibliography

Amiguet, E., Van De Moortèle, B., Cordier, P., Hilairet, N., and Reynard, B. (2014). Deformation mechanisms and rheology of serpentines in experiments and in nature. *Journal of Geophysical Research: Solid Earth*, 119(6):4640–4655.

Andersson, P. (1985). Thermal conductivity under pressure and through phase transitions in solid alkali halides. i. experimental results for kcl, kbr, ki, rbcl, rbbr and rbi. *Journal of Physics C: Solid State Physics*, 18(20):3943.

Auzende, A.-L., Escartin, J., Walte, N. P., Guillot, S., Hirth, G., and Frost, D. J. (2015). Deformation mechanisms of antigorite serpentinite at subduction zone conditions determined from experimentally and naturally deformed rocks. *Earth and Planetary Science Letters*, 411:229–240.

Barsoum, M. W. and Radovic, M. (2011). Elastic and mechanical properties of the max phases. *Annual review of materials research*, 41:195–227.

Blacic, J. and Hagman, R. (1977). Wide-band optical–mechanical system for measuring acoustic emissions at high temperature and pressure. *Review of Scientific Instruments*, 48(7):729–732.

Boettcher, M. S., Hirth, G., and Evans, B. (2007). Olivine friction at the base of oceanic seismogenic zones. *Journal of Geophysical Research: Solid Earth*, 112(B1).

Brantut, N., Baud, P., Heap, M., and Meredith, P. (2012). Micromechanics of brittle creep in rocks. *Journal of Geophysical Research: Solid Earth*, 117(B8).

Brantut, N. and Sulem, J. (2012). Strain localization and slip instability in a strain-rate hardening, chemically weakening material. *Journal of Applied Mechanics-Transactions of the Asme*, 79(3):031004–031004–10.

Burdette, E. and Hirth, G. (2020). Enhanced dehydration weakening of antigorite driven by slow shear heating: Insights from high-pressure experiments with a modified apparatus stiffness. *Journal of Geophysical Research: Solid Earth*, 125(11):e2020JB020064.

Chernak, L. J. and Hirth, G. (2010). Deformation of antigorite serpentinite at high temperature and pressure. *Earth and Planetary Science Letters*, 296(1-2):23–33.

Chernak, L. J. and Hirth, G. (2011). Syndeformational antigorite dehydration produces stable fault slip. *Geology*, 39(9):847–850.

David, E. C., Brantut, N., Hansen, L. N., and Mitchell, T. M. (2018). Absence of stress-induced anisotropy during brittle deformation in antigorite serpentinite. *Journal of Geophysical Research: Solid Earth*, 123(12):10–616.

David, E. C., Brantut, N., and Hirth, G. (2020). Sliding crack model for nonlinearity and hysteresis in the triaxial stress-strain curve of rock, and application to antigorite deformation. *Journal of Geophysical Research: Solid Earth*, 125(10):e2019JB018970.

Dieterich, J. H. (1979). Modeling of rock friction .1. experimental results and constitutive equations. *Journal of Geophysical Research*, 84(Nb5):2161–2168.

Dieterich, J. H. and Linker, M. F. (1992). Fault stability under conditions of variable normal stress. *Geophysical Research Letters*, 19(16):1691–1694.

Druiventak, A., Trepmann, C. A., Renner, J., and Hanke, K. (2011). Low-temperature plasticity of olivine during high stress deformation of peridotite at lithospheric conditions—an experimental study. *Earth and Planetary Science Letters*, 311(3-4):199–211.

Escartin, J., Hirth, G., and Evans, B. (1997). Effects of serpentinization on the lithospheric strength and the style of normal faulting at slow-spreading ridges. *Earth and Planetary Science Letters*, 151(3-4):181–189.

Evans, B. and Goetze, C. (1979). The temperature variation of hardness of olivine and its implication for polycrystalline yield stress. *Journal of Geophysical Research: Solid Earth*, 84(B10):5505–5524.

Ferrand, T. P., Hilairet, N., Incel, S., Deldicque, D., Labrousse, L., Gasc, J., Renner, J., Wang, Y., Green Ii, H. W., and Schubnel, A. (2017). Dehydration-driven stress transfer triggers intermediate-depth earthquakes. *Nature Communications*, 8:15247.

French, M. E., Hirth, G., and Okazaki, K. (2019). Fracture-induced pore fluid pressure weakening and dehydration of serpentinite. *Tectonophysics*, 767:228168.

Frost, H. J. and Ashby, M. F. (1982). *Deformation mechanism maps: the plasticity and creep of metals and ceramics*. Pergamon press.

Gasc, J., Hilairet, N., Yu, T., Ferrand, T., Schubnel, A., and Wang, Y. (2017). Faulting of natural serpentinite: Implications for intermediate-depth seismicity. *Earth and Planetary Science Letters*, 474:138–147.

Gasc, J., Schubnel, A., Brunet, F., Guillon, S., Mueller, H. J., and Lathe, C. (2011). Simultaneous acoustic emissions monitoring and synchrotron x-ray diffraction at high pressure and temperature: Calibration and application to serpentinite dehydration. *Physics of the Earth and Planetary Interiors*, 189(3-4):121–133.

Grobéty, B. (2003). Polytypes and higher-order structures of antigorite: A tem study. *American Mineralogist*, 88(1):27–36.

Hacker, B. R., Peacock, S. M., Abers, G. A., and Holloway, S. D. (2003). Subduction factory

2. are intermediate-depth earthquakes in subducting slabs linked to metamorphic dehydration reactions? *Journal of Geophysical Research: Solid Earth*, 108(B1).

Hansen, L. N., David, E. C., Brantut, N., and Wallis, D. (2020). Insight into the microphysics of antigorite deformation from spherical nanoindentation. *Philosophical Transactions of the Royal Society A*, 378(2165):20190197.

Hansen, L. N., Kumamoto, K. M., Thom, C. A., Wallis, D., Durham, W. B., Goldsby, D. L., Breithaupt, T., Meyers, C. D., and Kohlstedt, D. L. (2019). Low-temperature plasticity in olivine: Grain size, strain hardening, and the strength of the lithosphere. *Journal of Geophysical Research: Solid Earth*, 124(6):5427–5449.

Hernlund, J., Leinenweber, K., Locke, D., and Tyburczy, J. A. (2006). A numerical model for steady-state temperature distributions in solid-medium high-pressure cell assemblies. *American Mineralogist*, 91(2-3):295–305.

Hilairet, N., Reynard, B., Wang, Y., Daniel, I., Merkel, S., Nishiyama, N., and Petitgirard, S. (2007). High-pressure creep of serpentine, interseismic deformation, and initiation of subduction. *Science*, 318(5858):1910–3.

Hirauchi, K.-i., Katayama, I., and Kouketsu, Y. (2020). Semi-brittle deformation of antigorite serpentinite under forearc mantle wedge conditions. *Journal of Structural Geology*, 140:104151.

Idrissi, H., Bollinger, C., Boioli, F., Schryvers, D., and Cordier, P. (2016). Low-temperature plasticity of olivine revisited with in situ tem nanomechanical testing. *Science advances*, 2(3):e1501671.

Idrissi, H., Samaee, V., Lumbeeck, G., van der Werf, T., Pardoen, T., Schryvers, D., and Cordier, P. (2020). In situ quantitative tensile testing of antigorite in a transmission electron microscope. *Journal of Geophysical Research: Solid Earth*, 125(3):e2019JB018383.

Karato, S.-i. (2008). Deformation of earth materials. *An Introduction to the Rheology of Solid Earth*, 463.

Kawano, S., Katayama, I., and Okazaki, K. (2011). Permeability anisotropy of serpentinite and fluid pathways in a subduction zone. *Geology*, 39(10):939–942.

Kim, K.-T., Vaidya, S., and Kennedy, G. (1972). Effect of pressure on the temperature of the eutectic minimums in two binary systems: Naf-nacl and cscl-nacl. *Journal of Geophysical Research*, 77(35):6984–6989.

King, D. and Marone, C. (2012). Frictional properties of olivine at high temperature with applications to the strength and dynamics of the oceanic lithosphere. *Journal of Geophysical Research: Solid Earth*, 117(B12).

Kirby, S. H. and Kronenberg, A. K. (1984). Deformation of clinopyroxenite: Evidence for a transition in flow mechanisms and semibrittle behavior. *Journal of Geophysical Research: Solid Earth*, 89(B5):3177–3192.

Kirkendall, C. K. and Dandridge, A. (2004). Overview of high performance fibre-optic sensing. *Journal of Physics D: Applied Physics*, 37(18):R197.

Kocks, U. and Mecking, H. (2003). Physics and phenomenology of strain hardening: the fcc case. *Progress in materials science*, 48(3):171–273.

Kuna, V. M., Nábělek, J. L., and Braunmiller, J. (2019). Mode of slip and crust–mantle interaction at oceanic transform faults. *Nature Geoscience*, 12(2):138–142.

McGuire, J. J. and Beroza, G. C. (2012). A rogue earthquake off sumatra. *Science*, 336(6085):1118–1119.

Milsch, H., Heinrich, W., and Dresen, G. (2003). Reaction-induced fluid flow in synthetic quartz-bearing marbles. *Contributions to Mineralogy and Petrology*, 146(3):286–296.

Moarefvand, A., Gasc, J., Fauconnier, J., Baïsset, M., Burdette, E., Labrousse, L., and Schubnel, A. (2021). A new generation griggs apparatus with active acoustic monitoring. *Tectonophysics*, page 229032.

Molnar, P. (2020). The brittle-plastic transition, earthquakes, temperatures, and strain rates. *Journal of Geophysical Research: Solid Earth*, 125(7):e2019JB019335.

Murrell, S. A. F. and Ismail, I. A. H. (1976). The effect of decomposition of hydrous minerals on the mechanical properties of rocks at high pressures and temperatures. *Tectonophysics*, 31(3-4):207–258.

Nowakowski, B., Smith, D., and Smith, S. (2016). Highly compact fiber fabry-perot interferometer: A new instrument design. *Review of Scientific Instruments*, 87(11):115102.

Okada, M., Ohta, N., Yoshimoto, O., Tatsumi, M., and Inagaki, M. (2017). Review on the high-temperature resistance of graphite in inert atmospheres. *Carbon*, 116:737–743.

Okazaki, K. and Hirth, G. (2016). Dehydration of lawsonite could directly trigger earthquakes in subducting oceanic crust. *Nature*, 530(7588):81–4.

Okazaki, K. and Katayama, I. (2015). Slow stick slip of antigorite serpentinite under hydrothermal conditions as a possible mechanism for slow earthquakes. *Geophysical Research Letters*, 42(4):1099–1104.

Proctor, B. and Hirth, G. (2015). Role of pore fluid pressure on transient strength changes and fabric development during serpentine dehydration at mantle conditions: Implications for subduction-zone seismicity. *Earth and Planetary Science Letters*, 421:1–12.

Proctor, B. and Hirth, G. (2016). “ductile to brittle” transition in thermally stable antigorite gouge at mantle pressures. *Journal of Geophysical Research: Solid Earth*, 121(3):1652–1663.

Proctor, B., Mitchell, T. M., Hirth, G., Goldsby, D., Zorzi, F., Platt, J. D., and Di Toro, G. (2014). Dynamic weakening of serpentinite gouges and bare surfaces at seismic slip rates. *J Geophys Res Solid Earth*, 119(11):8107–8131.

Raleigh, C. B. and Paterson, M. S. (1965). Experimental deformation of serpentinite and its tectonic implications. *Journal of Geophysical Research*, 70(16):3965–&.

Reinen, L. A., Weeks, J. D., and Tullis, T. E. (1994). The frictional behavior of lizardite and antigorite serpentinites - experiments, constitutive models, and implications for natural faults. *Pure and Applied Geophysics*, 143(1-3):317–358.

Roland, E., Lizarralde, D., McGuire, J. J., and Collins, J. A. (2012). Seismic velocity constraints on the material properties that control earthquake behavior at the quebrada-discovery-gofar transform faults, east pacific rise. *Journal of Geophysical Research: Solid Earth*, 117(B11).

Ruina, A. (1983). Slip instability and state variable friction laws. *Journal of Geophysical Research*, 88(Nb12):359–370.

Rutter, E. H., Llana-Funez, S., and Brodie, K. H. (2009). Dehydration and deformation of intact cylinders of serpentinite. *Journal of Structural Geology*, 31(1):29–43.

Rybacki, E., Renner, J., Konrad, K., Harbott, W., Rummel, F., and Stöckhert, B. (1998). A servohydraulically-controlled deformation apparatus for rock deformation under conditions of ultra-high pressure metamorphism. *pure and applied geophysics*, 152(3):579–606.

Sawai, M., Katayama, I., Hamada, A., Maeda, M., and Nakashima, S. (2013). Dehydration kinetics of antigorite using in situ high-temperature infrared microspectroscopy. *Physics and Chemistry of Minerals*, 40(4):319–330.

Schilling, F. and Wunder, B. (2004). Temperature distribution in piston-cylinder assemblies: Numerical simulations and laboratory experiments. *European Journal of Mineralogy*, 16(1):7–14.

Scholz, C. H. (1998). Earthquakes and friction laws. *Nature*, 391(6662):37–42.

Schwartz, S., Guillot, S., Reynard, B., Lafay, R., Debret, B., Nicollet, C., Lanari, P., and Auzende, A. L. (2013). Pressure–temperature estimates of the lizardite/antigorite transition in high pressure serpentinites. *Lithos*, 178:197–210.

Syracuse, E. M., van Keken, P. E., and Abers, G. A. (2010). The global range of subduction zone thermal models. *Physics of the Earth and Planetary Interiors*, 183(1-2):73–90.

Takahashi, M., Uehara, S. I., Mizoguchi, K., Shimizu, I., Okazaki, K., and Masuda, K. (2011). On the transient response of serpentine (antigorite) gouge to stepwise changes in slip velocity under high-temperature conditions. *Journal of Geophysical Research-Solid Earth*, 116(B10).

Trittschack, R., Grobety, B., and Brodard, P. (2014). Kinetics of the chrysotile and brucite dehydroxylation reaction: a combined non-isothermal/isothermal thermogravimetric analysis and high-temperature x-ray powder diffraction study. *Physics and Chemistry of Minerals*, 41(3):197–214.

Tullis, T. E. and Tullis, J. (1986). Experimental rock deformation techniques. In *Mineral and rock deformation: Laboratory studies*, volume 36, pages 297–324. American Geophysical Union Washington, DC.

Vyazovkin, S., Burnham, A. K., Criado, J. M., Perez-Maqueda, L. A., Popescu, C., and Sbirrazzuoli, N. (2011). Ictac kinetics committee recommendations for performing kinetic computations on thermal analysis data. *Thermochimica Acta*, 520(1-2):1–19.

Wada, I., Wang, K., He, J., and Hyndman, R. D. (2008). Weakening of the subduction interface and its effects on surface heat flow, slab dehydration, and mantle wedge serpentinization. *Journal of Geophysical Research: Solid Earth*, 113(B4).

Wada, I. and Wang, K. L. (2009). Common depth of slab-mantle decoupling: Reconciling diversity and uniformity of subduction zones. *Geochemistry Geophysics Geosystems*, 10.

Watson, E., Wark, D., Price, J., and Van Orman, J. (2002). Mapping the thermal structure of solid-media pressure assemblies. *Contributions to Mineralogy and Petrology*, 142(6):640–652.

Wunder, B. and Schreyer, W. (1997). Antigorite: High-pressure stability in the system mgo sio2 h2o (msh). *Lithos*, 41(1-3):213–227.